Rydberg Atoms for Quantum Information

by

Kelly Cooper Younge

A dissertation submitted in partial fulfillment
of the requirements for the degree of
Doctor of Philosophy
(Physics)
in The University of Michigan
2010

Doctoral Committee:

Professor Georg A. Raithel, Chair
Professor Paul R. Berman
Professor Jean P. Krisch
Professor Roseanne J. Sension
Assistant Professor Jennifer Ogilvie

"I am far from giving up hope. And even if it never works, there is always the consolation that this lack of success will be entirely mine." *Albert Einstein*

This work is dedicated to my mom, for her unwavering love and support.

ACKNOWLEDGEMENTS

It is interesting how graduate school seems to go so slowly in the beginning, then about two thirds of the way through you seem to hit your stride because maybe things finally "click" for you, and then in the last year it is speeding by so fast you don't know how you'll ever finish everything you wanted to do in time. I want to thank all the people who helped me get through each of those stages, especially Georg Raithel whose lab I joined in 2007. Georg has always astounded me with his scientific insight, and I have been exceedingly grateful for his patient persistence in helping me on my way to my degree. Over the last three years, his daily encouragement and enthusiasm for science have inspired me to do my best work.

I would like to thank the members of the Raithel lab with whom I have worked, including David Anderson, Sarah Anderson, Cornelius Hempel, Brenton Knuffman, Rahul Mhaskar, Éric Paradis, Erik Power, Aaron Reinhard, Rachel Sapiro, Andy Schwarzkopf, Betty Slama, Mallory Traxler, Rui Zhang and Stefan Zigo. I want to thank Brenton for helping me to learn the CryoMot experiment before he graduated, and for all of the epic emails we exchanged after he left. Sarah, I am really excited to see where you take the experiment from here. I'll miss our afternoon trips to Amer's! I also want to thank Aaron for letting me join his experiment in 2007 and teaching me the "ropes" of the Raithel lab. Rui, thank you for your contagious happiness and for brightening the lab every day. Stefan, keep playing techno music in the highB. Cornelius! I miss our afternoon coffees where I never actually drank coffee. And

Éric, don't give up on me, eventually I'll learn how to pronounce Moulin Rouge, parfait, and possibly even poincaré.

Over the last five years, I've made some of the closest friendships I have ever had. Beth, thanks for all the therapy sessions and the afternoon trips to Starbucks that turned into four hours of not working, the midnight Harry Potter movies and vegan cupcakes and that gingerbread house we made. Oh, and that time we had to defend ourselves with the saw I made in shop class. Kristin, I never could have run that 5k without you, and thanks for spending twenty hours with me in my car driving to and from Minnesota.

I know I never would have gotten this far without the help of my high school and undergraduate physics professors. Steven Brehmer, my high school physics teacher was the reason I chose to pursue physics in college. His love for the field and his remarkable teaching ability made him stand out among all others. My undergraduate professors, Dennis Henry, Tom Huber, Steve Mellema, Chuck Niederriter, and Paul Saulnier prepared me very well for the hardships of graduate school, even if I didn't always appreciate the hard work.

Most importantly, I want to thank my family for all of the support and encouragement they have given me over the last many, many years I have spent in school. Mom, we spent 16,883 minutes on the phone while I was in graduate school. We also spent 35 days in the Caribbean, and I think I learned that one of the best ways to do well in graduate school is to stop thinking about graduate school once in a while. Dad, thanks for all the golf lessons and trips to Arizona. If physics doesn't work out, maybe I can join the pro tour?

I published 14 papers in graduate school. I also flooded the top of the dipole blockade table, burnt through an iris with 10 W of 1064, set my IR card on fire, used

a heat gun to dry off my pants after walking through snow, tried to clean a mirror with tap water, used double stick tape to fix a mirror in the dipole blockade blue laser, and froze a variety of different objects, not to mention my arm, with liquid nitrogen. And trust me, there are countless other stories that ended in, "oh man, that was stupid." All in all, I'd say it has been a productive five years.

TABLE OF CONTENTS

LIST OF TABLES

Table

LIST OF FIGURES

Figure

LIST OF APPENDICES

Appendix

ABSTRACT

I examine interactions between ensembles of cold Rydberg atoms, and between Rydberg atoms and an intense, optical standing wave. Because of their strong electrostatic interactions, Rydberg atoms are prime candidates for quantum information and quantum computation. To this end, I study excitation dynamics in many-body Rydberg systems using a rotary echo technique similar to the echo sequences used in nuclear magnetic resonance schemes. In this method, a phase reversal of a narrow-band excitation field is applied at a variable time during the excitation pulse. The visibility of the resulting echo signal reveals the degree of coherence of the excitation process. Rotary echoes are measured for several $n\mathrm{D}_{5/2}$ Rydberg levels of rubidium with principal quantum numbers near $n = 43$, where the strength of electrostatic Rydberg-atom interactions is sharply modulated by a Förster resonance. The Rydberg-atom interactions diminish the echo visibility, in agreement with theoretical work. The equivalence of echo signals with spectroscopic data is also examined.

Applications of Rydberg atoms based on controlled interactions require a trapping device that holds the atoms at well-defined positions several microns apart. Rydberg atoms in ponderomotive optical lattices present a unique platform to meet this requirement, as well as to study properties and interactions of these highly excited atoms. Because the Rydberg electron is so loosely bound, the ponderomotive interaction for a Rydberg electron is very similar to a free electron. Ponderomotive lattices tailored to trap Rydberg atoms will allow new experiments in quantum infor-

mation physics and high-precision spectroscopy. Microwave spectroscopy is used as a powerful technique to probe the motion and to verify trapping of Rydberg atoms in ponderomotive lattices. The potentials for non-degenerate, low angular momentum states, are used to obtain ensembles of Rydberg-atom trajectories in the lattice, and to simulate the spectra of microwave transitions of Rydberg atoms moving through the lattice. Additionally, adiabatic potentials are calculated for Rydberg atoms in one-dimensional ponderomotive lattices for a variety of atomic states and lattice parameters. The lattice induced mixing of nearly-degenerate, high-angular-momentum states is explained in terms of effective electric and magnetic fields.

CHAPTER I

Introduction

Rydberg atoms have attracted significant interest in the scientific community over the past several decades due to their unique, exaggerated properties. These atoms are characterized by their large sizes, strong electro-static interactions, and polarizabilities that scale with principal quantum number to the seventh power, resulting in extreme sensitivity to external fields. The name "Rydberg atom" is in honor of the Swedish physicist Johannes Rydberg, who introduced the Rydberg formula and the Rydberg constant as an empirical way to determine the energy of the spectral lines in hydrogen. The formula also applies to other species of atoms, and is an excellent approximation for highly excited Rydberg atoms. These atoms have an outer electron that is excited into a very high energy state, i.e. a state of high principal quantum number n. When this occurs, the atom behaves essentially like a very large hydrogen atom, with a loosely bound outer electron at a high radial separation from the positive ion core. Rydberg atoms are often used in experiments pertaining to quantum information [1, 2], but are also used in other contexts. For example, Rydberg-Rydberg molecules can be created from multipole forces that bond two Rydberg atoms at large internuclear distances [3–6]. Ref. [3] suggests a number of interesting possibilities for the use of such molecules, such as studying collective

excitation, and the creation of superposition states between free and bound atoms. Rydberg atoms can also spontaneously evolve into a plasma [7] and vice versa. Some of the first experiments in plasma formation were conducted by the Rolston group at the National Institute of Standards and Technology in Gaithergsburg, MD [8–10]. An ultracold plasma formed via ionization of cold Rydberg atoms is a unique state of matter that can have temperatures four orders of magnitude smaller than conventional cold plasmas. Such ultracold plasmas have applications to antihydrogen formation [11] and even quantum information [2]. Because the strong interactions of Rydberg atoms persist over long ranges (10's to 100's of microns), these atoms are also often studied in the context of many-body physics [12–15].

1.1 Rydberg atom properties

Because of the Rydberg atom's similarity to a hydrogen atom, the Bohr model works well as a first approximation for many of the Rydberg atom's properties. For example, balancing the centripetal acceleration of the Rydberg electron and Coulombic force from the nucleus gives us

$$\frac{m_e v^2}{r} = \frac{e^2}{4\pi\epsilon_0 r^2} \tag{1.1}$$

where m_e and v are the electron's mass and speed, respectively. Quantizing angular momentum in units of $\hbar$ ($m_e v r = n\hbar$) immediately leads to the relationship

$$r = \frac{\hbar^2}{(e^2/4\pi\epsilon_0)\, m_e} n^2 = a_0 n^2 \tag{1.2}$$

where a_0 is the familiar Bohr radius. This is an important result which tells us how the Rydberg atom radius scales with n and explains why Rydberg atoms can reach nearly macroscopic sizes. Equation 1.1 also leads to a result for the Kepler

frequency, $\omega = v/r$, of the Rydberg electron:

$$\omega^2 = \frac{e^2/4\pi\epsilon_0}{m_e r^3}. \tag{1.3}$$

From Equations 1.2 and 1.3, we see that the Kepler frequency scales as n^{-3}, which will be important for later sections of this thesis concerning optical lattices. A number of other scaling parameters can also be derived from the classical description of the atom and are summarized in Table 1.1. Two particularly relevant scalings include the electric field at which the Rydberg atom ionizes, which will be important in state selective detection of Rydberg atoms, and the dipole-dipole interaction (proportional to the dipole moment squared), which is the basis for many of the studies in this thesis.

To determine the ionization electric field for a Rydberg atom, I begin with the combined Coulomb-Stark potential given by

$$V = -\frac{1}{r} + Ez \tag{1.4}$$

where E is an electric field applied along the z direction and r is the radius of the Rydberg electron orbit. This equation is written in atomic units which are summarized in Appendix A.2. The saddle point of this potential, found by setting the derivative equal to zero, is located at $z = -E^{-1/2}$ where the potential is $-2\sqrt{E}$. This means that an electric field of $E = W^2/4$, where W is the binding energy of the Rydberg electron, will ionize the atom. The binding energy, W, can be calculated from a sum of the electron's kinetic and potential energies and is equal to $-1/2r$. Employing Equation 1.2, the electric field required to ionize Rydberg states is found to be

$$E = \frac{1}{16n^{*4}} \tag{1.5}$$

where n^* is the effective principal quantum number, $n - \delta_l$ [16]. This derivation works very well to estimate the ionization electric field, but ignores the fact that as the ionization electric field is increased, the atoms undergo a Stark shift and may mix with nearby energy levels. The atom may traverse the Stark map adiabatically (staying in its original energy level) or diabatically (hopping to other nearby levels) depending on both the speed of the electric field ramp and the size of the avoided crossings. Diabatic traversal of the Stark map will broaden the ionization signature and result in ionization electric fields ranging from $\frac{1}{4n^{*4}}$ to $\frac{1}{9n^{*4}}$ [16].

The dipole-dipole interaction is the interaction energy of a dipole in the electric field of another dipole. The dipole moment of an atom is given by $\vec{\mu} = e \cdot \mathbf{r}$ and scales like n^2. The electric field of a dipole at a location $\mathbf{R}$ is the result of the field from the nucleus which scales as $1/R^2$, and the field of the electron which scales as $-1/\left(R + r\right)^2$. The sum of these fields for large distances $\mathbf{R}$ can be approximated as r/R^3, or n^2/R^3. This results in a dipole-dipole interaction energy of $V_{\text{dd}} \sim n^4/R^3$. It is important to note that in the context of the Rydberg atom experiments discussed here, the atoms do not have permanent dipole moments, and therefore the dipole-dipole interaction is a result of *transition* dipole moments to other states. Additionally, I have left out the angular dependence of the derivation of the dipole-dipole interaction energy. The complete form of the interaction energy is given by

$$V_{\text{dd}} = \frac{\vec{\mu}_1 \cdot \vec{\mu}_2 - 3\left(\vec{\mu}_1 \cdot \hat{n}\right)\left(\vec{\mu}_2 \cdot \hat{n}\right)}{R^3} \tag{1.6}$$

where $\vec{\mu}_1$ and $\vec{\mu}_2$ are the transition dipole moments of the two atoms involved in the interaction, and $\hat{n}$ is the unit vector pointing from atom one to atom two.

Binding energy	n^{-2}
Energy between adjacent states	n^{-3}
Orbital radius	n^{2}
Dipole moment	n^{2}
Polarizability	n^{7}
Radiative lifetime	n^{3}
Rabi frequency for excitation	$n^{-3/2}$

Table 1.1: Scaling laws for Rydberg atoms.

Table 1.1 contains many of the Rydberg atom scalings that will be important for this thesis.

1.2 Rydberg atoms for quantum information

The application of Rydberg atoms to quantum computing is perhaps the most significant driving force behind the study of these exotic atoms. Here I will briefly explain recent developments in the field and how Rydberg atoms can be used to generate quantum gates. There are several excellent references in which the reader can find more detailed information [1, 2, 17] as well as the Quantum Information Science and Technology Roadmap website, operated by Los Alamos National Security, LLC, at http://qist.lanl.gov/.

The importance of modern computing in everyday life cannot be overestimated. The speed of computers has increased dramatically each year ever since the first integrated circuits were developed over five decades ago. One of the cofounders of Intel, Gordon Moore, was the first person to point out that computers seemed to double in speed about once every 18 months. Indeed, Moore's law has been remarkably accurate since it was first introduced in 1965. The problem with Moore's law is that within the next ten years we will enter a new realm where the size of transistors reaches the atomic length scale. The issue with this is that quantum mechanical effects begin to interfere with the fidelity of electronic devices as they

get smaller and smaller. However, we can instead take advantage of these effects by using the principle of superposition.

A classical computer uses bits of information stored as 1s or 0s, while a quantum computer is capable of storing any superposition of these two states. While at the end of the computation the superposition state is destroyed and the result must be read out simply as one of the two states, the advantage of the quantum nature of the system lies in the computation itself. One can show that a quantum computer can be simulated by a classical computer, but it is impossible to perform this simulation efficiently. This means that quantum computers offer an essential speed advantage over classical computers. In fact, this speed advantage is so immense that many researchers believe that no conceivable amount of progress in classical computation would ever be able to close the gap between the classical and quantum computation domains [17, 18].

David Deutsch of the University of Oxford was the first person to develop a specifically quantum computational algorithm and therefore is widely considered one of the pioneers of the field of quantum computation. In 1985, Deutsch developed the idea of the Universal Quantum Computer that could efficiently simulate any physical system using the principles of quantum mechanics. He was the first to show that there existed problems that could be solved using a quantum computer that were not tractable on a classical computer. This idea was further developed in 1994 when Peter Shor showed that the problem of finding the prime factors of a number could be solved efficiently on a quantum computer. This is an enormously important problem in today's world because of its ties to data encryption, and is a prime reason why research in quantum information is of prime interest for defense agencies. At about the same time, another famous physicist, Richard Feynman, pointed out that

quantum systems that were too complicated to be simulated on a classical computer could in fact be simulated on a quantum computer, which would have huge scientific and technological implications. The bottom line is that although we still do not know all of the benefits that quantum computing has to offer, it is certain that it will become the future of computing.

For successful quantum computation, one must create a quantum bit, or qubit, that can exist in one of two states labeled $|0\rangle$ and $|1\rangle$. In 2000, David DiVincenzo of IBM laid out some requirements for a successful quantum computer. These include scalability, the ability to initialize the qubits, gates fast enough to avoid the effects of decoherence, a universal gate set (meaning that any arbitrary operation can be completed), and the ability to read out an answer. What kinds of qubit systems show promise for the creation of a quantum computer? There are several different avenues that are all simultaneously being explored[1]. Popular systems include trapped ions [19], neutral atoms [20], semiconductor quantum dots [21], cavity QED [22], and NMR based systems [23].

Ions are one of the most promising candidates because they are easily trapped and have strong interactions via the Coulomb force. The strong interactions mean that gate operations can be completed quickly. However, just like the ions interact strongly with each other, they are also capable of interacting strongly with their environment, which leads to decoherence. Neutral atoms provide the opposite situation. They interact more weakly with their environment than ions, but at the same time gate times are longer because they also interact weakly with other atoms. Alternatively, Rydberg atoms provide the best of both of these worlds.

Rydberg atoms, though neutral, interact very strongly with each other. This

[1]The website mentioned earlier, http://qist.lanl.gov/, contains roadmaps for all of the current quantum information research areas. While these roadmaps are from 2004 and the field has grown remarkably since then, many of explanations are excellent for basic understanding of the principles involved.

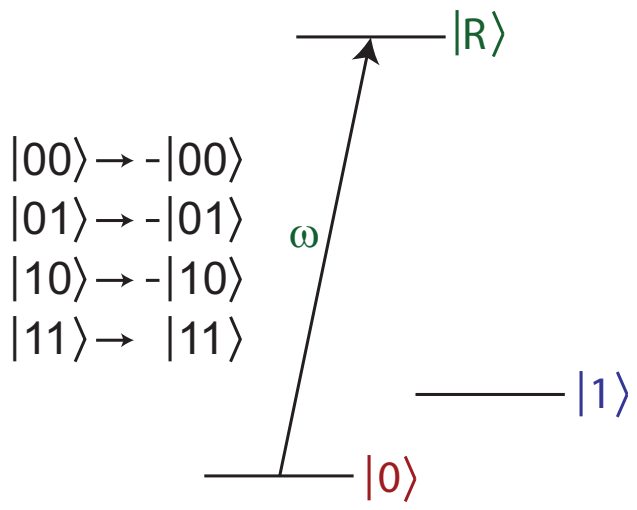

Figure 1.1: Rydberg atom fast phase gate first proposed by Jaksch *et al.* in 2000.

allows quantum gates to be completed quickly, as in the case of trapped ions. An additional advantage that ions do not have is the fact that the interaction can be tuned and even switched off for a desired amount of time. This can be done either by Stark shifting the Rydberg state with an electric field, or by de-exciting the atom from the Rydberg state. Once the interaction is turned off, the coherence can be preserved because as mentioned above, the neutral atom does not interact strongly with its environment. Lastly, because Rydberg atoms are significantly larger than their ground-state atom counterparts, they are more easily accessible (i.e. they can be individually addressed with laser beams) for quantum computing applications.

The first Rydberg atom quantum gate was proposed by Jaksch *et al.* in 2000 [1]. This proposal was for a two-atom fast phase gate taking advantage of the dipole-dipole interaction that prevents more than one Rydberg atom from being excited at one time (see Section 1.3). This gate involves hyperfine ground state levels, labeled $|0\rangle$ and $|1\rangle$, and one Rydberg state. A laser couples $|0\rangle$ to the Rydberg level, while $|1\rangle$ is not coupled, as shown in Figure 1.1. There are three steps to the gate: a π pulse is applied to atom A, a 2π pulse is applied to atom B, and then another π pulse is

applied to atom A. The idea is that for every case except for $|11\rangle$ (where there is no coupling of the atoms to the Rydberg state at all), the excitation blockade prevents the second atom being excited. This results in a phase shift for every state except $|11\rangle$. The truth table for such a gate is shown on the left-hand side of Figure 1.1. Later, Lukin *et al.* showed that this same idea could be applied to a mesoscopic ensemble of atoms via entanglement [2].

Since then, a number of exciting advances have been made in the field of quantum information processing with Rydberg atoms. Particularly, in 2009, Phillipe Grangier's research group from Laboratoire Charles Fabry and Pierre Pillet's research group from Laboratoire Aimé Cotton demonstrated collective excitation of two atoms each held in a separate dipole trap [24]. This experiment was a major step forward in quantum-information science as well as in many-body physics in general because it was the first time anyone had successfully demonstrated the excitation blockade with individual atoms. They also observed an enhancement of single-atom excitation proving the coherent behavior of their system. In early 2010, Grangier's group generated an entangled state with the same system of spatially separated dipole traps with a fidelity of 0.75 [25]. At the same time, a research group at the University of Wisconsin demonstrated a controlled-NOT gate with a fidelity of 0.58 [26].

1.3 Rydberg atoms and the excitation blockade

As mentioned in Section 1.2, the Rydberg excitation blockade, sometimes referred to as the dipole blockade, is the basis behind using Rydberg atoms for quantum information. The strong electrostatic interactions between Rydberg atoms lead to energy perturbations of any system with more than a single excitation. This is shown graphically in Figure 1.2. In this figure, the labels on the right hand side are

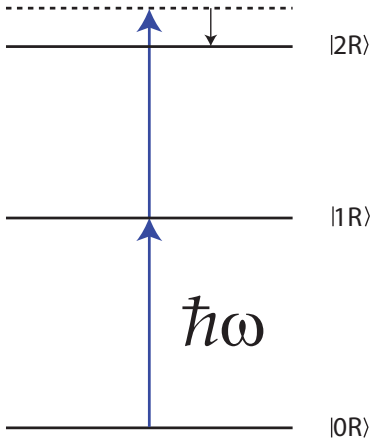

Figure 1.2: Rydberg excitation ladder.

shorthand notation for the number of Rydberg excitations that are coherently shared among all atoms in the excitation region of our experiment until a measurement is made that projects that excitation onto a single atom. The ket $|0\mathrm{R}\rangle$ represents a system where all atoms are in the ground state, and the ket $|1\mathrm{R}\rangle$ is sum over all possible configurations where a single atom is in the Rydberg state. It is somewhat inaccurate to label the second excited state with the ket $|2\mathrm{R}\rangle$ because this is a doubly excited state and its energy will depend on the distance between the excited atoms. However, it will suffice for the treatment in this thesis.

Here, I have labeled the energy difference between the states $|0\mathrm{R}\rangle$ and $|1\mathrm{R}\rangle$ as $\hbar\omega$. If the atoms were non-interacting, then one would expect that the $|1\mathrm{R}\rangle \rightarrow |2\mathrm{R}\rangle$ transition energy would also be $\hbar\omega$. However, because of the afore mentioned strong interactions, the $|2\mathrm{R}\rangle$ state is shifted in energy. The size and direction depends on the Rydberg state [27], but if the magnitude of the shift is greater than the linewidth of the optical source used for excitation, then the $|2\mathrm{R}\rangle$ state is out of resonance, and all excitation above $|1\mathrm{R}\rangle$ is blockaded.

The energy shift for an arbitrary Rydberg state may be calculated using second order perturbation theory. Consider two Rydberg-atom states $A = |n, l, j, m_j\rangle$ that

have non-zero transition-dipole-moments to the states $B = |n', l', j', m'_j\rangle$ and $C = |n'', l'', j'', m''_j\rangle$. The infinite-separation energy defect is defined as $\Delta = W_B + W_C - 2W_A$. It is then found that the second order shift, $\Delta W^{(2)}$, is given by

$$\Delta W^{(2)} = -\sum_{\substack{n',l',j',m'_j,\\ n'',l'',j'',m''_j}} \frac{|\langle n'', l'', j'', m''_j| \otimes \langle n', l', j', m'_j|V_{\mathrm{dd}}|n, l, j, m_j\rangle \otimes |n, l, j, m_j\rangle|^2}{\Delta} \tag{1.7}$$

where V_{dd} was defined in Equation 1.6. Equation 1.7 is sufficient to find the energy shift of an arbitrary state $|n, l, j, m_j\rangle$ as long as the Rydberg atom does not possess a permanent dipole moment. Low angular momentum states of rubidium Rydberg atoms do not have a permanent dipole moment unless an external field is applied at a sufficient strength [28].

In general, the sum in Equation 1.7 will have contributions from many two particle states. If none of the interaction channels ($2A \leftrightarrow B+C$) are resonant (i.e. $\Delta \gg V_{\mathrm{dd}}$), then the system is considered to be in the off-resonant, van der Waals regime. In this case, the interaction induced energy shift scales as V_{dd}^2/Δ or n^{11}/R^6, as is evident from Equation 1.7. However, there are cases in which a resonant interaction channel ($\Delta \ll V_{\mathrm{dd}}$) exists. In this case, the non-degenerate perturbation treatment in Equation 1.7 is not accurate. Here, the system is in the on-resonant, dipole-dipole regime, and the interaction induced energy level shift is calculated via degenerate perturbation theory. One then finds that the energy left shift scales as V_{dd} or n^4/R^3. These resonant interaction channels are referred to as Förster resonances, and because the value of Δ can easily be Stark-shifted using electric fields, it possible to generate a Förster resonance in cases where they do not exist naturally. The tunability of such interactions and the enhanced interaction energy makes them a popular research

subject in numerous contexts [14, 29–31].

1.4 Properties of Rubidium

All of the experiments in this thesis use ^{85}Rb. Alkali-metal atoms (lithium, sodium, potassium, rubidium, cesium, and francium) are popular for Rydberg atom experiments as well as for atomic physics experiments in general. For one, their excitation frequency from the ground to the first excited state is in the visible part of the electromagnetic spectrum. Laser light at these frequencies is increasingly easy to generate, and indeed, alkali-metal atoms were the first to be cooled and trapped. It is also an easy task to generate an atomic beam because of the large vapor pressure of these atoms. All alkali-metal atoms have a closed electronic core with a single valence electron. This means that the state of the electron is completely determined by its orbital and spin angular momenta, l, and s, since the closed electronic core does not contribute.

There are three important temperature scales to consider when cooling and trapping ^{85}Rb [32]. The first of these is referred to as the capture limit. When resonant light is shined on an atom moving at a high speed, the Doppler shift may cause the light to be far enough out of resonance that the atom cannot absorb the photons' energy. For ^{85}Rb, this velocity is equal to

$$v_c = \frac{\gamma}{k} = 2\pi \times 6 \text{ MHz} \times \left(\frac{2\pi}{\lambda}\right)^{-1} = 4.7 \text{ m/s} \tag{1.8}$$

where γ is the linewidth of the transition and λ is the frequency. This corresponds to a temperature of

$$T_c = \frac{M v_c^2}{k_B} = 222 \text{ mK} \tag{1.9}$$

where M is the mass of Rubidium and k_B is the Boltzmann constant.

The next temperature scale is the Doppler limit, which is the energy corresponding to the natural linewidth of a transition. The Doppler limit arises because of the randomness of spontaneous emission (necessary for laser cooling), which causes the atom to move on a random walk and therefore competes with cooling. The Doppler temperature gives us a limit of how effective Doppler cooling can be for a particular species of atom, although sub-Doppler cooling often allows much lower temperature almost by accident [33]. The Doppler temperature and velocity are given by

$$T_D = \frac{\hbar\gamma}{2k_B} = 144\ \mu\text{K} \tag{1.10}$$

$$v_D = \left(\frac{k_B T_D}{M}\right)^{1/2} = 11.8\ \text{cm/s}. \tag{1.11}$$

Lastly, the recoil limit, as the name suggests, corresponds to the energy gained or lost through the absorption or emission of one photon by the atom. For Rb,

$$v_r = \frac{\hbar k}{M} = 0.6\ \text{cm/s} \tag{1.12}$$

$$T_r = \frac{M v_r^2}{k_B} = 0.37\ \mu\text{K} \tag{1.13}$$

There are two rather inventive ways of optically cooling below the recoil limit, including Raman cooling [34] and Velocity Selective Coherent Population Trapping (VSCPT) [35]. These methods allow one to reach a temperature in the 100's of nanoKelvin range. Below this, for example to achieve BEC, non-optical techniques such as evaporative cooling are necessary [36]. In this thesis, I focus on atoms cooled to approximately the Doppler limit, and sub-Doppler cooling is not usually a requirement.

1.5 Thesis framework

This thesis is organized as follows: In Chapter 2, I begin with a summary of the experimental apparatus used to conduct the experiments described in the remainder of the thesis. Two primary setups were used, referenced as the "Blockade Experiment" and the "CryoMOT".

Chapter 3 discusses a rotary echo technique I used to demonstrate excitation coherence in a system of Rydberg atoms as a means to overcome the effects of density inhomogeneity. Maintaining the coherence of the system is important in many applications, but most notably in quantum computation where information must be preserved during the course of each gate operation. My experimental effort was initially inspired by a paper written by Francis Robicheaux in 2008 [37]. There, it was suggested that rotary echo schemes could be used to quantify coherence in a mesoscopic ensemble of atoms. Previously, coherence was measured by observing Rabi oscillations of cold, trapped atoms between the ground and excited Rydberg state. However, the number of atoms in a system had to be limited to one or two in order to measure such coherence, since interactions between Rydberg atoms quickly caused dephasing in the Rabi oscillations of neighboring atoms [38]. Also in 2008, Tilman Pfau's research group published their results on applying the rotary echo technique to a 3.8 μK sample of rubidium atoms with a density of 5.2×10^{13} cm^{-3} [39]. This was a remarkable achievement because it allowed the measurement of excitation coherence in a large ensemble of atoms - a system much easier to produce than a single isolated atom.

The goal of my experiment was to use a rotary echo sequence to verify coherence in a system of atoms with a much higher temperature, and to investigate the effects

of atom-atom interactions on echo visibility. I was able to measure a rotary echo in a 1 mK sample of atoms with a density of 2.5×10^{11} cm^{-3}. This experiment is the first in which an echo signal was observed for a system of atoms with a temperature as high as 1 mK and is more applicable to today's research in quantum computation with Rydberg atoms than the 3.8 μK temperatures used in [39]. I show how echo visibility depends strongly on the strength of Rydberg-Rydberg interactions, and explain the results in terms of the theory described in Ref. [39]. I also show that the interpretation given in this paper is inaccurate for certain cases in which an increased interaction strength between Rydberg atoms appears to induce a reduction in the observed echo signal. Even more importantly, this echo technique can be used in the future to measure coherence as a function of a wide variety of parameters, including atom temperature, density, interaction strength, and interaction time. In this way, systems designed for quantum computation can be easily analyzed in terms of their coherence properties.

The fundamental parts of the atom trap and imaging system used to measure rotary echoes were designed and built by Tara Cubel-Liebisch and Aaron Reinhard. After their graduation, I designed the system of electronics used to generate the rotary echo sequence and wrote all of the software used to record and analyze the echo signals. I also designed and engineered a system of crossed-beam excitation to narrow my excitation region from several millimeters to about ten microns. Additionally, this system is capable of dual excitation regions produced by diffraction in a non-linear crystal, a feature that will be useful in future endeavors.

In Chapter 4, I use microwave spectroscopy between neighboring Rydberg states to study Rydberg atoms that are within an optical lattice. As with Chapter 3, my work here is also directly applicable to quantum information. However, instead of

studying coherence, I examine the ponderomotive optical lattice as a novel method of Rydberg atom storage that will allow atoms to be individually addressed for qubit initialization and readout. And because the lattice can be precisely tailored using the lattice laser beams, it also allows for scalability of the system. The experiment described in Chapter 4 constitutes the first evidence of a ponderomotive optical lattice for Rydberg atoms. The theoretical existence of such a lattice had been suggested in Refs. [40] and [41], but never observed experimentally. Not only does this trap localize the atoms in space, but it also confines the atoms in micron-sized, spatially separated potential wells such that the atoms to be individually addressed via focused laser beams. This work was featured on the front page of the National Science Foundation website at www.nsf.gov as well as the front page of the University of Michigan website at www.umich.edu.

The experimental apparatus used in this experiment was built by Alisa Walz-Flannigan and Brenton Knuffman. After their graduation, I added the optics to generate a focused optical lattice at the center of the excitation region, and was the first to experimentally observe and characterize the effects of the lattice by using optical and microwave spectroscopy (detailed in depth in Chapter 4).

In Chapter 5 I calculate the trajectories of Rydberg atoms in optical lattices in order to better understand the experimental results shown in Chapter 4. The results of the simulations prove the effectiveness of microwave spectroscopy as a tool to characterize the efficiency of the optical lattice as a trapping device. The simulations used in this chapter were written by Prof. Georg Raithel. I performed the calculations and analyzed the resulting spectra and trajectories.

Chapter 6 extends the optical lattice discussion to a theoretical description of much deeper lattice potentials and compares the results to the diamagnetic problem

in classical mechanics. Deeper lattice potentials than those achieved in experiments described in Chapter 4 will be necessary to observe these effects experimentally. The simulations used here were also written by Georg Raithel. Analysis of my results using the simulations was done by Georg and myself.

Lastly, in Chapter 7 I summarize my results and describe a few possible future research projects involving both the Blockade Experiment and the CryoMOT.

CHAPTER II

Experimental Apparatus

I performed the experiments described in this thesis using two primary experimental designs. I will refer to these two designs as the "Blockade Experiment" and the "CryoMOT". In this chapter, I will discuss the basic principles common to all experiments, and then describe the important differences between the Blockade Experiment and the CryoMOT.

2.1 Laser cooling and magneto-optical trapping of atomic vapors

Room temperature atomic vapors are made up of atoms with velocities of approximately 300 m/s. However, since we are concerned with studying atom-atom interactions, we desire a system where thermal contributions can be neglected. This is achieved prior to Rydberg-atom excitation via laser cooling of an ensemble of ground-state atoms. The technique of cooling atoms using radiation pressure is an integral part of many atomic physics experiments today, and has opened entirely new domains of physics since its advent. Prior to the development of laser cooling, studies of atomic samples were all performed with fast-moving atoms, which can make measurements very difficult. Spectral resolution was limited because of the limited observation time, as well as the displacement and broadening of spectral lines due to the Doppler shift and relativistic time dilation. One of the biggest motivations for

developing laser cooling was the limitation on atomic clock performance. Laser cooling also helped lead to many new phenomena such as Bose-Einstein condensation [42] and quantum logic gates [43] The technique of laser cooling was first developed using ions trapped with electric fields, and led to the award of the 1997 Nobel prize in physics to Steven Chu, Claude Cohen-Tannoudji and William Phillips.

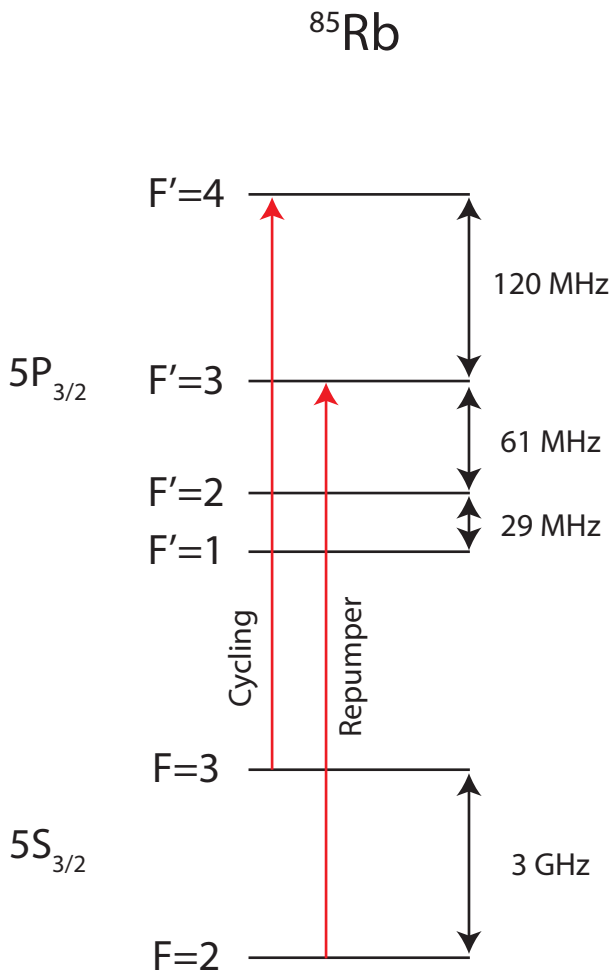

Figure 2.1: Hyperfine levels of the $5S_{1/2}$ and $5P_{3/2}$ levels in ^{85}Rb.

Cooling can be generated along one direction of motion by directing a red-detuned laser into a cloud of atoms. Due to the Doppler shift, atoms moving anti-parallel to the laser beam will absorb more radiation from the laser beam than atoms moving parallel to the beam. Atoms will re-emit the absorbed radiation in a random

direction, and, after many thousands of scattering events, there will be a significant cooling effect along the direction of the laser beam. Cooling in all directions is accomplished by applying three pairs of counter-propagating beams in orthogonal directions.

Laser cooling is accomplished using a "cycling" transition, meaning that the atom will absorb and re-emit in a closed sequence of atomic states. Figure 2.1 shows the hyperfine levels of $5S_{1/2}$ and $5P_{3/2}$ levels in ^{85}Rb. For simplicity, the m_F sub-levels are not shown, but we apply σ^+ polarized light such that the atoms are always in the extreme m_F states. The cycling transition is from $5S_{1/2}$, $|F = 3\rangle \rightarrow 5P_{3/2}$, $|F' = 4\rangle$. However, because the $|F' = 4\rangle$ state is separated from the $|F' = 3\rangle$ by only 120 MHz, about one out of every 1600 photons scattered will off-resonantly excite into the $|F' = 3\rangle$ state. From here the atom can decay into the $|F = 2\rangle$ manifold, which is 3 GHz detuned from the cycling transition. Therefore, a "repumper" laser must be used to transfer the atom back to the cycling transition. This laser is tuned to the $|F = 2\rangle \rightarrow |F' = 3\rangle$ transition.

The limits of this technique arise from the fact that the atoms will undergo a random walk as they spontaneously emit absorbed radiation. Laser cooling is capable of reaching temperatures near the Doppler limit: 144 μK, or 11.8 cm/s for Rubidium. Thus, we can reduce the velocity of the atoms from the speed of sound to approximately the speed of a mosquito. For more information, C.J. Foot's *Atomic Physics* provides an excellent overview of the details of this technique.

Laser cooling generates what is often referred to as an optical molasses, since an atom moving in a light field reacts similarly to a particle moving a viscous fluid. We must note, however, that laser cooling is a velocity dependent force and not a position dependent force. Atoms will be cooled while they remain under the presence

of radiation pressure, but are not constrained to remain within of the laser beam path. Therefore, laser cooling alone cannot be used to trap atoms. The addition of a quadrupole magnetic field centered about the trapping region provides a position-dependent restoring force. This kind of setup is referred to as a magneto-optical trap or a MOT, and offers an extremely robust method of cooling and confining atoms.

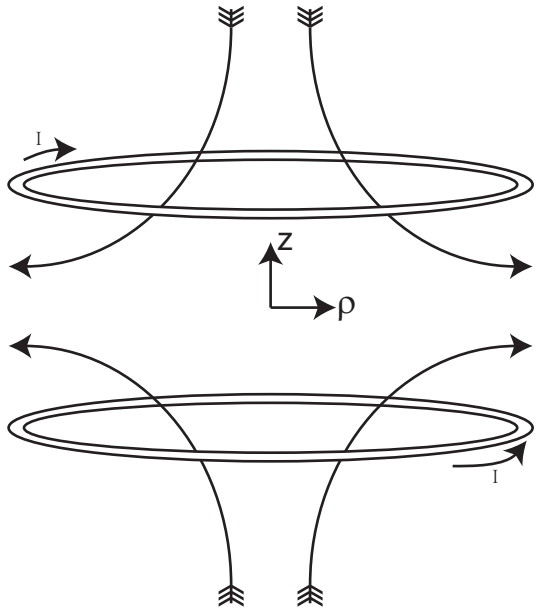

Figure 2.2: The field coils and magnetic field lines of a magneto-optical trap.

Figure 2.2 shows how the magnetic field of a MOT is constructed. Two coils in the anti-Helmholtz configuration create the necessary quadrupole field. The force on an atom in a magnetic field is given by

$$\overrightarrow{F} = \overrightarrow{\nabla}(\overrightarrow{\mu} \cdot \overrightarrow{B}) \tag{2.1}$$

where $\overrightarrow{\mu}$ is the magnetic moment of the atom. The magnetic field $\overrightarrow{B}$ is given by

$$A(\rho^2 + 4z^2)^{1/2} \tag{2.2}$$

where A is the field gradient. A convenient quality of the quadrupole field is that the field gradient is A fixed along any line through the origin, so on any of these lines,

we have $B = Ar\sqrt{4\cos^2\phi + \sin^2\phi}$: a linear field gradient when ϕ is constant. This gradient produces the energy level structure for the Zeeman levels of the trapped atom shown in Figure 2.3. This example is for a simple $J_g = 0 \rightarrow J_e = 1$ system, but easily extends into more complicated atom structures where $J_g \rightarrow J_e = J_g + 1$.

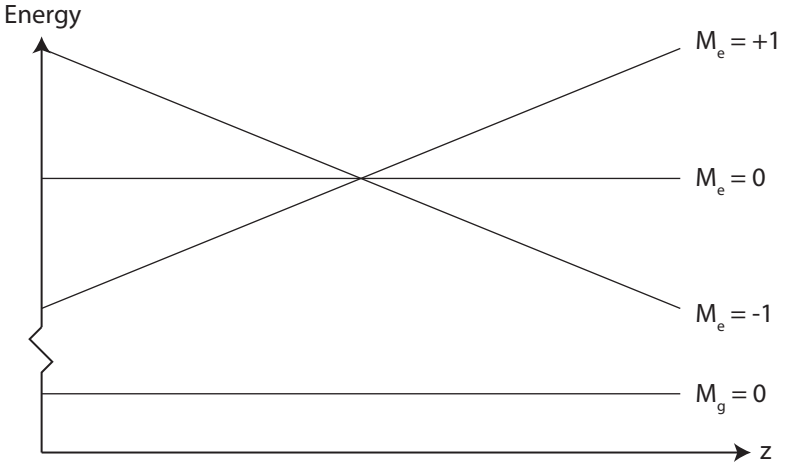

Figure 2.3: Zeeman splitting of the first excited state due to the linear magnetic field gradient.

We can take advantage of this Zeeman splitting by choosing the correct polarization for our cooling and trapping light. If the beam has frequency ω_l with σ^+ light incident from the left, and σ^- light is incident from the right, the excitation scheme will look like that shown in Figure 2.4:

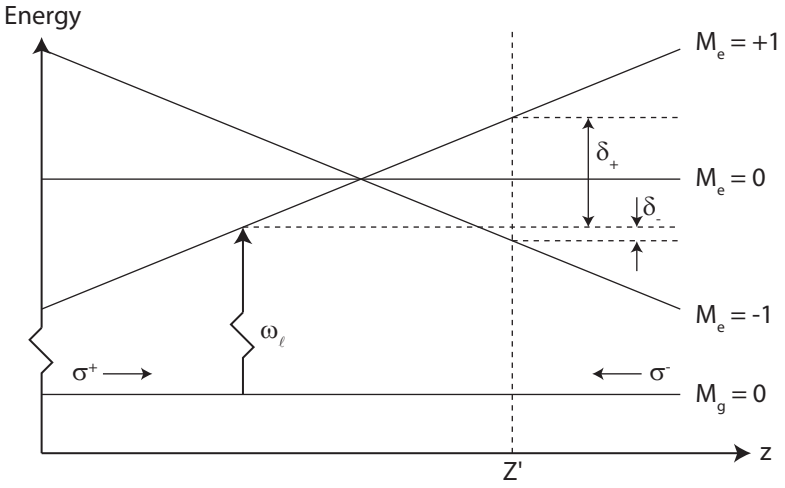

Figure 2.4: Excitation scheme for a magneto-optical trap.

Consider an atom at position z'. This atom is much closer to resonance with the light if it is in the $M_e = -1$ Zeeman sub-level than if it is in the $M_e = +1$ level. If it is in the $M_e = -1$ level, it can only scatter light from the σ^- beam (and vice versa), and therefore it will be preferentially scattered to the left. The reverse situation occurs when z' is located on the other side of the magnetic field zero.

It is of practical importance to remember the polarizations used for the MOT beams depend on the chosen frame of reference. In the figures in this section, the polarizations are with respect to the atoms, not to the beam axis. With respect to the beam axis, both beams along a single axis have the same polarization (either LCP or RCP *with respect to the direction of travel*). The strong axis of the magnetic field (vertical in Figure 2.2) will have the opposite polarization from the other two axes. An easy way to guarantee the polarizations are the same along each axis is to retroreflect the beams with a $\lambda/4$ waveplate and a mirror.

In the Blockade Experiment, a vapor cell MOT of ^{85}Rb generates a trap with a density of about 10^{10} atoms/cm^3 and an atom number of $\sim 10^6$. The diameter of the MOT is about half a millimeter. We achieve a larger, more dense atom sample by using a two-MOT setup where the vapor cell MOT serves as a primary trap to load a secondary trap located inside an ultra-high-vacuum chamber. In this way, atoms can be collected and cooled in the high-pressure vapor cell MOT, and then transferred into the low-pressure chamber where collision-induced atom loss rates are suppressed.

The transfer from the primary MOT to the secondary MOT is accomplished using a resonant beam with σ^+ polarization that drives the $5S_{1/2}$, $|F = 3, m_{\rm F}\rangle \rightarrow 5P_{3/2}$, $|F' = 4, m'_{\rm F} = 4\rangle$ cycling transition of ^{85}Rb. This creates a stream of atoms that move from the vapor cell into the vacuum chamber with a velocity of about 10 m/s. This

type of system is often referred to as a Low Velocity Intense Source, or, LVIS [44]. Using the LVIS, we obtain MOTs with a density of approximately 5×10^{10} atoms/cm^3 and an atom number of 5×10^6.

2.2 Imaging

2.2.1 Calculating atomic sample parameters

Atom numbers and densities are determined using a shadow imaging technique where resonant light is directed onto the atomic sample and "shadow" cast by the atoms is measured with a CCD camera. We define $I_0(x, y)$ to be the intensity profile of the incident laser beam and $I(x, y)$ to be the profile of the beam after passing through the trap. A brief calculation can show that the area density of the atoms is given by

$$N_A(x, y) = \frac{\Gamma h\nu}{2I_{\text{sat}}} \ln \frac{I(x, y)}{I_0(x, y)}$$

where Γ is the natural linewidth of the transition, $h\nu$ is the change in energy due to a single photon of the probe light, and I_{sat} is the saturation intensity. Note that this requires that $I \ll I_{rmsat}$ such that there are no line splittings and the linewidth of the transition is not broadened.

The total atom number, N, can be calculated by assuming the distribution

$$N_A(x, y) = N_A(0, 0)exp(-\frac{x^2 + y^2}{\sigma^2}) \tag{2.3}$$

and integrating over x and y. The characteristic width, σ, and the central area density can be calculated by fitting the shadow image data to a 2D Gaussian function. The central volume density can be calculated:

$$N_V(x,y,z) = N_V(0,0,0)exp(-\frac{x^2+y^2+z^2}{\sigma^2}) \tag{2.4}$$

which also gives the useful result:

$$N_V(0,0,0) = \frac{N_A(0,0)}{\sigma\sqrt{\pi}} \tag{2.5}$$

2.2.2 Direct versus 4F imaging

The imaging system used to collect the light for the shadow image can greatly affect the resolution that is obtained. If the shadow image is shone directly onto a CCD camera, the resolution is given by

$$\frac{1.22\lambda f}{D_{\text{atoms}}} \tag{2.6}$$

where λ is the wavelength of the light, f is the distance from the atoms to the camera, and D_{atoms} is the diameter of the atom cloud. For reasonable experimental conditions, the amount of blurring seen for a 1 mm MOT cloud is on the order of 100 microns. However, for a smaller atomic sample, such as the dipole trap discussed in Section 2.3, the atoms would be completely obscured by diffraction. In this case, we use a system known as 4F imaging, illustrated in Figure 2.5.

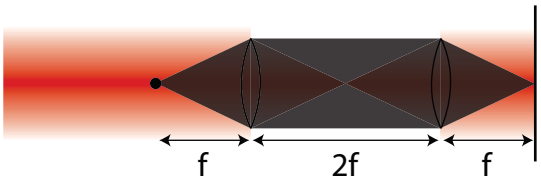

Figure 2.5: 4F imaging system for improved resolution of small atomic samples.

For 4F imaging, the resolution becomes

$$\frac{1.22\lambda f}{D_{\text{lens}}} \tag{2.7}$$

where now we have the diameter of the lenses in the denominator instead of the diameter of the atom cloud. This makes it possible for imaging of atom clouds with diameters of 10's of microns, provided a camera with small enough pixel size is used. A pixelfly high performance digital 12 bit CCD camera with a pixel size of 6.7 μm produces the images shown in Figure 2.6. Both of these images are formed using 4F imaging. While it would be possible to directly image the MOT, the dipole trap with a 15 μm diameter would be not be resolvable. Additionally, a further advantage of a 4F imaging system is that high frequency noise can be reduced by putting a filter on-axis between the two lenses.

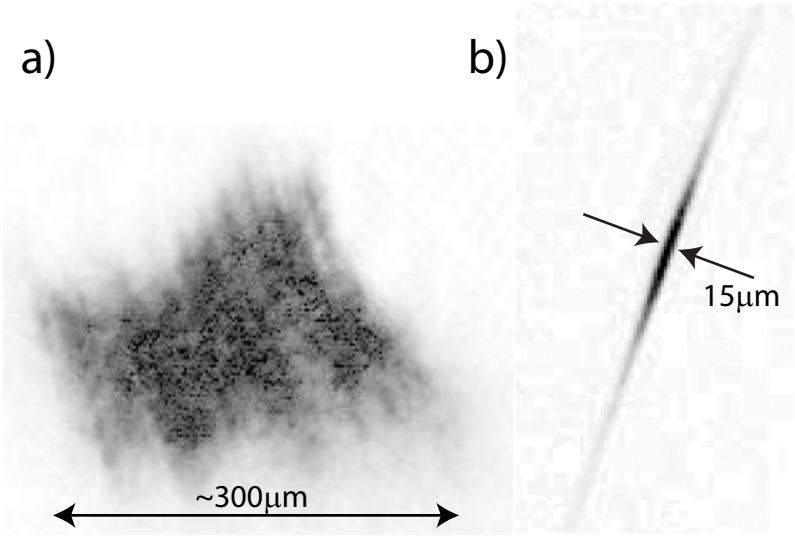

Figure 2.6: Images obtained with a 4F imaging system. a) Magneto-optical trap, density 5×10^{10} atoms/cm^3, atom number 5×10^6. b) Optical dipole trap, density 5×10^{11} atoms/cm^3, atom number 3×10^4.

2.3 Optical dipole traps

An atom trap with a high density and uniform density gradient is an advantage in many atomic physics experiments. In the Blockade Experiment, this is achieved

by creating an optical dipole trap after atoms are trapped in the MOT. Dipole traps are based on the light shift (AC Stark shift) that atoms experience in an intense laser field. Depending on the detuning of the dipole trap laser, a potential will be created for ground state atoms that attracts them to either the laser intensity maximum (red detuning) or minimum (blue detuning).

Dipole traps need to balance the dipole force with the radiation scattering force in order to trap effectively. For the derivation below, we assume a two-level atom but the equations extend easily to multi-level atoms. The two-level assumption is reasonable in this case because in ^{85}Rb, the transition from the $5S_{1/2}$ ground state to the intermediate 5P manifold dominates the contribution to the light shift and scattering rate. The interaction potential of the induced dipole moment of a two-level atom in an oscillating driving field is given by

$$U_{\text{dip}}(\overrightarrow{r}) = \frac{3\pi c^2}{2\omega_0^3}\frac{\Gamma}{\Delta}I(\overrightarrow{r}) \tag{2.8}$$

where Γ is the linewidth of the transition between the two levels, ω_0 is the laser frequency, Δ is the laser detuning from resonance, and $I(\overrightarrow{r})$ is the intensity profile of the laser. The scattering rate is given by

$$\Gamma_{\text{sc}}(\overrightarrow{r}) = \frac{3\pi c^2}{2\hbar\omega_0^3}\left(\frac{\Gamma}{\Delta}\right)^2 I(\overrightarrow{r}). \tag{2.9}$$

Equation 2.9 is obtained after applying the rotating wave approximation and assuming that $\omega/\omega_0 \sim 1$ (ω is the transition frequency between the two levels of the atom). From these equations, we see that the potential scales as I/Δ and the scattering rate scales as I/Δ^2. Because of this, optical dipole traps usually use large detunings and high intensities to keep the scattering rate as low as possible for a given potential.

Because the light shift of the atomic states is proportional to the intensity of the laser beam, by focusing the laser beam through the MOT, a potential well can be created that traps the atoms. The spatial intensity of a focused Gaussian beam with power P propagating along the z-axis is given by

$$I_{\mathrm{FB}}(r,z) = \frac{2P}{\pi w^2(z)} \exp\left(-2\frac{r^2}{w^2(z)}\right) \tag{2.10}$$

with

$$\omega(z) = \omega_0(1 + (z/z_r)^2)^{1/2} \tag{2.11}$$

$$z_r = \pi w_0^2/\lambda \tag{2.12}$$

where $\omega(z)$ is beam waist and z_r is the Raleigh length.

The optical potential can be determined from Equation 2.8:

$$U_{\mathrm{dip}}(\overrightarrow{r}) = \frac{3\pi c^2}{2\omega_0^3}\frac{\Gamma}{\Delta}\frac{2P}{\pi w^2(z)} \exp\left(-2\frac{r^2}{w^2(z)}\right). \tag{2.13}$$

The depth of the trap is given by $\hat{U} = |U(r=0, z=0)|$. We see that the potential in the radial direction is much steeper than in the axial direction, since z_r is a factor of $\pi w_0/\lambda$ larger than w_0. Our dipole trap is formed with a 5W, 1064 nm laser beam focused to a full width at half maximum of the intensity profile (FWHM) of 16 μm. The resonant transition frequency is 780 nm, and this results in a trap depth of 1.6 mK. Although the atoms in the MOT have a temperature near the Doppler limit of 140 μK, transfer into the dipole trap heats the atoms to about 1 mK. Transfer is accomplished by overlapping the dipole trap laser beam with the MOT for 30 ms. The MOT laser beams are then turned off for 38 ms in order to let untrapped atoms

fall out of the excitation region. This generates the cigar shaped trap shown in Figure 2.6.

2.4 Rydberg atom excitation

I excite ^{85}Rb Rydberg atoms out of the dipole trap or the MOT using the two-photon transition $5S_{1/2} \rightarrow 5P_{3/2} \rightarrow$ nS,nD. The wavelengths for the lower and upper transitions are 780 nm and 480 nm, respectively. Transitions to states that are not dipole-coupled (nP or nF, for example) can be accomplished as well by applying an electric field across the excitation region. Direction excitation from the 5S state into the Rydberg state can also be done using an ultraviolet laser at 297 nm [45]. A single-photon transition has the advantage that only one laser is required. However, UV light is difficult to generate at the required intensity and the matrix elements coupling the $5S_{1/2}$ state into the Rydberg state are much smaller than those for the two-photon transition. For these reasons, only the two-photon transition scheme is used here.

2.4.1 External cavity diode lasers

For the lower transition at 780 nm, we use home-built external cavity diode lasers (ECDLs). Diode lasers operate on the basic principle of a p-n junction in a direct band gap semiconductor. The gain region of the diode is surrounded by an optical cavity to form the laser. Electron-hole pairs in the semiconducter will annihilate and release photons. Photons that are emitted into a mode of the waveguide inside the cavity will bounce back and forth many times before they escape the cavity. The photons can cause further electron-hole pairs to combine which will in turn emit more photons. The mode of the laser is determined by the geometry of the cavity, and depending on the size of the cavity, the laser can either be single- or multi-mode.

To generate a single-mode beam, the laser waveguide must be on the order of the optical wavelength, such that only one mode is supported and a diffraction limited beam is formed.

The wavelength of the laser is determined by the semiconductor material and the modes of the optical cavity. One can tune the diode over a range of a few nanometers by adjusting the current density and the temperature of the diode. Adjusting the injection current will change the refractive index of the active area, which in turn changes the length of the cavity. Temperature influences both the path length and the gain curve of the semiconductor.

A diffraction grating placed after the collimation lens of the diode is also used to adjust the lasing wavelength. This arrangement is known as the Littrow configuration. The first order reflection off the grating is directed back into the diode, while the zeroth order is used as the laser output. There is a trade-off between stabilizing the laser with as much reflected power as possible, and still achieving the desired output power. In some cases, up to 50% of the power is reflected back into the diode.

2.4.2 Frequency doubled lasers

The upper transition 480 nm laser light is also generated by an ECDL, but because no commercial direct diode at 480 nm currently exists, I use a frequency doubled 960 nm laser from Toptica Photonics. The Toptica lasers in the Raithel laboratory use a non-linear crystal placed inside of a bow-tie cavity where the 960 nm light circulates and builds up in power. Second harmonic generation is a result of the first nonlinear term of the polarization induced in the crystal by the electric field of the 960 nm light [46]. This is discussed in more detail in Appendix C. Once light is phase matched into the crystal, some of the light is converted from 960 nm to 480 nm.

Ideally the conversion efficiency can approach 30 percent. The wavelength of the light can be adjusted via grating and current feedback (as discussed in Section 2.4.1 by about ±20 nm. After exciting the shutter of this laser, the 480 nm laser beam is coupled into an optical fiber and directed toward the atoms trapped in the vacuum chamber.

Part of the fundamental 960 nm beam is also coupled out of the system before it enters the doubling cavity. This beam has about 2-3 mW of power. It is used both to measure the wavelength of the laser, and is sent into a pressure-tuned, temperature stabilized Fabry-Perot cavity to stabilize the laser frequency.

2.4.3 Frequency stabilization of diode lasers

2.4.3.1 Saturated absorption spectroscopy

Our home-built, 780 nm diode lasers are stabilized to a Rb reference cell using saturated absorption spectroscopy. The Doppler broadened line shape of a gas of atoms is given by the Boltzmann distribution $e^{-mv_z^2/(2k_BT)}$. A laser beam interacts with atoms that have a given velocity class,

$$v_z = \left(\frac{\nu - \nu_1}{\nu_1}\right) c \tag{2.14}$$

where ν is the laser's frequency and ν_1 is the resonance frequency. The number of atoms absorbing is a Gaussian of the form,

$$e^{-mc^2(\nu-\nu_1)^2/\left(2k_BT\nu_1^2\right)} \tag{2.15}$$

The full width at half-maximum is therefore

$$\Delta\nu_{1/2} = \sqrt{8k_B \ln 2}\frac{\nu_1}{c}(T/M)^{1/2} \tag{2.16}$$

At room temperature this is on the order of a GHz. In order to improve the frequency resolution, one can use saturated absorption spectroscopy. The laser beam setup is shown in Figure 2.7.

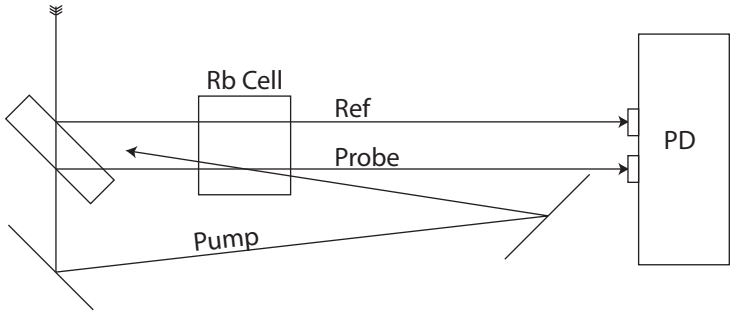

Figure 2.7: Beam configuration for saturated absorption spectroscopy.

When the pump and probe beams are not on resonance with an atomic transition, they interact with different velocity classes since they are counterpropagating (Figure 2.8). Only when they are on resonance will they interact with the same atoms (velocity class $v_z = 0$). This causes reduced absorption for the probe beam because the pump beam depletes the ground state atom population. This is observed by a narrow depression within the Doppler-broadened line. When the reference beam is subtracted such that the two Doppler signals cancel, this depression is the only feature that appears.

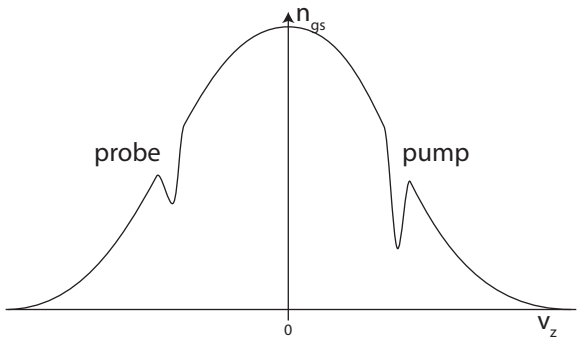

Figure 2.8: Pump and probe beams interacting with different velocity classes.

When two transitions share a common ground state and differ in frequency by less than the Doppler width, cross-over peaks occur. From Figure 2.9, it is clear that at some frequency, the same atoms will be resonant with ν_1 by the probe and ν_2 by the pump (and vice versa). We can easily calculate this frequency:

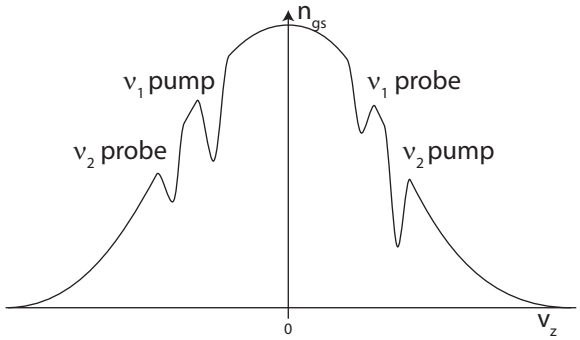

Figure 2.9: The origin of cross-over peaks.

$$\nu_1 = \nu_{\text{cross}} - \frac{v_{z1}}{c}\nu_{\text{cross}} \tag{2.17}$$

$$\nu_2 = \nu_{\text{cross}} + \frac{v_{z1}}{c}\nu_{\text{cross}} \tag{2.18}$$

Solving for the cross-over frequency results in

$$\nu_{\text{cross}} = \frac{\nu_1 + \nu_2}{2} \tag{2.19}$$

The peaks generated using this method of saturated absorption spectroscopy have a width of a few MHz and act as a suitable signal for locking the 780 nm lasers. Feedback to stabilize the laser frequency is provided by a lab-built PID servo connected to the current of the laser for fast feedback and the grating of the laser for slow feedback.

2.4.3.2 480 nm lasers

The Toptica 480 nm lasers involve two separate locks. The fundamental 960 nm laser light is locked to a home-built, pressure-tuned Fabry-Perot interferometer with free spectral range of 500 MHz and Finesse of about 40. [47]. This setup allows the frequency of the laser to be tuned smoothly by several hundred MHz. The doubling cavity is locked using the Pound Drever Hall technique [48].

2.4.4 Excitation region and detection of Rydberg atoms

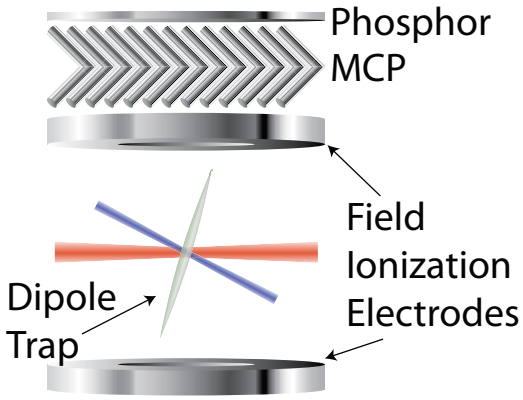

Figure 2.10: Qualitative view of beam geometry in the Rydberg excitation region and the detection electronics used for determining the number and state distribution of excited Rydberg atoms.

Figure 2.10 shows the 780 nm and 480 nm excitation beam geometry for the Blockade Experiment. The cigar shaped dipole trap is shown in the center (dipole trap beam not shown). The two beams are focused at the excitation region and propagate in orthogonal directions. Since the beam geometry changes slightly for the individual experiments presented in this thesis, further details on the geometries will be elucidated in each chapter.

As discussed in Chapter 1, Rydberg atoms are easily ionized with an electric field described by Equation 1.5. The electric field is applied using electrodes positioned above and below the excitation region as shown in Figure 2.10. The freed electrons are then pushed toward a micro-channel plate (MCP) with a phosphor screen located behind it. This technique, known as state selective field ionization (SSFI) not only provides a count of the number of Rydberg atoms excited, but also enables resolution of the atomic state distribution. The time at which the electrons reach the MCP can be converted into an electric field, and Equation 1.5 can be used to determine the state of the atom.

Each channel of the MCP is a continuous dynode electron multiplier, in which

the multiplication takes place under the presence of a strong electric field. The gain is 10^4 through a single channel, and $> 10^7$ for the stacked (Chevron) configuration. The phosphor screen transfers the electron energy into light with an efficiency of about 0.06 photons/eV/electron. The phosphor screen produces 5-10 mV pulses on top of the 5000 V applied to it. The DC signal is filtered out with a high voltage capacitor and sent to a pulse counter.

2.5 CryoMOT and Blockade Experiment differences

Both the CryoMOT and the Blockade Experiment use a double-MOT setup where atoms are first loaded in a primary MOT and then pushed into a secondary MOT as an LVIS. Rydberg excitation then proceeds out of the secondary MOT. As described above, the Blockade Experiment uses a six-beam MOT produced inside of a vapor cell. The CryoMOT, on the other hand, uses a pyramidal MOT configuration where the six beams necessary to create a MOT are generated by a single, large diameter beam incident on a set of four mirrors in a pyramidal configuration [49]. This beam also serves as the "pusher" beam to force atoms into the secondary MOT (this is the same type of LVIS as above). Atom densities and numbers for both methods are comparable, as are the vacuum pressures for the two chambers ($\sim 10^{-9}$ Torr).

The experimental repetition rate in the Blockade Experiment is 5 Hz, while the repetition rate in the CryMOT is 200 Hz. Although both experiments use a high intensity 1064 nm laser to form a dipole trap, the fast repetition rate of the CyroMOT experiment does not allow time for atoms outside of the dipole trap to fall out of the excitation region. This topic will be discussed further in Chapter 4 when we discuss ponderomotive optical lattices for Rydberg atoms.

Chapter 3 of this thesis discusses a rotary echo experiment performed with the

Blockade Experiment apparatus. Chapters 4, 5, and 6 each refer to the CryMOT experiment. Specifics of each experimental setup that do not pertain to all experiments will be detailed in the individual chapters.

CHAPTER III

Rotary Echo Tests of Coherence in Rydberg-atom Excitation

3.1 Excitation coherence in Rydberg atoms

The exaggerated properties of Rydberg atoms discussed in Chapter 1 lead to interactions that enable fundamental studies of quantum many-body systems [50, 51] and are the basis for applications in quantum information processing [1, 2]. Of particular interest is the Rydberg excitation blockade, described briefly in Section 1.3, which follows from the spectral characteristics of the entangled many-body states that describe systems of interacting Rydberg atoms. Due to these interactions, the energy separation of the levels $|N, 0\rangle$ and $|N, 1\rangle$ differs from that of the levels $|N, k\rangle$ and $|N, k+1\rangle$, where k is the number of Rydberg excitations and N the number of atoms that coherently share these excitations. The level shifts prohibit narrow-band photo-excitation into levels $|N, k\rangle$ with $k > 1$. The blockade has been observed via reduced excitation rates [28, 29, 45] and narrowed excitation number distributions [52]. More recently, resonant energy transfer between cold atoms in spatially separated cylindrical regions was observed [53], and the $|N, 0\rangle \rightarrow |N, 1\rangle$ and $|N, 1\rangle \rightarrow |N, 2\rangle$ transitions were spectroscopically measured [30].

One consequence of the coherent many-body nature of the states $|N, k\rangle$ is that the Rabi frequency between states $|N, 0\rangle$ and $|N, 1\rangle$ is given by $\Omega = \sqrt{N}\Omega_0$, where Ω_0

is the single atom Rabi frequency [2]. We can quickly derive this scaling by writing our ground and excited states,

$$|\psi_{\rm g}\rangle = |g_1, g_2 \ldots g_{N-1}, g_N\rangle \tag{3.1}$$

$$|\psi_{\rm e}\rangle = \frac{1}{\sqrt{N}} \sum_{i=1}^{N} |g_1, g_2 \ldots e_i \ldots g_{N-1}, g_N\rangle. \tag{3.2}$$

The Rabi frequency is given by

$$\Omega = \frac{\mu_z E}{\hbar} \tag{3.3}$$

$$= \frac{e\langle\psi_e|z|\psi_g\rangle E}{\hbar} \tag{3.4}$$

$$= \frac{eE}{\sqrt{N}\hbar} \sum_{i=1}^{N} \langle g_1, g_2 \ldots e_i \ldots g_{N-1}, g_N|z|g_1, g_2 \ldots g_{N-1}, g_N\rangle \tag{3.5}$$

$$= \frac{eE}{\sqrt{N}\hbar} N\langle g|z|e\rangle \tag{3.6}$$

$$= \sqrt{N}\Omega_0. \tag{3.7}$$

The scaling of the Rabi frequency Ω with $\sqrt{N}$, which indicates collective, coherent dynamics, has been measured experimentally [54]. However, experimental work aimed at measuring the $\sqrt{N}$-enhancement of the Rabi frequency has been complicated by the fact that measurements in extended atom samples yield sums over many excitation domains, leading to rapid dephasing of the Rabi oscillations. Because of density gradients within the sample, the number of atoms per excitation domain, N, varies substantially over the excitation volume. The blockade condition is described by

$$\frac{C_6}{r_b^6} \sim \Omega \tag{3.8}$$

for van der Waals interactions with r_b the blockade radius (the distance between excitations). The factor C_6 represents the strength of the van der Waals interaction and scales as n^{11}. The number of atoms, N, is given by the volume of the blockaded

region times the density,

$$N = \frac{4}{3}\pi \left(\frac{r_b}{2}\right)^3 \rho. \tag{3.9}$$

The blockade radius is divided by two in this case because r_b is the full distance between two Rydberg atoms. We can combine these two equations to yield some noteworthy scaling laws.

$$N = \left(\frac{C_6}{\Omega_0}\right)^{2/5} \left(\frac{4\pi\rho}{3}\right)^{4/5} \times 2^{-12/5} \tag{3.10}$$

$$r_b = \left(\frac{C_6}{\Omega_0}\right)^{2/15} \left(\frac{4\pi\rho}{3}\right)^{-1/15} \times 2^{1/5} \tag{3.11}$$

$$\Omega = C_6^{1/5}\Omega_0^{4/5} \left(\frac{4\pi\rho}{3}\right)^{2/5} \times 2^{-6/5} \tag{3.12}$$

We see that there is a weak, $\rho^{-1/15}$, dependence of the domain radius, r_b, on the local density and a $\rho^{2/5}$ dependence of the Rabi frequency Ω on the local density in the van der Waals regime [55]. The same treatment for the dipole-dipole regime yields a stronger $\rho^{2/3}$ dependence of the Rabi frequency on the local density. This further reenforces the fact that a measurement of the Rabi frequency in a mesoscopic ensemble of atoms is highly unlikely to yield results that show the coherent behavior of the atoms. Rydberg atom Rabi oscillations have previously been measured as a demonstration of the coherence of Rydberg atom systems [56], but the observation of many oscillation cycles requires that the number of Rydberg excitations be limited to one or two [38].

3.2 Rotary echo sequences

Echo schemes, such as spin and rotary echo sequences, have been used extensively in the past to overcome the effects of inhomogeneities in many different systems. The first studies used both spin and rotary echo methods to study the free precession of nuclear spins about a radio frequency field while in the presence of a large, DC

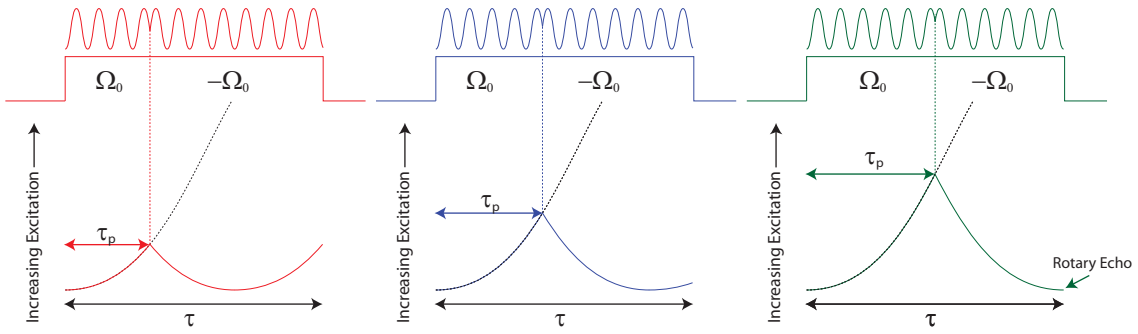

Figure 3.1: Rotary echo sequences with varying values of τ_p. As τ_p is increased, the amount of excitation at the end of the sequence changes accordingly. When the sign of the excitation is inverted halfway through the excitation pulse, all atoms will be back in the ground state (rotary echo).

magnetic field [57, 58]. In 2008, a rotary echo experiment was performed in a strongly interacting Rydberg gas to demonstrate coherence [39]. This experiment involved exciting atoms for a time τ_p, and then inverting the sign of the excitation amplitude. Here, I perform a similar experiment. I compare and contrast the methods used in Section 3.5.

In the rotary echo experiment presented here, I adjust the time τ_p as shown in Figure 3.1. An acousto-optic modulator driven by a radio-frequency (RF) pulse is used to generate the excitation laser pulse. In Figure 3.1, the RF pulse is represented by the oscillating curves at the top. Excitation inversion can be accomplished by flipping the phase of the RF by π, or 180 degrees. The dashed line represents how the excitation would evolve were there no excitation inversion. When the phase inversion occurs, the excitation process reverses and travels back down toward zero. If the inversion occurs halfway through the excitation pulse (far right panel of Figure 3.1), a rotary echo occurs at the end of the pulse, provided the excitation was coherent. The amount of signal remaining after such a sequence is a quantitative measure of the excitation coherence of the system.

A many-body pseudoparticle approach, where groups of blockaded atoms are

treated as "super-atoms", is well suited to model this experiment in the strongly blockaded regime where the number of blockaded atoms, N, is much greater than one [55, 59]. In the pseudoparticle approach, the Hamiltonian describing the excitation is given by [37]

$$\hat{H}(t) = \sum_j \hat{H}_{\rm j}(t) + \sum_{j<k} V_{\rm jk}|n_{\rm j}n_{\rm k}\rangle\langle n_{\rm j}n_{\rm k}| \tag{3.13}$$
$$\hat{H}_{\rm j}(t) = -\left[\Delta\omega + \epsilon\right]|n_{\rm j}\rangle\langle n_{\rm j}| + \frac{\Omega_0}{2}\sqrt{N_{\rm j}}(|g_{\rm j}\rangle\langle n_{\rm j}| + |n_{\rm j}\rangle\langle g_{\rm j}|).$$

Here, the interaction $V_{\rm jk}$ is between pseudoparticles and not individual atoms. The kets $|g_{\rm j}\rangle$ and $|n_{\rm j}\rangle$ correspond to pseudoparticle j being in the ground state $|N_{\rm j}, 0\rangle$ and excited state $|N_{\rm j}, 1\rangle$, respectively, $\Delta\omega$ is the laser detuning (approximately zero in our case) and ϵ is a mean-field energy shift due to distant excited atoms. If $\Omega_0 \to -\Omega_0$ at $t = \tau_{\rm p}$ and the terms ϵ and $V_{\rm jk}$ are negligible, the Hamiltonian in (3.13) exhibits near-perfect symmetry $\hat{H}(\tau_{\rm p} - t) = -\hat{H}(\tau_{\rm p} + t)$. Assuming that the excitation begins at $t = 0$, a rotary echo occurs at a time $2\tau_{\rm p}$, when all pseudoparticles will be back in the ground state, regardless of the inhomogeneity in $N_{\rm j}$. If ϵ and $V_{\rm jk}$ are significant and are not inverted, the Hamiltonian lacks this symmetry. The resultant decoherence of systems containing multiple pseudoparticles causes a reduction in echo visibility.

In this experiment, the rotary echo method is employed to study the effect of Rydberg-atom interactions on the coherence of excitation processes in many-body Rydberg-atom systems. The echo signal is recorded by varying τ_p for a fixed pulse length τ and counting the number of excitations. I show how the visibility of the rotary echo diminishes as the interaction strength, W, between Rydberg atoms is increased. I vary W by taking advantage of the interaction process $2 \times n{\rm D}_{5/2} \to (n+2){\rm P}_{3/2} + (n-2){\rm F}_{7/2}$, which for Rb is nearly resonant at the principal quantum

number n=43. This is a natural Förster resonance, as referred to in Section 1.3. Due to this resonance, W varies strongly as a function of n in the vicinity of n=43, allowing me to realize cases ranging from minimal interactions (n=40) to strong interactions (n=43) over a narrow range of n [27]. Rydberg excitation spectra, taken with and without excitation inversion, provide an alternate, equally valid test of coherence. Here, I highlight the importance of atom-atom interactions in rotary echoes as well as the equivalence of such echoes with spectroscopic information for the demonstration of coherence.

3.3 Experimental setup for rotary echo tests

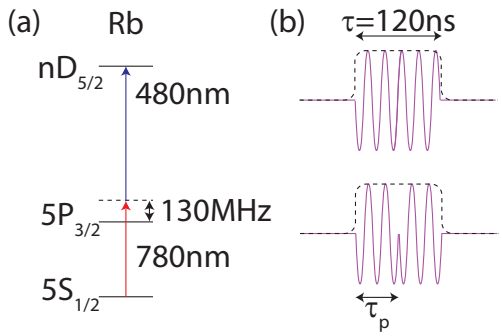

Figure 3.2: Experimental setup. (a) Rydberg atom excitation scheme. (b) RF signal sent to the acousto-optic modulator used to control the upper transition laser pulse for the case without phase inversion (top) and with phase inversion at time τ_p (bottom).

Figure 2.10 in Section 2.4.4 shows the trap setup used to conduct this experiment. I cool and trap ^{85}Rb atoms in a MOT and then form an optical dipole trap with a 5 W, 1064 nm laser beam focused through the center of the trap. As described in Section 2.3, the dipole trap has a temperature of approximately 1 mK and a peak density of 2.5×10^{11} atoms/cm^3. Figure 3.2 shows the excitation scheme. The excitation is performed with two narrow-linewidth, coincident laser pulses propagating in orthogonal directions, as shown in Figure 2.10. The pulses have a square temporal profile with a width of 120 ns. The lower transition laser beam is focused to

a full-width at half-maximum (FWHM) of the intensity of 18 μm and has a peak Rabi frequency of $\Omega_1 = 2\pi \times 10$ MHz. The laser is detuned from the intermediate $5P_{3/2}$ state by $\delta = 2\pi \times 130$ MHz. The upper transition laser beam is focused to a FWHM of 8 μm, and has a peak Rabi frequency of $\Omega_2 \approx 2\pi \times 10$ MHz. Both lasers have a linewidth $\delta\nu/2\pi \lesssim 2$ MHz. These conditions result in a Rabi frequency at the two-photon resonance of $\frac{\Omega_1\Omega_2}{2\delta} \approx 2\pi \times 400$ kHz. In order for the excitation to remain coherent, it is important that spontaneous emission out of the intermediate $5P_{3/2}$ state be negligible. The scattering rate is given by

$$\gamma_{\text{scat}} = \frac{s_0\Gamma/2}{1 + s_0 + (2\delta/\Gamma)^2} \tag{3.14}$$

where $\Gamma = 2\pi \times 5.98$ MHz is the linewidth of the transition and s_0 is the on-resonance saturation parameter, $2|\Omega|^2/\Gamma^2$. For the parameters stated above, there are less than 0.01 spontaneous emission events per atom on the lower transition during one experimental cycle. For typical experimental conditions there are about 500 ground-state atoms in the excitation volume. The number of atoms per blockaded region, N, reaches a maximum of about 100 at n=43. I apply an SSFI ramp 100 ns after excitation to ionize the Rydberg atoms, and detect the freed electrons with a microchannel plate detector. To perform the rotary echo experiment, I shift the phase of the radio frequency (RF) applied to the acousto-optic modulator (AOM) that controls the upper-transition light pulse by π after a time τ_p, as illustrated in Figure 3.2(b). This accomplishes the inversion of Ω_0 in (3.13). The phase shift is done by using a 180 degree power splitter connected to an RF oscillator. The two outputs of the splitter (Mini-Circuits part number ZFSCJ-2-4-S) are 180 degrees out of phase. These output are connected to a high isolation RF switch (ZASWA-2-50DR+) to change between the two signals, followed by a second high isolation switch to turn the optical pulse on and off. Total losses through the system are approximately 7dB, and

the signal is amplified by +29dB (ZRL-700+) before being directed to the AOM. It is worth noting that a setup using an RF oscillator and a high isolation switch often provides far superior performance to that of a typical AOM driver (DE-802 series from IntraAction Corporation or DRFA40Y series from Electro-Optical Products Corporation). The RF leakage from these drivers is on the order of 10^{-4}, but even the small amount of light produced by this leakage constantly interacting with the Rydberg atom excitation region can significantly distort the results of an experiment. The isolation for a Mini-Circuits ZASWA, on the other hand, is 10^{-10} at 100 MHz.

3.4 Echo spectra for a variety of Rydberg states

Figure 3.3(a) shows the rotary echo signal for the Rydberg state $40D_{5/2}$. For each data point, the atoms are excited for a time τ_p and then the evolution is reversed for a time $\tau - \tau_p$ (pulse width $\tau = 120$ ns). Each point represents 200 averages. Similar to a convention used in [39], for the visibility of the echo I use

$$\frac{N_R(\tau_p = 0) + N_R(\tau_p = \tau) - 2\,N_R(\tau_p = \tau/2)}{N_R(\tau_p = 0) + N_R(\tau_p = \tau) + 2\,N_R(\tau_p = \tau/2)}. \tag{3.15}$$

From the definition in Equation 3.15, the visibility will range from 0 to 1, with an increased visibility representing greater coherence in the system. The visibility obtained for $40D_{5/2}$ is 0.67 ± 0.11, which is greater than any of the echo visibilities achieved in Ref [39]. Standard error propagation techniques are used to arrive at the quoted uncertainty. The slight asymmetry of the curve is most likely due to small asymmetries in the short pulse used for excitation. Reasons why the visibility does not reach 100% could be because of residual interactions (which exist even for n=40) and the laser linewidths, which affect the magnitudes of the terms V_{jk} and $\Delta\omega$ in (3.13), respectively.

According to the principle that time-domain and spectroscopic information are

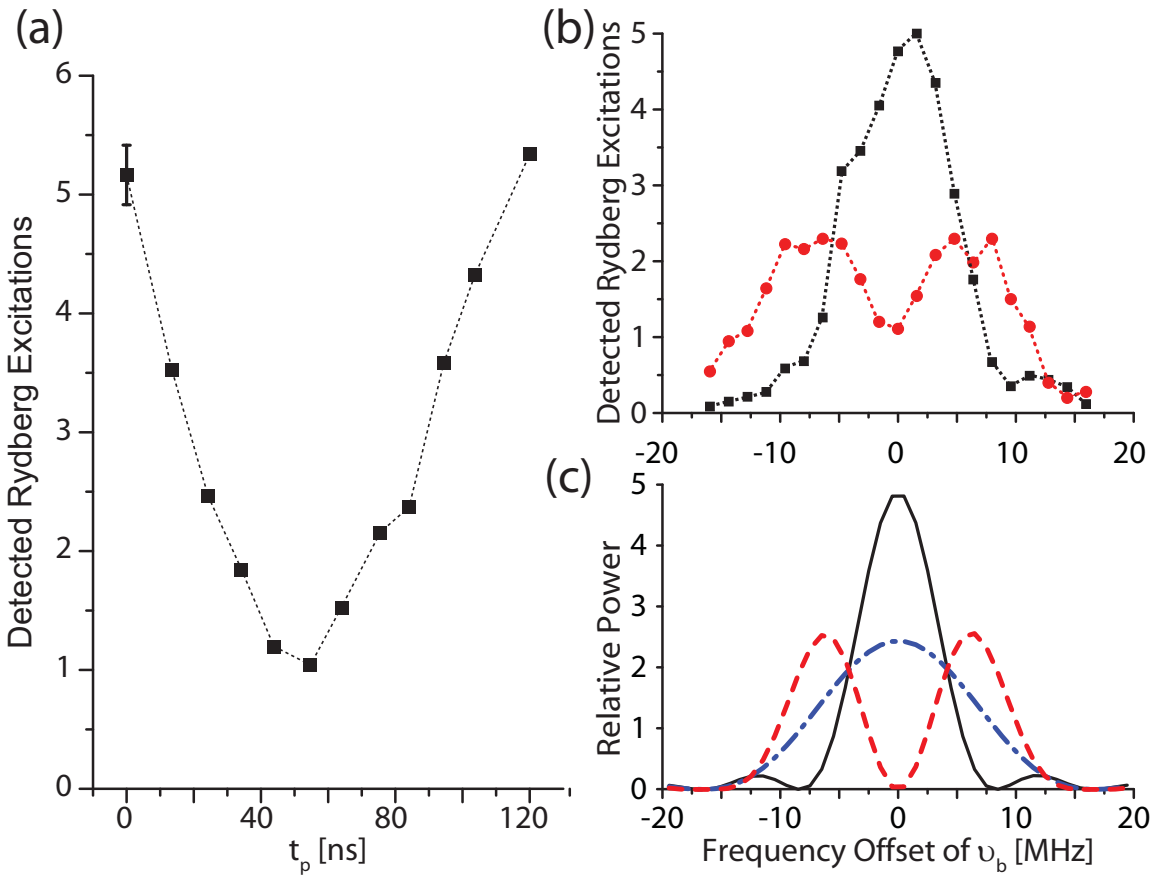

Figure 3.3: Echo data and spectra for the state $40D_{5/2}$ for square excitation pulses. (a) Number of Rydberg atoms for pulses with duration $\tau = 120$ ns, detected as a function of τ_p, the time of the phase flip with respect to the beginning of the excitation pulse. (b) Excitation spectra without phase inversion (black squares) and with phase inversion at $\tau_p = 60$ ns (red circles). c) Power spectra of three different square pulses. Black line: $\tau = 120$ ns and constant phase. Red dashed line: $\tau = 120$ ns and phase flip at $\tau_p = \tau/2$. Blue dash-dotted line: $\tau = 60$ ns square pulse without phase flip and with twice the intensity of the other two pulse types.

generally equivalent, evidence for the coherence of the evolution can not only be obtained via rotary echoes but also by spectroscopy of the excited Rydberg level. I record the number of Rydberg excitations as a function of the 480 nm excitation laser frequency, ν_b, with and without the phase inversion of the RF applied to the AOM. Figure 3.3(b) shows spectra obtained by scanning ν_b across the two-photon resonance. The fact that the spectrum with phase inversion (circles) in Figure 3.3(b) closely resembles the power spectra of a pulse with a phase flip at $\tau_p = \tau/2$ (dashed

line in Figure 3.3(c)) confirms the coherence of the excitation. In both the measured spectrum and the corresponding calculated power spectrum (dashed curve), the separation between the two resolved peaks is ~ 13 MHz. If the Rydberg excitation was not coherent, the excitation pulse with phase inversion at $\tau_p = \tau/2 = 60$ ns would act as two individual 60 ns pulses. These would generate an excitation spectrum with twice the width and half the amplitude of the spectrum obtained with the 120 ns pulse absent the phase inversion (dash-dotted line in Figure 3.3(c)).

Noting that the pulse used in Figure 3.3(b) represents a coherent sequence of two half-pulses (of opposite phase), it is not surprising that the spectrum in Figure 3.3(b) resembles spectra obtained with Ramsey's well-known separated oscillatory field method [60]. In both cases, the presence of spectral modulations signifies coherent evolution. Differences between typical conditions used in the separated-field method and the present work include the time separation between the pulses (vanishing in our case), and the significance of the detuning during excitation and excitation saturation (both high in our case).

To measure the effect of Rydberg-Rydberg interactions on the echo visibility, I enhance the interaction strength, W, by varying the n-value of the excited Rydberg state. I verify the relative interaction strengths of different Rydberg states by recording the number of Rydberg excitations as a function of the upper transition laser power for different n. As a consequence of the Rydberg excitation blockade, the interactions between atoms lead to saturation in the number of excitations as the laser power is increased [45]. The saturation is more prominent for more strongly interacting Rydberg states. The inset of Figure 3.4 shows the number of detected Rydberg excitations as a function of upper transition laser power for several Rb $n\mathrm{D}_{5/2}$ states. The count number for $40\mathrm{D}_{5/2}$, the state with the weakest interactions studied

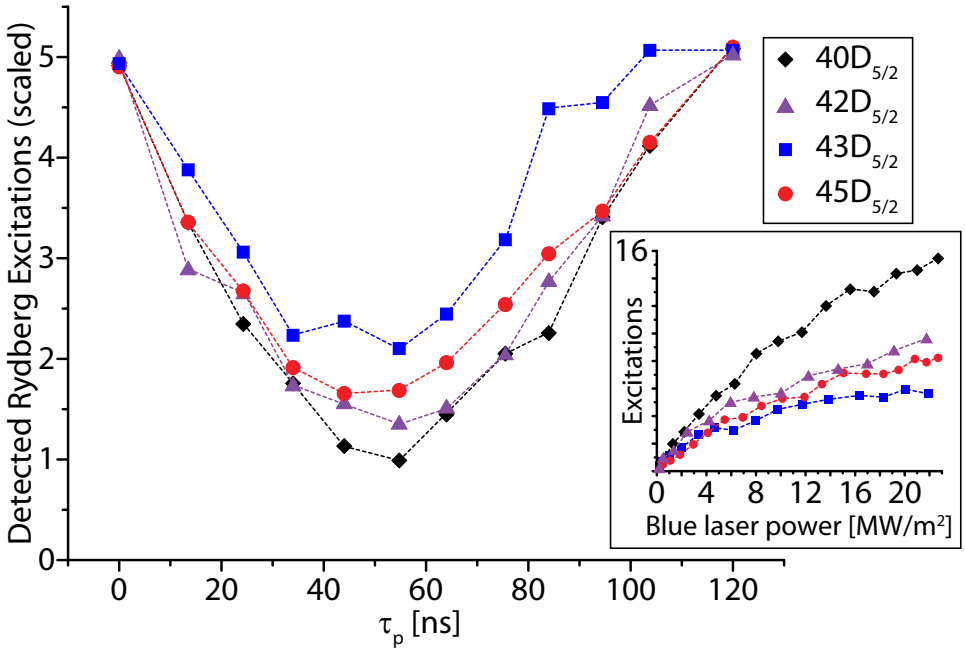

Figure 3.4: Number of Rydberg atoms detected as a function of τ_p for the states $40D_{5/2}$ (black diamonds), $42D_{5/2}$ (green triangles), $43D_{5/2}$ (red circles), and $45D_{5/2}$ (blue squares). For ease of comparison, all curves are scaled to a value of five at $\tau_p = 0$ and 120 ns. The inset shows the number of Rydberg atoms detected as a function of upper transition laser power for the same set of states. The degree of saturation reflects the strength of atom-atom interactions.

in this thesis, shows very little saturation. Conversely, the count number saturates significantly for $43D_{5/2}$, the state exhibiting the strongest interactions (because it is closest to the center of the Förster resonance). For the states $42D_{5/2}$ and $45D_{5/2}$ I observe intermediate saturation behavior, according to their moderate interaction strengths (see Figure 3a of [27]). I record the echo signal for $n = 42$, 43, and 45 using the same experimental procedure as described above. The upper transition laser power used is scaled proportional to n^{*3}, with effective quantum number n^*, to give the same single-atom Rabi frequency for each state; for $n = 43$ the intensity is 5.8 MW/m^2. The results are shown in Figure 3.4. The curves are multiplied by scaling factors such that the average values of the counts for $\tau_p = 0$ and $\tau_p = 120$ ns are five for each curve. The scaling factors reflect the varying degree of interactions; stronger interactions lead to more saturation and thus larger scaling factors (see Fig-

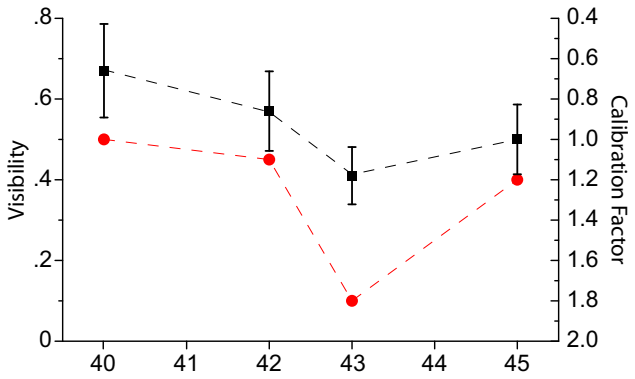

Figure 3.5: Echo visibilities (squares, left axis) and calibration factors (circles, right axis) for each n-state examined. The points in this graph follow a very similar trend because of the correlation between saturation of Rydberg atom excitation and loss of echo visibility.

ure 3.5). From (3.15), the echo visibilities for n=40, 42, 43, and 45, obtained from the data shown in Figure 3.4, are 0.67±0 11, 0.57±0.10, 0.41±0.07, and 0.50±0.09, respectively. The trends of echo visibility and saturation behavior as a function of n are compared in Figure 3.5. The figure clearly demonstrates that saturation behavior and loss in echo visibility are closely correlated.

Finally, I have recorded excitation spectra analogous to the spectrum shown in Figure 3.3(b) for n=42, 43, and 45. The results are shown in Figure 3.6. The visibility of the two side peaks for the case where the excitation amplitude is inverted (red circles) decreases as the atom-atom interaction strength increases. The echo data and spectroscopic data presented here allow us to conclude that increased atomic interactions and the resultant decoherence in pseudoparticle evolution have complementary consequences in the dynamics and the spectral properties of many-body Rydberg systems, namely a loss of visibility in rotary echo curves (Figure 3.4) and a loss of contrast in spectral data (Figure 3.3(b) and Figure 3.6).

3.5 Comparison to past studies

I first discuss my results in context with recent theoretical calculations performed by Hernandez *et. al* [37]. I first note that the system studied in this thesis is characterized by many-body interactions between pseudoparticles (as opposed to interactions between individual atoms); this statement follows from the saturation behavior shown in Figure 3.4 and from estimates of N_j based on the measured ground-state and Rydberg atom numbers. In Ref. [37], echo visibilities are calculated for three cases: a sparse system where the interaction V_{jk} is negligible, a perfectly blockaded system in which only one Rydberg excitation is allowed in the entire excitation volume, and an intermediate system in between these two limiting cases. A perfect echo visibility is achieved for the first two cases, while the echo is reduced for the third case when V_{jk} is no longer negligible. The results for the state $40\mathrm{D}_{5/2}$ correspond to the limiting case in which the interaction between particles is at a minimum and, hence, the best echo visibility is achieved. The results for the states $42\mathrm{D}_{5/2}$, $43\mathrm{D}_{5/2}$ and $45\mathrm{D}_{5/2}$ correspond to the intermediate case in [37], where the role of atomic interactions is sufficiently strong to cause a reduction in echo visibility, but not strong enough to turn the entire excitation volume into a single excitation domain.

Ref. [37] strongly suggests that the loss in visibility in the intermediate regime is a result of an increased interaction strength between pseudoparticles which inhibits the complete inversion of the Hamiltonian in Equation 3.13. Here, I interpret the results in a different manner. First, I compare the terms $\sqrt{N_{\mathrm{j}}}\Omega_0$ and V_{jk} in (3.13). I assume a power law, $W \propto C_{\mathrm{p}} d^{-p}$, for the Rydberg-atom interaction W as a function of interatomic separation d, and strong saturation, $\sqrt{N_{\mathrm{j}}}\Omega_0 \gg \delta\nu_L$ (this means that the number of atoms per blockaded region is much greater than unity). The excitation

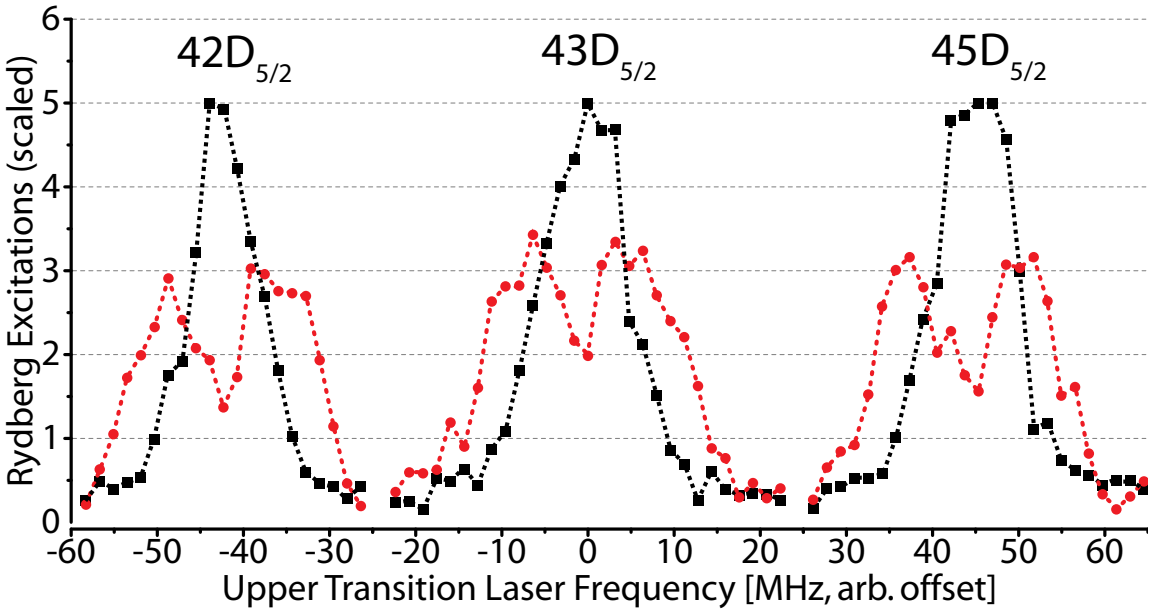

Figure 3.6: Excitation spectra for the states $42D_{5/2}$, $43D_{5/2}$, and $45D_{5/2}$. The black squares show the case where the excitation amplitude is constant throughout the pulse, and the red circles show the results when $\tau_p = \tau/2$. The number of detected excitations is scaled to give a maximum excitation number of five.

domain radius, r_{b}, is then found to scale as

$$C_{\mathrm{p}}^{2/(2p+3)}\rho^{-1/(2p+3)} \tag{3.16}$$

(using the same steps that led to Equation 3.12). Here, $\delta\nu_L$ is the laser linewidth, ρ is the ground-state atom density, and $p = 3$ for resonant electric-dipole interactions and $p = 6$ for van-der-Waals interactions. To find V_{jk}, which is the interaction strength between pseudoparticles, the interaction between individual atoms within each pseudoparticle must be considered. The exact interaction is given by a sum over the interactions between all individual atoms separated by variable distances. This sum must be weighted by the probability to find two atoms separated by a given distance. Thus, we have $V_{\mathrm{jk}} = \langle C_{\mathrm{p}} d_{\mathrm{lm}}^{-p} \rangle$, where the indices l and m identify a random atom pair with atom l in pseudoparticle j and atom m in pseudoparticle k, and $\langle ... \rangle$ identifies an average with weighting factor given by the probability of finding a pair

of Rydberg excitations on atoms l and m. Assuming an efficient blockade, consistent with the experimentally observed saturation, one may expect $\langle d_{\mathrm{lm}}^{-p} \rangle \approx [2r_{\mathrm{b}}]^{-p}$. This means that instead of calculating a weighted average to find the mean distance between individual atoms, one can simply use the center-to-center distance between pseudoparticles. If these two values are indeed equal, it follows from Equation 3.8 that $\sqrt{N_{\mathrm{j}}}\Omega_0$ and V_{jk} are identical. Then, from Equation 3.16, I find that $\sqrt{N_{\mathrm{j}}}\Omega_0$ and V_{jk} scale as $\rho^{p/(2p+3)} C_{\mathrm{p}}^{3/(2p+3)}$.

The consequence of the above is that the time-dependent Schrödinger equation that follows from Equation 3.13 becomes invariant under variations of density, ρ, and interaction strength, C_{p}, if an excitation pulse is used that is invariant as a function of a scaled time, $\tilde{t} \propto t\rho^{p/(2p+3)} C_{\mathrm{p}}^{3/(2p+3)}$ (t is the physical time). So, although the magnitude of the Hamiltonian scales with ρ and C_{p}, we can counteract this increase by reducing the duration of the excitation by the same factor. Since in my experiment I keep the timing of the physical pulse fixed, stronger interactions correspond to longer scaled times $\tilde{t}$. Since longer scaled times lead to more strongly excited domains, I conclude that the reduced visibilities, observed for stronger interactions in the intermediate regime, are a result of driving the domains further into their first excited states, $|N_{\mathrm{j}}, 1\rangle$. Interestingly, in this model the reduced visibilities *do not* result from an enhancement of the V_{jk}-terms relative to the $\sqrt{N_{\mathrm{j}}}\Omega_0$-terms in (3.13) as suggested by Ref [37]. I note that longer scaled times can also be achieved by simply increasing the physical pulse duration while keeping all other conditions the same. I did, indeed, observe a trend that longer physical pulse durations lead to less visible echoes.

A critical assumption made in the above is that $\langle d_{\mathrm{lm}}^{-p} \rangle \approx [2r_{\mathrm{b}}]^{-p}$. In simpler language, this means that it is reasonable to represent all atoms within a blockaded volume with a single pseudoparticle to find the interaction strength between blockaded

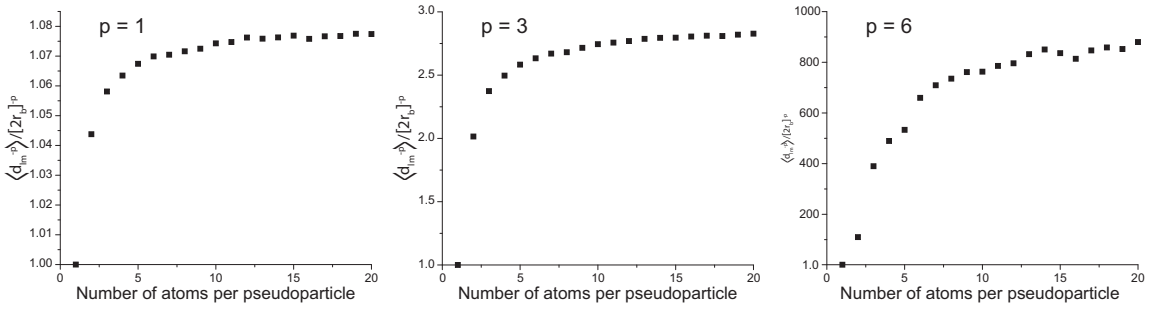

Figure 3.7: Ratio of $\langle d_{\rm lm}^{-p} \rangle$ to $[2r_{\rm b}]^{-p}$ for $p = 1$, 3, and 6 and $r_{\rm b} = 5\mu$m.

regions. In a perfectly blockaded atom sample, the validity of this assumption is ensured by a drastic suppression of the pair correlation function of Rydberg excitations for Rydberg-Rydberg separations $d < 2r_{\rm b}$ [61]. Systems with a reduced blockade effectiveness will exhibit a less dramatic suppression of the pair correlation function at small distances. A reduction in blockade effectiveness can result for several reasons, including the excitation bandwidth, anisotropy and "dead angles" (angles where the dipole-dipole interaction is reduced to zero) in the Rydberg-Rydberg interaction, and motion-induced decoherence during excitation. A loss of structure in the Rydberg pair correlation will obviously lead to a more random spread of Rydberg excitations over all atoms in the sample. Consequently, the condition $\langle d_{\rm lm}^{-p} \rangle \approx [2r_{\rm b}]^{-p}$ will trend towards $\langle d_{\rm lm}^{-p} \rangle \gg [2r_{\rm b}]^{-p}$ (for large and positive p). I have verified this trend in a two-dimensional simulation where I randomly place atoms within a circular area, then calculate both $\langle d_{\rm lm}^{-p} \rangle$ and $[2r_{\rm b}]^{-p}$. The results of this simulation are shown in Figure 3.7 for $p = 1$, 3, and 6 and $r_{\rm b} = 5\mu$m. The trend simply arises from the likelihood of finding Rydberg-atom pairs at small separations $d_{\rm lm}$. A few instances of small separations are sufficient to strongly inflate the expectation value for $\langle d_{\rm lm}^{-p} \rangle$, because $d_{\rm lm}^{-p}$ quickly diverges at small $d_{\rm lm}$ (for large and positive p). Thus, the assumption $\langle d_{\rm lm}^{-p} \rangle \approx [2r_{\rm b}]^{-p}$, the effectiveness of the Rydberg excitation blockade, and

the validity of the model underlying Equation 3.13 are intimately related to each other.

In the following, I compare our results with a recent experiment described in [39]. For the case of least interaction ($n = 40$), I find a maximum echo visibility of 0.67, which is about 0.10 higher than the largest echo visibility obtained in [39], recorded in their case of lowest density. In [39], a trap temperature as low as 3.8 μK was used, which allowed for longer coherence times than would be obtainable in our 1 mK trap. The highest trap density used in [39] was $\sim 5 \times 10^{13}$ atoms/cm^3 and typical excitation pulse lengths were $\sim$ 500 ns. I have shown in the present experiment that an excellent echo visibility is achievable in a much hotter sample by performing the experiment with shorter pulses and using densities that are about two orders of magnitude lower than those used in [39]. A substantial difference between the work in [39] and our work is that our work has been performed with D-Rydberg levels, while the data in [39] have been obtained with the $43S$ level. The fact that I observe substantial rotary echoes despite that difference is noteworthy for two reasons. First, $D_{5/2}$-levels in Rb have stronger, attractive and anisotropic interactions, while S-levels have weaker, repulsive and isotropic interactions. The $nD_{5/2}$-states in Rb shift because of couplings to states with angular momenta that allow for so-called "Förster zeroes" (i.e., binary molecular Rydberg states with little interaction [62]), while S-states do not have Förster zeroes. Our results show that these differences do not preclude considerable echo visibility in systems of interacting Rydberg atoms. Second, the $nD_{5/2}$-levels of Rb exhibit a Förster resonance at $n = 43$ while S-levels exhibit a more generic van-der-Waals-type interaction. The Förster resonance leads to substantial populations of Rydberg levels in the Förster-resonant states, as demonstrated earlier [12]. The results for $43D_{5/2}$ presented here show that the

Förster-resonance-induced state mixing does not cause a breakdown of echo visibility.

3.6 Conclusion and future developments

In this chapter, I have demonstrated coherent excitation of Rb $nD_{5/2}$ Rydberg atoms using a rotary echo method. Echo signals and excitation spectra are found to be equal means of providing evidence of such coherence. I have varied the strength of the atom-atom interactions by performing the experiment with Rydberg states near a Förster resonance where the interaction features an abrupt change in magnitude and a zero-crossing at n=40. I have shown that the echo visibility is reduced as the strength of the interaction increases. I have interpreted this behavior by examining the Hamiltonian of the system given in (3.13). To improve the echo visibility in the case of strongly interacting Rydberg-atom systems, in future work one may look for ways to invert all terms in the Hamiltonian given in (3.13) (as opposed to just the terms $\sqrt{N_j}\Omega_0$). This could be accomplished by exploiting the abrupt change in sign of atomic interactions in the vicinity of Förster resonances [37].

CHAPTER IV

State-dependent Energy Shifts of Rydberg Atoms in a Ponderomotive Optical Lattice

So far, I have examined excitation coherence in a mesoscopic ensemble of atoms using a rotary echo technique. A system with a coherence time longer than the quantum gate time is one of the DiVincenzo requirements for successful quantum computation, as discussed in Section 1.2. In this chapter, I consider a novel type of Rydberg atom trap that will help in meeting three of the remaining four requirements, including scalability, qubit initialization, and qubit readout.

Since the development of laser cooling and trapping of atoms in the 1980's, the idea that atoms could be organized and stored via the AC Stark shift produced by fields of interfering laser beams has been studied in numerous theoretical and experimental contexts, many of which are reviewed in detail in Ref. [63]. The optical lattice potential can be modeled exactly and the lattice parameters can be controlled precisely via the laser beam geometry, intensity, frequency and polarization. This makes the optical lattice a very attractive system for a breadth of physics subfields. Some recent studies include investigations of effects in condensed matter systems such as interacting fermions in periodic potentials (3D optical lattice) [64], purely quantum mechanical effects such as quantum random walks to distribute atoms in a lattice [65], and the generation of entanglement for quantum information [66].

Optical lattices present a unique opportunity to create Rydberg atom traps with suppressed collisions, long storage times, and minimal trap-induced shifts compared to other techniques [67]. Microwave spectroscopy of Rydberg atoms trapped in an optical lattice will allow for high precision spectroscopy of quantum defects and the Rydberg constant [40]. Microwave modulations of the lattice could be used to probe highly dipole-forbidden transitions between Rydberg states [41]. Perhaps most significantly, Rydberg atom lattices will be ideal for quantum information experiments exploiting the strong electrostatic interactions between the atoms [2]. Research groups in Paris and Wisconsin have each independently created an entangled hyperfine-hyperfine ground state quantum bit using the Rydberg state to generate the entanglement [25, 26]. However, one of the major obstacles in these experiments is the fact that the Rydberg state is not trapped. Thus, any time an atom is excited into the Rydberg state, it can freely leave the trapping region. In fact, both of these experiments used dipole traps to localize their ground state atoms, which produces an *anti*-trapping force on any atom in the Rydberg state. Both groups report significant atom loss: 39% for the Paris group and 17% for the Wisconsin group[2], which could be improved dramatically if there existed a trapping potential for the Rydberg state in addition to the hyperfine ground states.

In this Chapter, I use microwave spectroscopy to measure trap-induced level shifts of Rydberg atoms in an optical lattice. I show how the shifts depend on both the light field's spatial variation and the Rydberg atom's state. This method of microwave spectroscopy allows analysis of Rydberg atom trajectories within the lattice, the characterization of which is a prerequisite for using lattices as trapping devices.

[2]The reported fidelities of 0.75 and 0.58 for the Paris and Wisconsin group, respectively, were adjusted to include only cases where atoms were not lost from the trap.

4.1 The ponderomotive energy

The spatial extent and large number of nearly degenerate states in Rydberg atoms makes the study of Rydberg atoms in optical lattices distinct in relation to their ground-state atom counterparts. For ground-state atoms, the atom-field interaction is between bound states. The trapping force is due to light shifts induced by laser beams with a frequency nearby a resonance between the ground state and one or a few nearby bound excited states. The light shift for a Rydberg atom is not as straightforward, since optical transitions between Rydberg atoms do not exist. Following the calculation for the ground-state light shift, it would be necessary to consider the effect of virtual transitions to all available atomic states as well as the continuum. An alternate method involves considering that the quasi-free Rydberg electron experiences a position dependent ponderomotive force, much like a free electron. The ponderomotive shift is the time averaged kinetic energy of a free electron in an oscillating electric field, and is given by

$$V_{\mathrm{p}} = \frac{e^2|\mathbf{E}|^2}{4m_e\omega^2}, \tag{4.1}$$

where $-e$ and m_e are the electron charge and mass, respectively, and $\mathbf{E}$ is a slowly varying electric field with angular frequency ω. This result can be easily derived for a standing wave optical lattice propagating along z and polarized along x where the electric field takes the form,

$$\begin{aligned}\mathbf{E}\left(\mathbf{r},t\right) = E_x\left(z,t\right)\hat{x} \quad &= E_{0x}\left[\cos\left(\omega t - kz\right) + \cos\left(\omega t + kz\right)\right]\hat{x} \\ &= 2E_{0x}\cos\left(\omega t\right)\cos\left(kz\right)\hat{x}. \end{aligned} \tag{4.2}$$

The electric field induces a driven oscillation of the electron that is sometimes referred to as a "quiver" motion. The acceleration and velocity of the motion are

given by,

$$\ddot{x} = \frac{eE_x(z,t)}{m_e}\hat{x} \tag{4.3}$$
$$= \frac{2eE_{0x}}{m_e}\cos(kz)\cos(\omega t)$$
$$\dot{x} = \frac{2eE_{0x}}{\omega m_e}\cos(kz)\sin(\omega t) \tag{4.4}$$

assuming that the initial velocity is zero. The time averaged kinetic energy is then,

$$\begin{aligned} V_{\mathrm{p}} = & \ \tfrac{\omega}{2\pi}\int_0^{\frac{2\pi}{\omega}} \tfrac{1}{2} m_e \dot{x}^2 dt \\ = & \ \tfrac{e^2[2E_{0x}\cos(kz)]^2}{4m_e\omega^2} \end{aligned} \tag{4.5}$$

This equation has the same form as Equation 4.1. The force on the quasi-free Rydberg electron due to the ponderomotive shift forces the Rydberg electron (and thus the bound nuclear core) toward regions of low laser field intensity. In an optical lattice, this potential is periodic in space and acts as a grating off of which free electrons can be diffracted (the Kapitza-Dirac effect [68]). The ponderomotive shift on Rydberg electrons has been studied in a number of contexts, not always yielding consistent results. The measurement is complicated by the fact that it is difficult to accurately characterize the exact laser intensities experienced by the atom during the experiment. Small misalignment of the employed laser beams will cause a reduction of the measured Stark shift but still result in a shift that scales linearly with the beam intensity, masking the misalignment issue. The ponderomotive shift on Rydberg electrons has been studied in references [69, 70] and, for instance, gives rise to observable structures in above-threshold ionization [71, 72]. In Ref. [70], AC Stark shifts of Xe Rydberg atoms in high-intensity laser fields were measured, and the results were in excellent agreement with ponderomotive predictions. The authors

discuss in detail the extreme care taken to accurately measure all beam intensities. Ref. [70] also provides a comprehensive description of the sordid history of past failed experiments aimed at measuring the same AC Stark shifts.

4.2 State-dependent energy shifts

If V_{p} exhibits substantial spatial variation, generally both level shifts and state mixing occur, with the exception of sufficiently non-degenerate Rydberg levels. For the latter, the adiabatic lattice potential is [40]

$$V_{\mathrm{ad}}\left(\mathbf{R}\right)=\int d^{3}rV_{\mathrm{p}}\left(\mathbf{r}+\mathbf{R}\right)\left|\psi\left(\mathbf{r}\right)\right|^{2}. \tag{4.6}$$

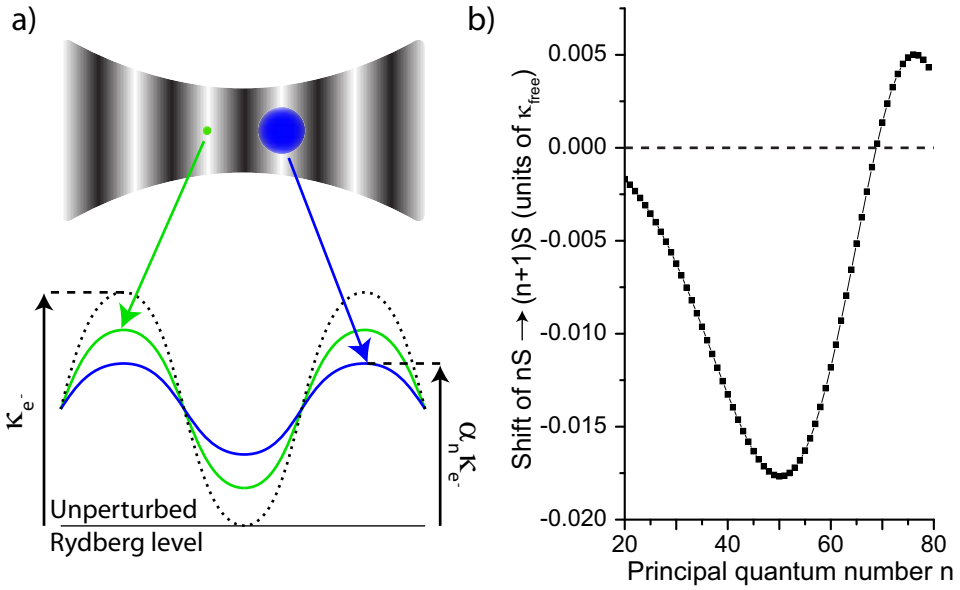

Figure 4.1: Effect of atom size on ponderomotive level shifts of Rydberg atoms in an optical lattice. a) The level shifts are averages over the free electron ponderomotive potential (dotted curve; maximum height κ_{e^-}) weighted by the Rydberg electron's density distribution. Hence, the lattice potentials of large Rydberg atoms tend to be shallower than those of small ones (sold curves; maximum height $\alpha_n\kappa_{e^-}$, with state-dependent reduction factors $0 < \alpha_n < 1$). b) Calculated frequency shift, $(\alpha_{n+1} - \alpha_n)\kappa_{e^-}$, of the Rb nS→$(n+1)$S transition at a lattice maximum as a function of principal quantum number, n.

Here, $\mathbf{R}$ is the center-of-mass coordinate of the atom, $\mathbf{r}$ is the relative coordinate of the Rydberg electron, $V_{\mathrm{p}}\left(\mathbf{r}+\mathbf{R}\right)$ is the position dependent free-electron pondero-

motive potential (Equation 4.1), and $\psi(\mathbf{r})$ is the Rydberg wavefunction. Following Equation 4.6, $V_{\rm ad}(\mathbf{R})$ is a spatial average of $V_{\rm p}$ with weighting function $|\psi(\mathbf{r})|^2$. If the field varies over a length scale comparable to the size of the atom, the result depends on the atomic state. This leads to the state-dependent ponderomotive shifts of the Rydberg levels illustrated in Figure 4.1a.

The state-dependence of the ponderomotive level shifts in an optical lattice can be demonstrated using two-photon microwave spectroscopy between Rb nS states as a sensitive probe. S-states are well suited because of their large quantum defect and resultant rigidity against state-mixing, their isotropic electronic wavefunction, and their low sensitivity to residual electric and magnetic fields, allowing transform-limited microwave spectroscopy. In Figure 4.1b, I show calculated frequency shifts for the two-photon microwave transition nS$\rightarrow$ $(n+1)$S of a Rb Rydberg atom located at an intensity maximum of a one-dimensional ponderomotive optical lattice versus the principal quantum number n. The lattice is formed by two counter-propagating, linearly polarized laser beams of equal electric-field amplitude, E_0, and wavelength (1064 nm). The shifts are scaled by the full lattice-induced shift of the free electron ponderomotive potential, $\kappa_{e^-} = e^2E_0^2/m\omega^2$. For $n < 69$, the shift is negative and has a maximal value of $0.018 \times \kappa_{e^-}$ at n=50. For $n \sim 69$ the frequency shift becomes very small because the size of the wavefunction approximately equals the lattice period, and for $n > 69$ the shift turns positive.

4.3 Apparatus for optical lattice experiments

The experimental apparatus used to perform this experiment is similar to that used in Chapter 3. However, there are a few noteworthy differences. In this experiment, atoms are collected in a MOT while in the presence of a running or standing

wave 1 Watt, 1064 nm laser beam. This is a continuous-wave optical beam and is used to form both a dipole trap (for diagnostic purposes) and an optical lattice.

As before, slow Rydberg atoms are prepared via a two-photon excitation from a laser-cooled cloud of ^{85}Rb atoms in a magneto-optical trap (MOT). Atoms are first collected in a primary, pyramidal MOT, then pushed through a small hole in the pyramid into a vacuum chamber where they are recollected in a secondary MOT. The secondary MOT has a temperature $\sim 200\mu$K and density $\sim 10^{10}$ atoms/cm^3. The lower transition beam (780 nm, FWHM 150 μm) is detuned from the intermediate $5P_{3/2}$ state by 1.2 GHz, instead of only 130 MHz as in Chapter 3. This way, all atoms will see an effectively constant detuning from the 5P level, regardless of their position within the trap. The upper transition beam (480 nm, FWHM 25 μm) is tuned in frequency to achieve resonant 5S $\rightarrow n$S two-photon Rydberg excitation. Both lasers have a linewidth of about 2 MHz. To excite Rydberg atoms, the MOT laser beams are turned off and the optical excitation beams are pulsed on for 2 μs. The 1064 nm lattice laser beam (focal diameter 13 μm at FWHM) is always on and produces an optical lattice for atoms in the 5S ground state as well as a ponderomotive optical lattice (see Section 4.1) for atoms in Rydberg states.

For this particular experiment, after excitation the Rydberg atoms are exposed to several μs of microwave radiation, which will be discussed in detail below. Subsequently, an electric-field ramp is applied to the atoms for state-selective field ionization. The freed electrons are counted using a micro-channel plate detector.

The spatial arrangement of the laser beams and atom cloud is sketched in Figure 4.2a. The 1064 nm lattice beam and the 780 nm lower transition beam are launched from the same optical fiber and are focused through the excitation region with a 30 cm lens. The focus of the 1064 nm beam is centered on the excitation region,

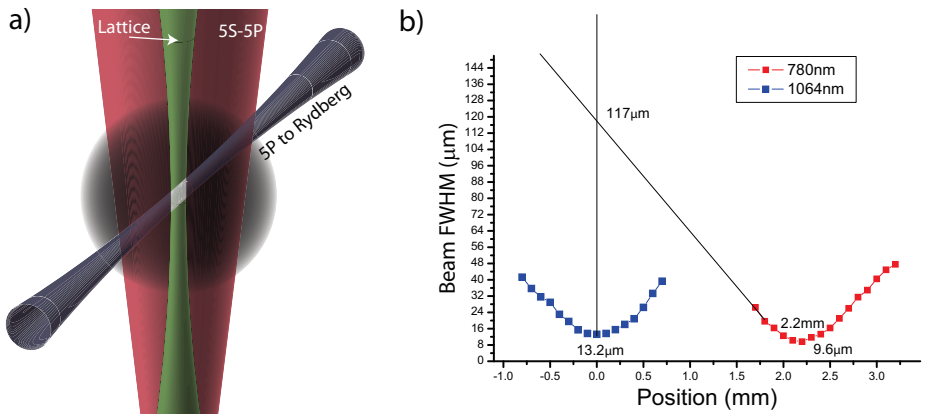

Figure 4.2: a) Diagram of laser beams used for Rydberg excitation and for creating the optical lattice. b) Offset foci of the 780 nm and 1064 nm beams.

overlapping about 1% of the MOT. The out-going 1064 nm beam is re-collimated by another 30 cm lens and then retroreflected back through the chamber, where it re-focuses onto itself to form an optical lattice. Chromatic aberrations in the lens system cause the 780 nm lower transition beam to focus about 2 mm away. Figure 4.2b shows a measurement of the 1064 nm and 780 nm beam sizes as a function of position. The 780 nm beam has a FWHM of about 10 μm at its focus and a FWHM of about 120 μm at the focus of the 1064 nm beam.

To align the lattice, the retroreflected beam is first blocked, resulting in a simple, running-wave dipole trap for the ground state atoms in the MOT. Atoms in the dipole trap are quite efficiently cooled by the MOT laser beams, which are relatively far detuned from the cooling transition due to the dipole-trap-induced light shifts [73]. A Rydberg excitation spectrum from the dipole trap is shown in Figure 4.3 (black diamonds). The large peak on the left side of the spectrum results from atoms excited in the wings of the 780 nm beam outside of the dipole trap. The peak on the right corresponds to atoms within the dipole trap beam, where the transition frequency is blue-shifted due to the trap-induced light shifts. The blue-shifted peak exhibits a sharp high-frequency cutoff because most atoms in the dipole trap are

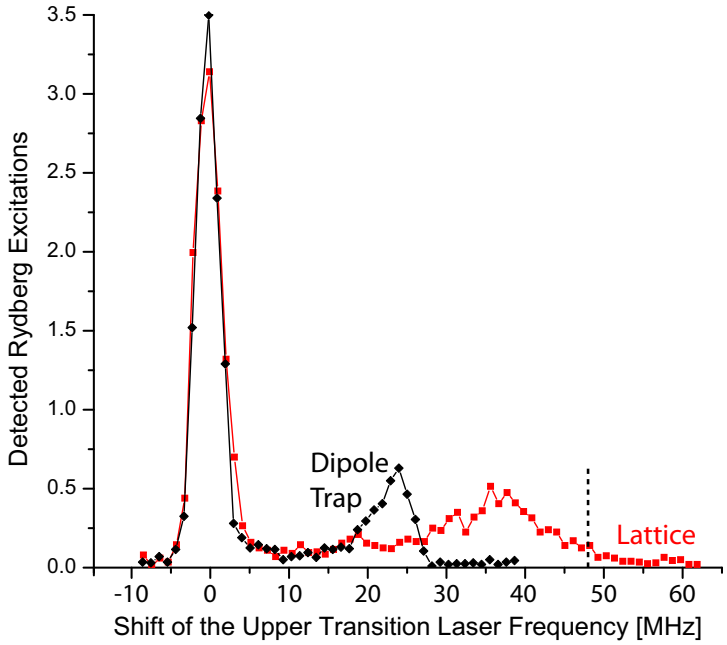

Figure 4.3: Laser excitation spectra of the 50S Rydberg level for the dipole trap and optical lattice, obtained by scanning the upper transition laser. The dashed vertical line represents the approximate maximum lattice-induced shift. Clearly, this estimate of the maximum shift is accurate only to within a few MHz, as it is difficult to tell exactly when the signal drops to zero.

located relatively close to the bottom of the trap. I optimize the dipole trap focus for maximum light shift and sharp high-frequency cutoff.

The optical lattice is formed by unblocking the retroreflected 1064 nm beam and aligning it back through the optical fiber. A typical lattice spectrum is shown in Figure 4.3 (red squares). As would be expected, the optimal position of the 30 cm retroreflection lens is close to the point where the retroreflected beam power is maximized back through the optical fiber. However, abberations of the system shift the focus slightly. Figure 4.4 shows lattice spectra as a function of the position of the 30 cm retroreflection lens. The bright red vertical line on the left side of the graph corresponds to atoms outside of the trap (left peak in Figure 4.3). There are two positions that provide a maximal shift to the atoms: 13.2 mm and 11.6 mm. These are marked by black arrows in Figure 4.4. The maximum at 13.2 mm is the result of

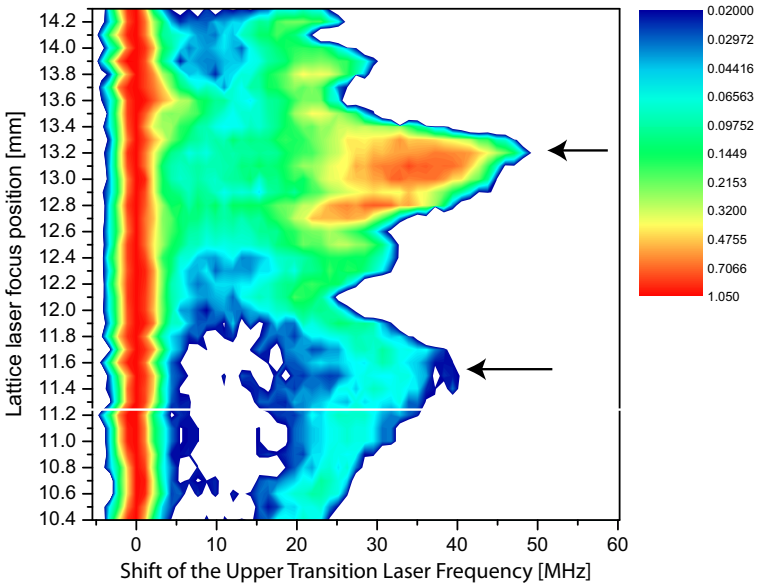

Figure 4.4: Lattice spectra as a function of the retroreflection lens position. Count rate is plotted on a log scale to show extra detail in low-count regions. The black arrows point to regions where the atoms experience a local maximum in the light shift (see text).

the 780 nm excitation beam being focused onto the excitation region instead of the 1064 nm lattice beam. This is evident by the fact that the peak for atoms outside of the trap is broadened quite significantly (note the difference in the signal in the 5 - 20 MHz region). The maximum at 11.6 mm is the desirable position for the retroreflection lens. The horizontal white line located just above 11.2 mm marks the point where the lattice light is best coupled back through the fiber. The optimal position of the lens is about 350 μm farther away from the trap. This factor was found to be consistent from day to day, and allowed a rather simple positioning procedure for the retroreflection lens once the optimal coupling position was measured.

Unlike the dipole trap spectrum, lattice spectra do not exhibit a sharp cutoff. Because the force from the optical potential is conservative, some cooling of the atoms must occur as they enter the potential formed by the 1064 nm beam(s), or the atoms will simply roll back up the optical potential and out of the trap. This cooling is provided by the MOT laser beams, which are increasingly red-detuned as

the atoms move deeper into the potential. The broad cutoff of the lattice spectra may be due to a loss in cooling efficiency in potentials deeper than about 45-50 MHz. To investigate this further, I measured dipole trap and lattice spectra as a function of 1064 nm laser power. Figure 4.5 shows the resultant spectra. The optical dipole trap (left graph of Figure 4.5) exhibits a linear shift as a function of 1064 nm laser power for essentially the entire range of the 0→1.5 W scan in power. The lattice (right graph), exhibits spectra similar to those in the dipole trap for very low laser powers. However, for increasing powers the spectra are broadened because the MOT light is too far detuned to efficiently cool the atoms. The lattice loses its ability to collect atoms very quickly when a laser power above 1 W is applied, corresponding to a shift of about 45 MHz. At this point, not only are the atoms not cooled into the bottom of the trap wells, they are unlikely to remain in the trap at all.

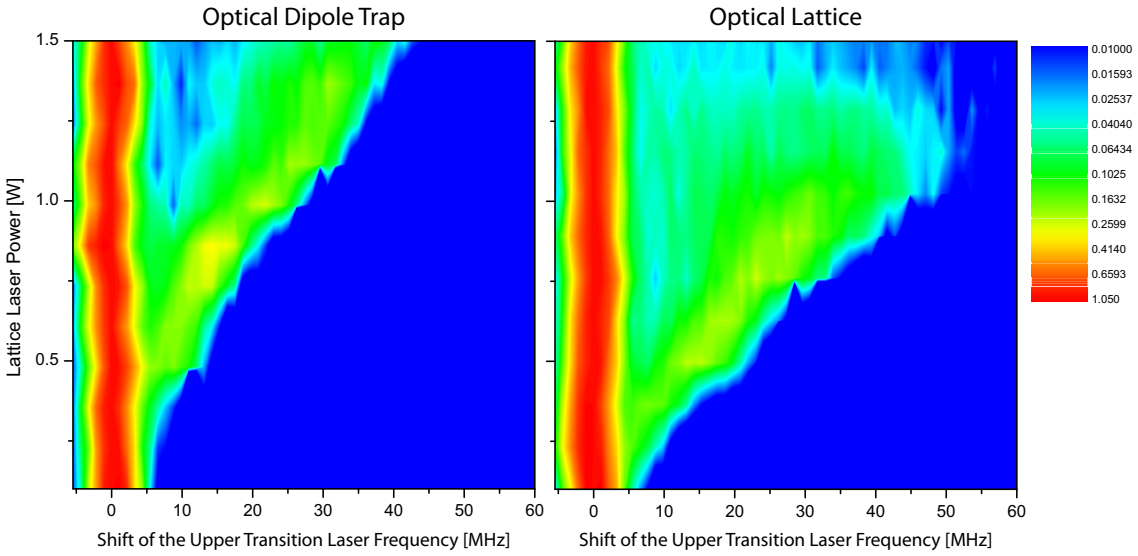

Figure 4.5: Dipole trap and lattice spectra as a function of 1064 nm laser power. Count rate is plotted on a log scale to show extra detail in low-count regions.

4.4 Rydberg atom averaging in the ponderomotive optical lattice

For perfect, loss-free retroreflection, the intensity at the lattice maxima would be 4 times that of the dipole trap, but the observed shift seen in Figure 4.3 is only about twice as much. Experimental factors that reduce the lattice-induced shift are imperfect alignment and power loss of the return beam as it passes through the lens system. The observed trap-induced shift is further reduced by the spatial averaging in Equation 4.6. Figure 4.6 illustrates both of these factors.

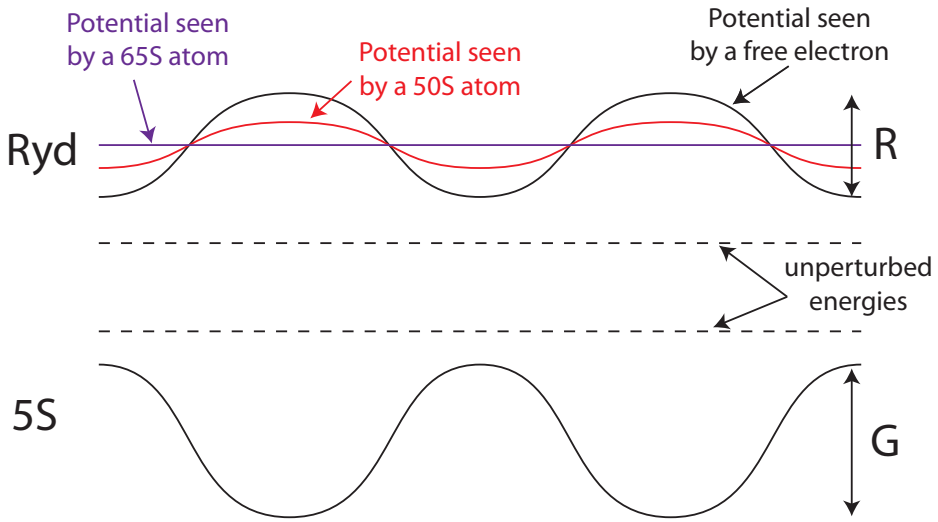

Figure 4.6: The total shift measured in the lattice spectrum is a combination of the ground state light shift and the averaged ponderomotive shift seen by the Rydberg electron. The total shift can depend strongly on the attenuation of the return beam used to create the optical lattice, because this adds a running wave component to the field and results in an offset energy shift for both the ground and excited states. This shift does not depend on the Rydberg state.

The measured shift in the optical lattice is due to a light shift of both the ground state and the Rydberg state. The ground state can be considered point-like in relation to the optical lattice, while the Rydberg state averages over many parts of the potential, depending on its size. This is shown in Figure 4.6, where the ground state shift is labeled as G, and the shift that would be seen by a (stationary) free electron is labeled as R. As shown in Figure 4.1, the Rydberg state energy shift is

reduced by a factor α_n from the free electron shift because of averaging. The value of α_n is found via Equation 4.6.

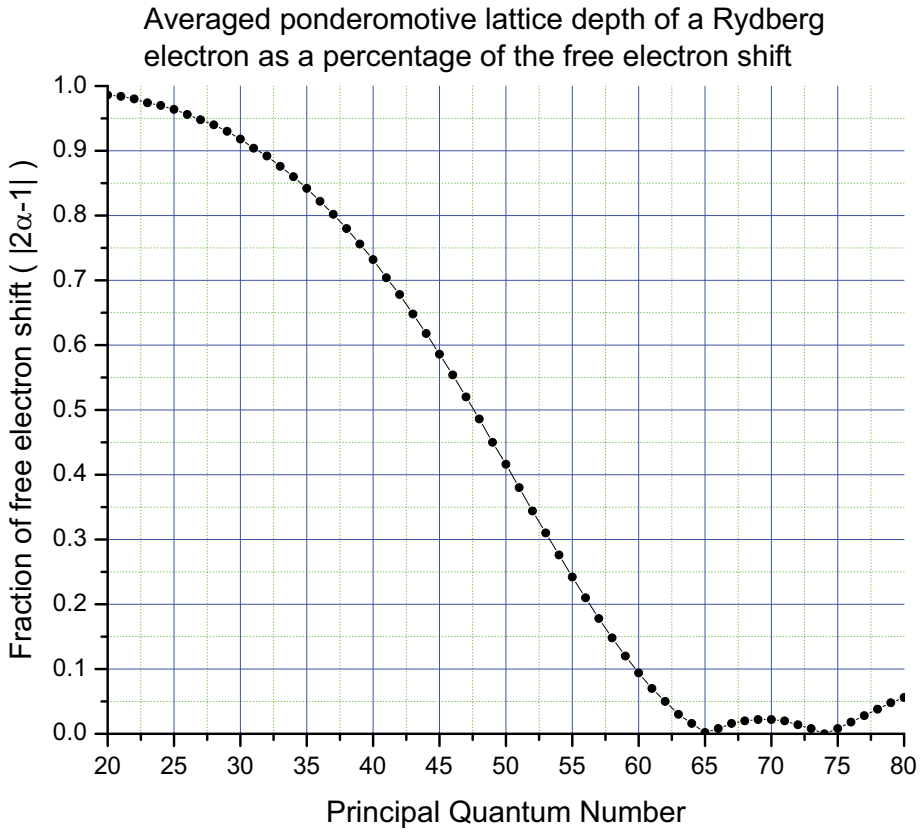

Figure 4.7: Rydberg electron trap depth as a fraction of the free electron trap depth versus the principal quantum number for $nS_{1/2}$ states of Rb.

It is important to keep in mind that just as the maximum shift is decreased by α_n, the minimum is *increased* by a factor 1-α_n. This is a consequence of the way I have defined the parameter α_n. The depth of the trap seen by the atom in comparison to that which is seen by a free electron is therefore decreased by a factor of $2\alpha_n$-1. The magnitude of this factor is shown in Figure 4.7 as a function of principal quantum number n. From this graph, it is seen that for n=65 and 74, the depth of the trap is nearly zero. Between these points, the trap modulation experienced by the Rydberg atom is actually inverted from that which is seen by a free electron.

When calculating the ground and Rydberg state contributions to the measured shift in the optical lattice, one must include the effects of return beam attenuation and imperfect alignment of the foci of the two beams. This will create a situation where there is a running wave component to the shift. The Rydberg potential will have a positive offset and the ground state potential will have a negative offset (as shown in Figure 4.6).

To account for the running wave component of the lattice, I introduce the constant η to denote the fractional power remaining in the return beam. The incident electric field is then E_0, and the return beam electric field is ηE_0. The maximum electric field in the lattice is then $E_0\,(1+\eta)$ while the minimum electric field is $E_0\,(1-\eta)$. The maximum shift of the 5S ground state is then

$$G = \frac{1}{4}\kappa_{5\mathrm{S}}\,(1+\eta)^2 \tag{4.7}$$

where $\kappa_{5\mathrm{S}} = \alpha_{5\mathrm{S}} E_0^2$ and $\alpha_{5\mathrm{S}}$ is the dynamic polarizability of the $5\mathrm{S}_{1/2}$ ground state.

The shift of the Rydberg state is slightly more complicated because for all Rydberg states the running wave component will create the same shift, while the Rydberg averaging factor α_n will be Rydberg-state dependent. The averaged lattice depth (peak to peak distance in Figure 4.1) for a free electron is given by

$$\begin{aligned} R_{\mathrm{e^-,depth}} =& \frac{1}{4}\frac{\kappa_{e^-}}{E_0^2}\left(E_{\max}^2 - E_{\min}^2\right) \\ =& \frac{1}{4}\kappa_{e^-}\left[(1+\eta)^2 - (1-\eta)^2\right] \\ =& \frac{1}{4}\kappa_{e^-} \times 4\eta. \end{aligned} \tag{4.8}$$

where $\kappa_{e^-} = e^2 E_0^2/m\omega^2$ as defined earlier. The average lattice depth for a Rydberg electron is thus $R_{n,\mathrm{depth}} = (2\alpha_n - 1)\,R_{\mathrm{e^-,depth}}$. Again, the reason I add a factor of

$(2\alpha_n - 1)$ here is because α_n only accounts for the reduction of the lattice maxima. Here, I am comparing the averaged lattice depths, and so not only are the maxima reduced but the minima are raised, decreasing the depth further.

The average shift[3] of the Rydberg state does not depend on α_n and is the same for both a free electron and a Rydberg electron. It is given by

$$\begin{aligned} R_{\text{avg}} =& \frac{1}{4}\frac{\kappa_{e^-}}{E_0^2}\frac{(E_{\text{max}}^2 + E_{\text{min}}^2)}{2} \\ =& \frac{1}{4}\kappa_{e^-}\left[\frac{(1+\eta)^2 + (1-\eta)^2}{2}\right] \\ =& \frac{1}{4}\kappa_{e^-}\left(1+\eta^2\right) \end{aligned} \tag{4.9}$$

Thus, the total maximum shift of the Rydberg state is

$$\begin{aligned} \frac{1}{2}R_{n,\text{depth}} + R_{\text{avg}} =& \frac{1}{4}\left(2\alpha_n - 1\right)\kappa_{e^-} \times 2\eta + \frac{1}{4}\kappa_{e^-}\left(1+\eta^2\right) \\ =& \frac{1}{4}\kappa_{e^-}\left[1 + \eta^2 + 2\eta\left(2\alpha_n - 1\right)\right] \end{aligned} \tag{4.10}$$

The total lattice induced energy shift (LIES) seen spectroscopically is then the sum of Equations 4.7 and 4.10, or

$$\begin{aligned} \text{LIES} =& \frac{1}{4}\{\kappa_{5\text{S}}\left(1+\eta\right)^2 + \kappa_{e^-}\left[1 + \eta^2 + 2\eta\left(2\alpha_n - 1\right)\right]\} \\ =& \frac{1}{4}\kappa_{5\text{S}}\left(1+\eta\right)^2 + \frac{1}{4}\kappa_{e^-}\left[1 + \eta^2 + 2\eta\left(2\alpha_n - 1\right)\right]. \end{aligned} \tag{4.11}$$

A quick check reveals that when $\eta = 1$, I arrive at the simple result:

$$\text{LIES} = \kappa_{5\text{S}} + \kappa_{\text{e}^-} \times \alpha_{\text{n}}, \tag{4.12}$$

as expected.

The total lattice shift measured in Figure 4.3 is approximately 48 MHz (Rydberg state 50S). To find the ground and Rydberg state contributions to the 48 MHz shift,

[3]By average shift I mean halfway between the maximum and minimum shifts, i.e. the flat potential in Figure 4.6.

Shift Parameter		
	A	$\frac{1}{4}\kappa_{5S} = \frac{\text{LIES}}{(1+\eta)^2+\frac{\kappa_{e^-}}{\kappa_{5S}}[1+\eta^2+2\eta(2\alpha_n-1)]}$
Maximum ground state shift	G_{max}	$A \times (1+\eta)^2$
Maximum Rydberg state shift	R_{max}	LIES - G_{max}
Maximum free electron shift	R_{e^-}	R_{max}/α_n
Free electron depth	$R_{e^-,depth}$	$A \times \frac{\kappa_{e^-}}{\kappa_{5S}} \times 4\eta$
Average Rydberg/electron shift	R_{avg}	$A \times \left(1+\eta^2\right) \times \frac{\kappa_{e^-}}{\kappa_{5S}}$
Rydberg electron depth	R_{depth}	$(2\alpha_n - 1) \times R_{e^-,depth}$

Table 4.1: A number of parameters related to the lattice induced shift.

I begin with

$$48 \text{ MHz} = \frac{1}{4}\{\kappa_{5S}\left(1+\eta\right)^2 + \kappa_{e^-}\left[1+\eta^2+2\eta\left(2\alpha_n-1\right)\right]\} \tag{4.13}$$

The ratio $\kappa_{e^-}/\kappa_{5S} = 1.354/1.776$ (see Appendix B.3). The values of α_n for the various Rydberg states are shown in Figure 4.7, and $\alpha_{50} = 0.708$. This is enough information to solve for the component shifts for a given value of η.

Table 4.1 shows the relevant parameters that can be calculated using the formulae above. For $n = 50$, a lattice induced shift of 48 MHz, and $\eta = 0.7$, the ground and Rydberg state contributions are 31 and 17 MHz, respectively. In this case, the depth of the trap for a Rydberg electron is 10 MHz. The corresponding ponderomotive shift of a free electron would be 24 MHz. Figure 4.8 shows how the calculated trap depth depends on the assumed value of η. The dependency is not very strong until η falls below about 0.5, but does limit the ability to precisely determine that potential depth of the Rydberg atom trap.

4.5 Microwave spectroscopy of Rydberg atoms

In principle, it would be possible to use lattice spectra and Equation 4.11 to demonstrate the n-dependence of α_n predicted by Equation 4.6. However, as alluded to above, this method would not be precise due to the laser linewidths, as well as uncertainties in η, the measured lattice-induced shift, and the lattice intensity. In-

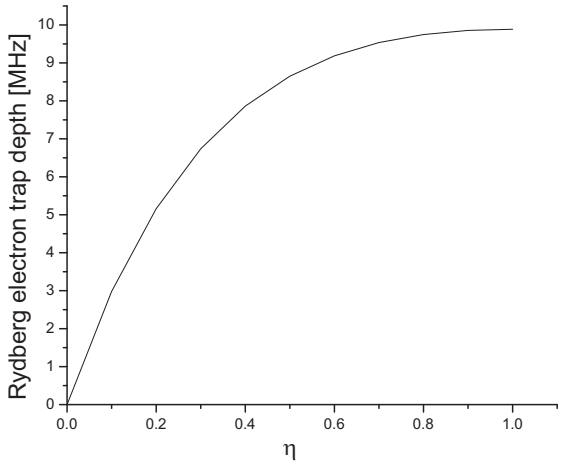

Figure 4.8: Dependency of the Rydberg trap depth on η.

stead, I use microwave spectroscopy as a sensitive and reliable method. A WR-28 or WR-42 waveguide is used to direct continuous microwave radiation into the vacuum chamber. I introduce 6 μs between Rydberg excitation and subsequent detection to allow the Rydberg atoms time to interact with the microwaves. The microwave intensity is set low enough that power broadening is minimal. The interaction duration is sufficiently short to keep the effect of Rydberg atom motion transverse to the lattice axis small while still resulting in narrow microwave spectra. Also, by exciting fewer than one atom per shot, we ensure that atom-atom interactions (such as those that lead to an excitation blockade) do not play a role. The optically excited and microwave-coupled Rydberg states produce distinct SSFI signals that are recorded separately with a gated pulse counter.

Figure 4.9 shows the results of driving a two-photon transition from 50S to 51S. The top curve is the microwave spectrum without a lattice. The frequency axis is chosen such that the unperturbed 50S$\rightarrow$51S transition frequency of approximately 61.92 GHz is located at zero. This curve has a FWHM of 110 kHz, which is close to the calculated Fourier transform limit of about 120 kHz (see Appendix D), and exhibits small Fourier side peaks, indicating coherent excitation. The other three

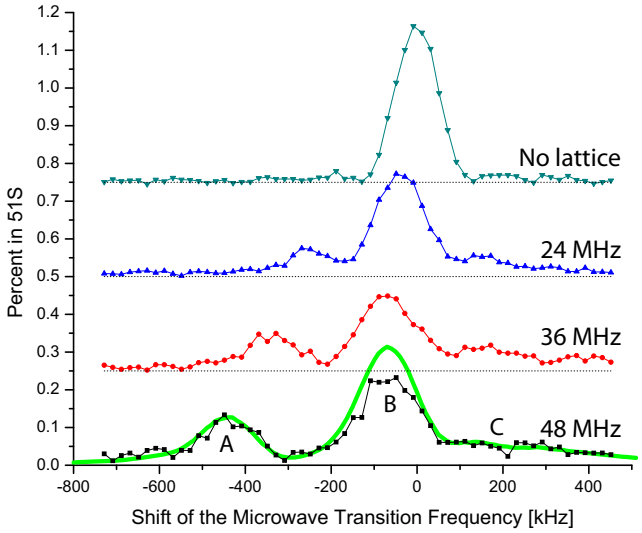

Figure 4.9: Microwave spectra of the 50S→51S transition outside of the lattice and for three different lattice-induced shifts. The thick green line shows the results of a numerical simulation (see text). (For clarity, spectra are staggered vertically.)

curves show microwave spectra with the lattice turned on for three different lattice-induced shifts. For these cases, the upper transition 480 nm laser is set to excite atoms at the deepest part of the lattice (far right side of lattice spectrum in Figure 4.3, marked by dashed line). Thus, Rydberg atoms are located near the ponderomotive-lattice peaks at the beginning of the microwave interaction. The three lower spectra in Figure 4.9 show distinct features referred to as A, B, and C: a strongly red-shifted peak that shifts approximately linearly with the lattice intensity (A), a central peak that red-shifts slightly with the lattice intensity (B), and a blue-shifted signal (C). For the lowest spectra, the shift of peak A is about -430 kHz. This coincides with the value expected from Figure 4.1b, assuming a ponderomotive-lattice depth consistent with Figure 4.3 and Equation 4.11.

To interpret the features in the microwave spectra, numerical simulations of the Rydberg-atom evolution were conducted. The simulation software was written by Professor Raithel, while I performed the simulations and analyzed the results. The simulation assumes a Boltzmann distribution of ground-state atom positions and

velocities in the 5S-lattice potential. Based on the optical excitation spectra shown in Figure 4.3, atomic temperatures are estimated to be 200 μK. After randomly selecting positions and momenta following this Boltzmann distribution, the probabilities that the atoms are excited into the 50S level are determined. It is assumed that the net optical excitation bandwidth is 5 MHz and that the optical Rydberg excitation is resonant at the lattice-field maxima. For each 50S Rydberg atom produced, its classical center-of-mass trajectory, $\mathbf{R}(t)$, in the adiabatic ponderomotive lattice potential $V_{\mathrm{ad,50S}}(\mathbf{R})$ (see Equation 4.6), is computed using a fourth order Runge-Kutta method. The lattice field strength and η, which determine the peak height and the modulation depth of $V_{\mathrm{ad,50S}}(\mathbf{R})$, are chosen consistent with Equation 4.11 and Figure 4.3. Then, the microwave-driven evolution operator in the internal space $\{|50S\rangle, |51S\rangle\}$, $\hat{U} = \exp(-\mathrm{i}\hat{H}t/\hbar)$ with $H = \hbar\chi(|50S\rangle\langle 51S| + |51S\rangle\langle 50S|)$ $+ (V_{\mathrm{ad,50S}}(\mathbf{R}(t)) + \hbar\delta)|50S\rangle\langle 50S| + V_{\mathrm{ad,51S}}(\mathbf{R}(t))|51S\rangle\langle 51S|$, is computed based on the simulated trajectory $\mathbf{R}(t)$ and the adiabatic potentials $V_{\mathrm{ad,50S}}(\mathbf{R})$ and $V_{\mathrm{ad,51S}}(\mathbf{R})$. The two-photon microwave Rabi frequency, χ, is constant during the atom-field interaction and is chosen such that the on-resonant final $51S$-population without lattice matches that observed in the experiment (top curve in Figure 4.9). As in the experiment, the atom-field interaction time is randomly selected between 6 μs and 8 μs. The simulated spectra vs the detuning of the microwave frequency from the field-free transition frequency are shown as bold lines in Figures 4.9 and 4.10.

It is noted that for the simulation of $\mathbf{R}(t)$, the potential $V_{\mathrm{ad,50S}}$ is used, while the quantum state actually is a coherent mix of 50S and 51S. This approximation is allowable, because the maximum relative discrepancy between $V_{\mathrm{ad,50S}}$ and $V_{\mathrm{ad,51S}}$ is only 1.8% (see Figure 4.1), and because over the course of the given atom-field interaction time the atoms only perform a few center-of-mass oscillations or run

only over a few lattice wells. Also, the results are found to be quite insensitive to the assumed atom temperature. The three main lattice-induced features in the microwave spectra shown in Figure 4.9 are reproduced very well by the simulation. In both simulations and experiment, peak A is centered at -430 kHz and has a width of about 150 kHz. By visual inspection of simulated Rydberg-atom trajectories $\mathbf{R}(t)$ contributing to peak A (see Chapter 5), I find that peak A is due to atoms that are excited at a lattice maximum and remain close to that maximum over the duration of the atom-field interaction. I further observe that Peak B in Figure 4.9 corresponds to atoms that are excited at lattice maxima and have enough kinetic energy to roam over many lattice wells. Lastly, the C-signal corresponds, in part, to atoms that are trapped by the lattice potential and oscillate back and forth within a single well. There is enough time for about three oscillations during the course of the atom-field interaction. Atoms with other trajectories add to the C-signal as well, such as ones that mostly move transverse to the lattice axis near a plane with vanishing intensity. I do not consider these atoms trapped, as the present lattice does not provide a transverse trapping force. The overall ratio of trapped and untrapped atoms prepared by the optical excitation depends on experimental details, such as the lattice potential and the optical excitation frequency. The presence of a mix of trapped and untrapped atoms is reasonable, considering that in our experiment the modulation depth of the ponderomotive optical lattice is about 10 MHz, the kinetic energy of the laser-cooled atoms is about 2 MHz, and the Rydberg atoms are excited near the ponderomotive-lattice peaks. It is expected that, as the lattice intensity is reduced, the positions of all features A, B, and C in the microwave spectra should scale proportional to the lattice intensity. This is indeed observed experimentally (see Figure 4.9) and is reproduced in simulations. Specifically, for the strongly red-shifted feature A, we

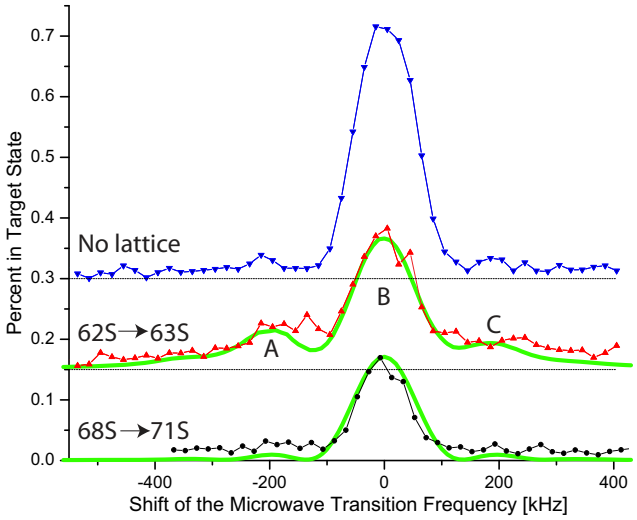

Figure 4.10: Microwave spectra of the 62S→63S and 68S→71S transitions. (For clarity, spectra are staggered vertically.)

observe microwave shifts of −340 kHz and −240 kHz for optical lattice-induced shifts of 36 and 24 MHz, respectively. In close agreement, the corresponding microwave shifts expected from Figure 4.1b are −320 kHz and −220 kHz. Figure 4.10 shows the microwave spectra for the transitions 62S→63S (middle) and 68S→71S (bottom) in a lattice with the same intensity as the bottom spectrum in Figure 4.9. The 62S→63S spectrum exhibits side-structures A and C that span about half the range of corresponding structures seen in the lowest curve of Figure 4.9, with peak A located at about -180 kHz. This observation agrees with predictions based on Figure 4.1b and is reproduced by simulations (bold lines in Figure 4.10). For Rydberg states near n=69, Figure 4.1b indicates that the microwave shift in the optical lattice should be negligible. Accordingly, the microwave spectrum of the transition 68S→71S, shown at the bottom of Figure 4.10, shows no side peak structure (in this measurement, I have chosen Δn=3 for technical reasons).

4.6 Conclusion

These results show that the energy shifts of Rydberg atoms in ponderomotive lattices depend on the specific Rydberg level, in close agreement with theory. The simulations here also provide additional insight into the Rydberg atom trajectories that will be discussed in much more detail in the following chapter. In particular, the results suggest that both trapped and untrapped Rydberg atoms are excited in the ponderomotive lattice, although most atoms remain untrapped. In the next chapter, I discuss ways to increase Rydberg-atom trapping efficiency using an excitation scheme that prepares the Rydberg atoms near ponderomotive-lattice minima.

CHAPTER V

Trajectories of Rydberg atoms in a Ponderomotive Optical Lattice

5.1 Introduction

In Chapter 4, I introduced a microwave spectroscopy technique useful for studying Rydberg atoms in ponderomotive optical lattices. Here, I provide a detailed analysis of the microwave spectra shown in Chapter 4, and analyze strategies that will lead to improved trapping and analysis. Using software written by Professor Georg Raithel, I simulate the trajectories of Rydberg atoms subject to the optical lattice potential and identify three different classes of trajectories (labeled as A, B, and C in the previous chapter). I begin with an analogy to the problem of the simple plane pendulum that helps in the understanding of the allowed trajectories.

5.2 Classical Phase Space Dynamics of Rydberg atoms in a 1D Ponderomotive Lattice

Due to the vast difference between typical Rydberg-atom Kepler frequencies ($\sim 10^{11}$Hz) and optical frequencies ($\gtrsim 10^{14}$Hz), the dominant effect of a non-resonant laser field applied to a Rydberg atom is that the field adds a ponderomotive term, $e^2E^2/4m_e\omega^2$, to the usual atomic potential in the Rydberg electron's Hamiltonian. Here, $-e$ is the electron charge and m_e its mass, $\omega = kc$ is the angular frequency of

the field, k the wavenumber, and E the electric-field amplitude. If the field consists of two counter-propagating laser beams, the spatial period of the intensity modulation in the resultant standing wave is π/k. If the period is much larger than the atom, the ponderomotive term does not vary substantially over the atom's volume. For laser beams with equal linear polarization and field amplitude E_0, the trapping potential acting on the Rydberg atom's center-of-mass coordinate then approximately equals the free-electron ponderomotive potential in the lattice,

$$U(Z) = \frac{V_0}{2}\left(1 - \cos\left(2kZ\right)\right) \tag{5.1}$$

where Z is the atom's center-of-mass coordinate in the lattice-beam direction and V_0 is the maximum potential depth, $V_0 = e^2E_0^2/m_e\omega^2$. The equation of motion for the atom is

$$\ddot{Z} = -\frac{V_0 k}{m}\sin\left(2kZ\right). \tag{5.2}$$

In comparison, the equation of motion for a plane pendulum is

$$\ddot{\theta} = -\frac{g}{L}\sin\theta. \tag{5.3}$$

From Equations 5.2 and 5.3 it is obvious that there is a direct analogy between the angular motion of the plane pendulum and the motion of an atom parallel to the axis of the lattice. The small-amplitude oscillation frequencies are $\sqrt{2V_0k^2/m}$ and $\sqrt{g/L}$ for the lattice and the pendulum, respectively. As the energy of the atom increases toward a critical energy equal to the depth of the lattice potential, the oscillation amplitude increases and the oscillation frequency decreases. Looking at the phase diagram for this problem assists in understanding the motion of the atoms in the lattice. Consider an atom with a total energy E_0 in the lattice potential given by Equation 5.1. The equation of motion can be written as

$$\dot{Z} = \sqrt{\frac{V_0}{m}\left(\cos\left(2kZ\right) - 1\right) + \frac{2E_0}{m}}. \tag{5.4}$$

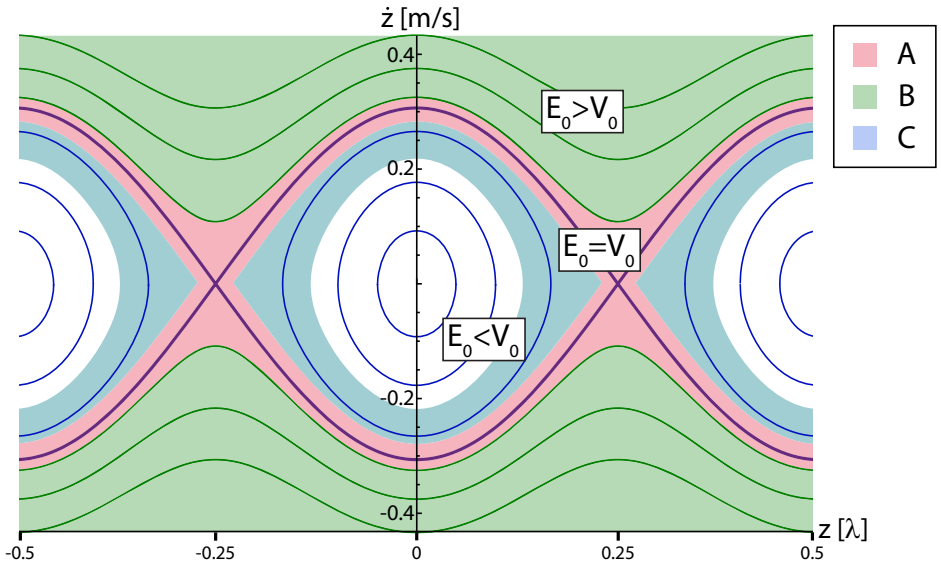

Figure 5.1: Phase-space diagram for motion of atoms in a ponderomotive optical lattice. The different shaded regions correspond to the trajectory classes A, B, and C seen in Figure 5.2.

Figure 5.1 shows a plot of the phase-space diagram for ^{85}Rb atoms in a lattice with $V_0 = 10$ MHz and lattice laser wavelength $\lambda = 1064$ nm. The phase-space diagram has a separatrix at an energy that equals the lattice depth ($E_0 = V_0$; bold line in Figure 5.1). For $E_0 < V_0$, the phase-space trajectories are periodic and resemble closed ellipses, corresponding to atoms that are trapped inside one lattice well. For $E_0 > V_0$, the phase trajectories are periodic but not closed, corresponding to un-trapped atoms running over the lattice wells. The separatrix forms a boundary between the two cases; it has hyperbolic fixed points at the lattice potential maxima, $\{(z = (n + 1/2)\lambda/2, \dot{z} = 0), n \in \mathbb{Z}\}$. Trajectories close to the separatrix have a long period, and atoms on such trajectories spend most of their time in the vicinity of the hyperbolic fixed points.

In the experiment described in Chapter 4 (also Reference [74]), the depth of the Rydberg trapping potential, V_0, was derived from line shifts measured via laser spectroscopy of optical Rydberg excitation lines in the lattice. The lattice depth experienced by a Rydberg atom was typically 10 MHz, corresponding to a small-

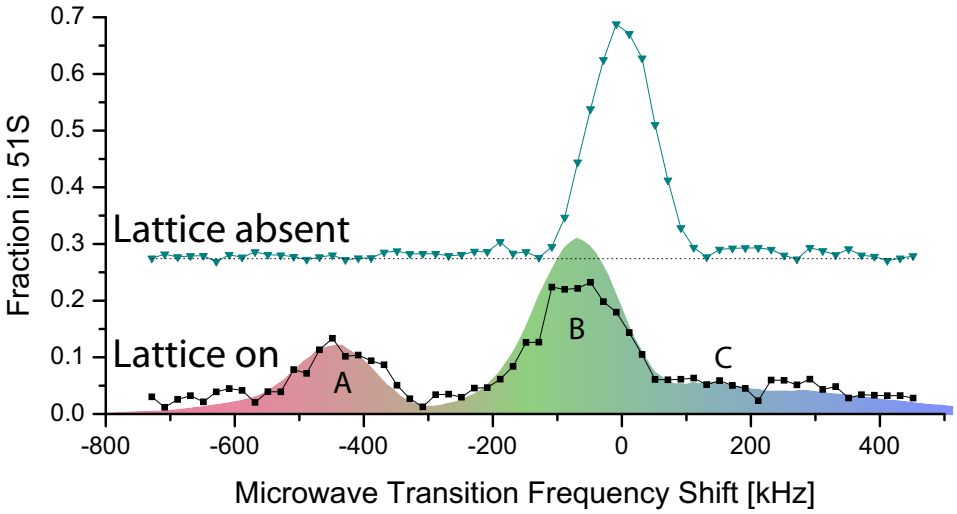

Figure 5.2: Experimental microwave spectra (dots and thin lines) of the 50S→51S transition outside of the lattice and for a Rydberg lattice modulation depth of $V_0 = 10$ MHz. The shaded curve shows the result of a simulation. The coloring of the shaded curve corresponds to the coloring of the different regions of Figure 5.1.

amplitude oscillation period of 3.5 μs. Atoms were excited into Rydberg states near the lattice maxima, with thermal kinetic energies of about 2 MHz. Since the lattice depth was much larger than the thermal kinetic energy, the relevant phase-space trajectories were concentrated near the separatrix. Hence, both trapped and untrapped classes of trajectories were excited in Chapter 4. The different classes of trajectories correspond to well-defined features in the measured microwave spectra, as will be discussed in the following section.

5.3 Microwave spectra of Rydberg transitions in an optical lattice

In the analysis presented in the previous section, it was assumed that the Rydberg atom is much smaller than the lattice period, resulting in a potential depth $V_0 = e^2E_0^2/m_e\omega^2$. This approximation becomes inaccurate for principal quantum numbers large enough that the Rydberg wavefunction extends over a significant portion of a lattice well. In that case, the adiabatic lattice potential of the Rydberg atom follows from [75],

$$V_{\mathrm{ad}}(\mathbf{R}) = \int d^3 r V_{\mathrm{p}}(\mathbf{r}+\mathbf{R}) \left|\psi(\mathbf{r})\right|^2. \tag{5.5}$$

where $\mathbf{R}$ is the center of mass coordinate of the atom, $\mathbf{r}$ is the relative coordinate of the Rydberg electron, $V_{\mathrm{p}}(\mathbf{r}+\mathbf{R})$ is the position dependent free-electron ponderomotive potential, $\frac{e^2|\mathbf{E}(\mathbf{r}+\mathbf{R})|^2}{4m_e\omega^2}$, and $\psi(\mathbf{r})$ is the Rydberg wavefunction. As a result, the adiabatic trapping potentials depend on the atomic state. Typically, with increasing principal quantum number, n, the adiabatic Rydberg-atom trapping potentials, $V_{\mathrm{ad}}(\mathbf{R})$, become shallower than the underlying free-electron potential, $V_{\mathrm{p}}(\mathbf{R})$, and may even become inverted for certain aspect ratios of atom size and lattice period. From Equation 5.5 it is obvious that the angular quantum numbers also affect the detailed shape of $V_{\mathrm{ad}}(\mathbf{R})$. The adiabatic potentials are in general complicated and are accompanied by substantial lattice-induced state mixing [75]. However, the potentials for nS Rydberg atoms are fairly simple due to the non-degeneracy of these states (hence, no state mixing) and the isotropy of their wave-functions. In the 1D-lattice considered here, the adiabatic potentials of nS Rydberg states are still of the general form of Equation 5.1; the state dependence primarily affects the potential depth. While the state-dependence of V_{ad} will, in most cases, not affect the functionality of the lattice as a trapping device for Rydberg atoms, it leads to frequency shifts of transitions between different Rydberg states. In Chapter 4, this lattice-induced frequency shift and its state dependence have been used to verify the effectiveness of the ponderomotive optical lattice.

Figure 5.2 shows a microwave spectrum from Chapter 4 of the 50S→51S transition for atoms within a Rydberg lattice having a modulation depth of 10 MHz. In that experiment, atoms were excited into the 50S Rydberg state near a lattice potential maximum. Atoms that have very little initial kinetic energy spend a majority of their

time near a hyperbolic fixed point in Figure 5.1. In the plane pendulum analogy, this case corresponds to an inverted pendulum near an unstable equilibrium. Calculating the shift of the 50S $\rightarrow$ 51S microwave transition using Equation 5.5 for an atom resting at a hyperbolic fixed point, I obtain line shifts of ~ -430 MHz. I therefore expect that the pink region in Figure 5.1 should correspond to peak A in Figure 5.2. Atoms that have enough energy to sample many lattice wells during the given atom-field interaction time will see a reduced shift of the transition energy because of averaging, and are therefore expected to contribute to peak B in Figure 5.2 (light green phase-space area in Figure 5.1). Finally, atoms that are trapped oscillate in a single lattice well and are expected to have upshifted microwave transition frequencies. These atoms contribute to region C in the microwave spectrum (light blue phase-space area in Figure 5.1).

5.4 Trajectory Simulations

Via software written by Georg Raithel, I have performed numerical simulations of the Rydberg atom trajectories to gain additional insight into the behavior of Rydberg atoms in an optical lattice. This is a simplified version of the software described in the previous chapter, where the full microwave spectrum for each case was calculated. Again, a Boltzmann distribution of ground-state atom positions and velocities in the ground, 5S-lattice potential is assumed. I use a temperature estimate of 200 μK consistent with the data shown in Chapter 4. After randomly selecting positions and momenta following this Boltzmann distribution, the probability for excitation into the 50S level is determined. I assume that the net optical excitation bandwidth is 5 MHz and that the optical Rydberg excitation is resonant at the lattice-field maxima. I randomly choose 10,000 ground state atom position-momentum

pairs and reduce this to include only the 1% most likely to be excited. Then, for each 50S Rydberg atom produced, its classical center-of-mass trajectory, $\mathbf{R}(t)$, is computed using a fourth order Runge-Kutta method. This is done using the adiabatic ponderomotive lattice potential $V_{\mathrm{ad,50S}}(\mathbf{R})$, calculated via Equation 5.5. To obtain satisfactory statistics, the procedure is repeated until the simulated sample contains 10,000 realizations of the Rydberg-atom evolution. After performing the simulation for a set of microwave detunings, I obtain simulated microwave spectra by plotting the average final 51S population vs the microwave detuning. The Rabi frequency of the microwave transition is adjusted to yield good agreement between on-resonant experimental and simulated 51S probabilities without lattice. Experimental and simulated spectra are compared in Figure 5.2.

To visualize the types of trajectories that, at a given microwave detuning, contribute the most to the observed microwave spectrum, I identify the subset $S_{0.01}$ of 1% of all simulated Rydberg atom trajectories that result in the highest microwave transition probabilities. In Figure 5.3, I show the $S_{0.01}$-subsets of Rydberg atom trajectories for three values of microwave detunings intended to correspond to the features A, B, and C observed in the 50S $\rightarrow$ 51S microwave spectrum. Parameters selected for this simulation are tailored to match the experimental parameters used to measure the data shown in Figure 5.2.

Panel (a) of Figure 5.3 shows the $S_{0.01}$-subset of trajectories at a -430 kHz shift of the 50S $\rightarrow$ 51S transition, *i.e.* the frequency shift at which the A-signal is observed in Figure 5.2. This frequency offset is equal to the -430 kHz frequency shift of the 50S $\rightarrow$ 51S transition that an atom frozen at a lattice maximum (hyperbolic fixed point in Figure 5.1) would experience. Inspecting the histogram in the top panel of Figure 5.3, it is seen that the $S_{0.01}$-subset of trajectories at -430 kHz indeed spend a vast

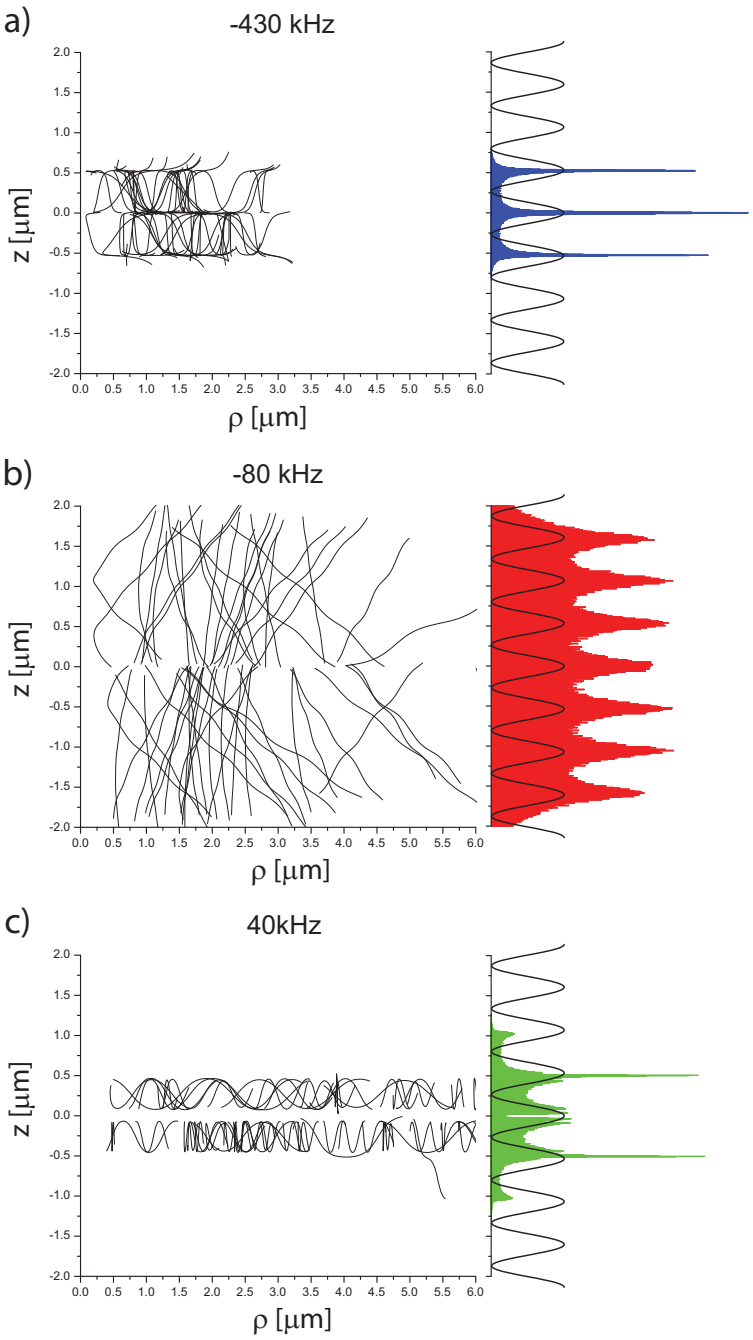

Figure 5.3: Calculated $S_{0.01}$-subset of Rydberg atom trajectories in a ponderomotive optical lattice for the same parameters as in Figure 5.2 and for the indicated values of the microwave detuning (-430 kHz, -80 kHz, and 40 kHz from top to bottom). The histograms on the right show the corresponding probability distributions along the z-coordinate.

majority of their time near lattice maxima, while only occasionally sampling other parts of the lattice. These atoms have total energies in the range of V_0 and correspond

to the pink region in the phase-space map in Figure 5.1. The simulation hence confirms that the A-component of the microwave spectrum in Figure 5.2 corresponds to atoms on trajectories that do not deviate much from the lattice maxima.

Panel (b) shows the $S_{0.01}$-subset of trajectories that give rise to a -80 kHz shift, corresponding to the B-peak in the microwave spectrum in Figure 5.2. There is a striking difference between the trajectories seen in panels (b) and (a): atoms with trajectories shown in panel (b) have enough energy after excitation to roam over many lattice wells during the given interaction time. Inspecting the histogram in the middle panel of Figure 5.3, it is seen that the atoms spend only little more time in regions where the 50S $\rightarrow$ 51S transition is red-shifted (lattice maxima) than they do in regions where the transition is blue-shifted (lattice minima). Hence, on average there is only a small net red shift, in agreement with the small negative shift of the B-peak in Figure 5.2. The simulation hence confirms that the B-component of the microwave spectrum is due to atoms sampling many lattice wells, corresponding to the green area in the phase-space map in Figure 5.1. It is further found that, when exciting the Rydberg atoms near the maxima of the ponderomotive lattice, the majority of trajectories are in the green phase-space area in Figure 5.1.

Panel (c) shows a typical $S_{0.01}$-subset of trajectories that result in a +40 kHz blue shift of the 50S $\rightarrow$ 51S transition (*i.e.* in between the broad B- and the C-signatures of the microwave spectrum in Figure 5.2). Most of these these trajectories are confined to a single lattice unit cell. Hence, these atoms are trapped in a single well and cannot freely roam through the lattice. During the given atom-field interaction time (6-8 μs), the atoms have enough time to make two or three oscillations in the lattice well in which they are trapped.

In Figure 5.3 I have shown $S_{0.01}$-subsets of trajectories for several values of the

microwave detuning at which these subsets have quite uniform, distinctive characteristics. At a detuning of -430 kHz, the $S_{0.01}$-subset mostly consists of atoms spending most of their time near hyperbolic fixed points in Figure 1, at -80 kHz it mostly consists of atoms running across many lattice wells, and at +40 kHz it mostly consists of trapped atoms. It is necessary to note that for other detunings the $S_{0.01}$-subsets of trajectories are not, in general, very uniform in their qualitative characteristics. For example, in the detuning range $\gtrsim 100$ kHz both trapped trajectories as in panel (c) as well as un-trapped ones as in panel (b) contribute. Noting that the microwave excitation probability depends on both the Fourier spectrum of the microwave pulse and the time dependence of the microwave detuning imposed by the atoms' motion through the lattice, it is not very surprising that at certain microwave detunings several distinct types of trajectories contribute equally to the $S_{0.01}$-subsets.

5.5 Rydberg Atom Trapping

The number of atoms that are confined to a single lattice well depends strongly on the experimental parameters used to generate the lattice potential and on the optical Rydberg excitation frequency. In the case studied in Chapter 4, the fact that ground-state atoms are excited into Rydberg states at a potential maximum of the lattice provides the Rydberg atoms with near-maximal initial potential energy. In this case, the only atoms that can be trapped are those that are fortuitously both excited slightly displaced from a lattice maxima due to the linewidth of the excitation laser, and that also have little kinetic energy. Some of these atoms do not have enough energy to climb over lattice potentials and are trapped. From the spectra shown in Figure 5.2 and the calculated trajectories in Figure 5.3, I estimate that about 5% of all excited Rydberg atoms are trapped in the lattice over the 8 μs

atom-field interaction time.

Atoms that are trapped in a one-dimensional ponderomotive lattice will still leave the lattice transversely because the lattice potential is generally repulsive in the directions transverse to the axis of the lattice laser beams. For the lattice used in Chapter 4, atoms with a temperature of 200 μK excited on the lattice axis will leave the lattice region within about 20 μs.

For these reasons, there are two factors that need to be addressed in order to improve the trapping functionality of ponderomotive optical lattices. First, instead of exciting Rydberg atoms at lattice maxima, with near-maximal potential energy, a method needs to be found to initially prepare the Rydberg atoms in a lattice minimum. Second, the lattice-beam geometry needs to be re-designed to enable transverse trapping, resulting in a three-dimensional optical Rydberg atom trap. In the following paragraphs, I present methods to address both of these issues.

5.5.1 Improvement of longitudinal trapping performance

Since the lattice acts as a red-detuned optical dipole trap for the laser-cooled ground-state atoms, the ground-state atoms collect at the maxima of the lattice laser field. In Chapter 4, the ground-state and Rydberg-state level shifts in the optical lattice were used to selectively excite ground-state atoms trapped in the optical dipole trap into Rydberg states. As a result, the Rydberg atoms were excited at locations of high potential energy in the ponderomotive Rydberg atom trapping potential. This resulted in a low fraction of Rydberg atoms that were trapped at all, and the temperature of the trapped atoms was high. In the following, I present a method by which the fraction of trapped atoms can be greatly increased and their temperature can be reduced.

A π phase shift applied to one of the lattice laser beams immediately after Rydberg

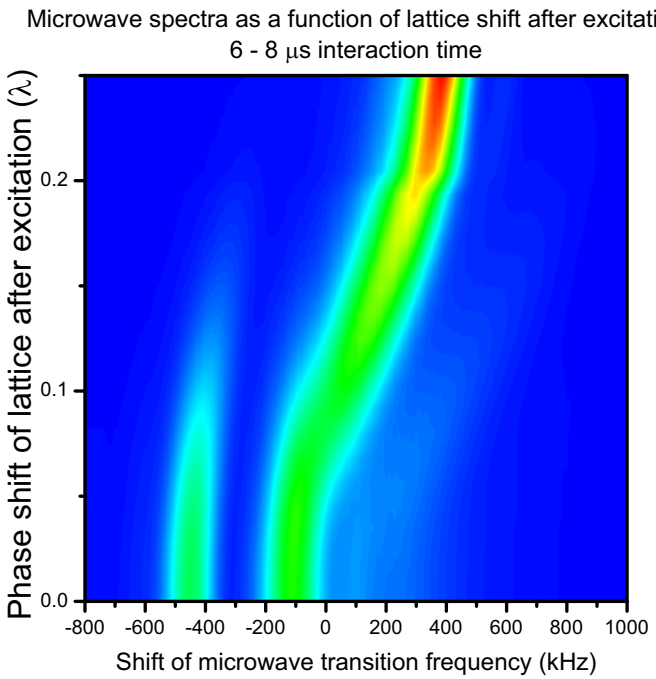

Figure 5.4: Contour plot of microwave spectra of the 50S $\rightarrow$ 51S transition as a function of microwave detuning and lattice phase shift after excitation.

excitation can serve to shift the location of the lattice potential maxima by $\lambda/4$. After the shift, atoms that are initially excited at the potential maxima will find themselves at a potential minimum. Hence, they will be efficiently trapped in the one-dimensional ponderomotive Rydberg-atom lattice. The lattice phase shift can be accomplished through a number of means, for example with a voltage-controlled waveplate. For the method to work, it is essential that the phase shift is applied over a time interval that is much shorter than the round-trip period of the atoms in the lattice wells.

Microwave spectroscopy is a powerful method to probe the effectiveness of the lattice phase shift. To show this, I have simulated microwave spectra like the one shown in Figure 5.2 as a function of an instantaneous phase shift of the lattice after Rydberg excitation. Figure 5.4 shows the simulated microwave spectra as a function of lattice phase shift. The optical Rydberg-atom excitation is assumed to

be resonant at the lattice field maxima prior to the shift. A phase shift of $\lambda/4$ corresponds to the case where the lattice is completely inverted immediately after excitation (i.e. all atoms excited to lattice maxima are instantaneously transferred to lattice minima). Figure 5.4 shows that, as the phase shift is increased from zero, the microwave spectrum undergoes an overall blue frequency shift, which is suggestive of more trapped atoms. For a phase shift of $\lambda/4$, the microwave spectrum exclusively consists of a blue-shifted peak centered at +380 kHz. This value approaches the frequency shift of +430 kHz that an atom pinned down at a ponderomotive-lattice minimum would experience. Figure 5.4 hence indicates that microwave spectroscopy is suited to prove the enhanced trapping performance, and that for a phase shift of $\lambda/4$ most Rydberg atoms should be longitudinally trapped.

Figure 5.5 shows the trajectories of atoms in a lattice with varying amounts of phase shift. The parameters used to calculate these trajectories are tailored to match the experimental parameters used to measure the data in Figure 5.2. In contrast to Figure 5.3, in Figure 5.5 I do not selectively plot trajectories that maximize the microwave transition probability at a specific microwave frequency - instead I show trajectories of random samples of Rydberg atoms optically excited in the lattice. On the right side of Figure 5.5, I show histograms of the z-positions of the atoms in the lattice. Without a lattice phase shift, most atoms roam over many wells within the lattice. They slow down near the lattice maxima, thus giving rise to the peaks in the histogram at these points. Upon closer inspection, one will find that a small percentage of the atoms are trapped, as discussed in Sections 3 and 4. If the lattice is shifted by $\lambda/8$ (atoms moved to lattice inflection points after excitation), a great majority of the atoms become trapped. These atoms exhibit a sloshing motion between the classical turning points of a single lattice site. The sloshing motion

leads to the pair of peaks in the z-probability distributions. Lastly, a $\lambda/4$ phase shift (atoms moved to lattice minima after excitation) leads to trapping of essentially all excited Rydberg atoms. These atoms are also tightly confined within a single lattice site, and will remain trapped until they exit the lattice transversely. The temperature of the trapped Rydberg atoms is similar to that of the ground-state atoms prior to excitation.

5.5.2 Three-dimensional trapping

As the ponderomotive lattice generally produces light forces pointing away from the light-field maxima, it is less straightforward to generate 3D ponderomotive traps than it is to generate attractive (red-detuned) optical dipole traps. In the following, I describe an efficient method to generate a 3D ponderomotive Rydberg atom trap using only two Gaussian beams.

A typical optical lattice formed with a pair of identical laser beams has an electric field of the approximate form

$$\sqrt{\frac{2P}{\pi w\left(z\right)}}e^{-\rho^2/w(z)^2}\left[e^{ikz+ik\frac{\rho^2}{2R(z)}-iG(z)}+e^{-ikz-ik\frac{\rho^2}{2R(z)}+iG(z)}\right] \tag{5.6}$$

where P is the total power in each beam, ρ is the distance from the axis of the beams, $w(z)$ is the beam waist, z is the coordinate along the beam axis, k is the wavenumber, $2\pi/\lambda$, R is a parameter representing the wavefront curvature and G is the Guoy phase. A transverse lattice potential gradient can be formed either by offsetting the focus of one of the laser beams from the other, or by adjusting the radial beam size of one of the beams. In any case, it is straightforward to realize conditions such that, at the location of the atoms, one beam is larger in diameter than the other. In that case, the electric field is given by

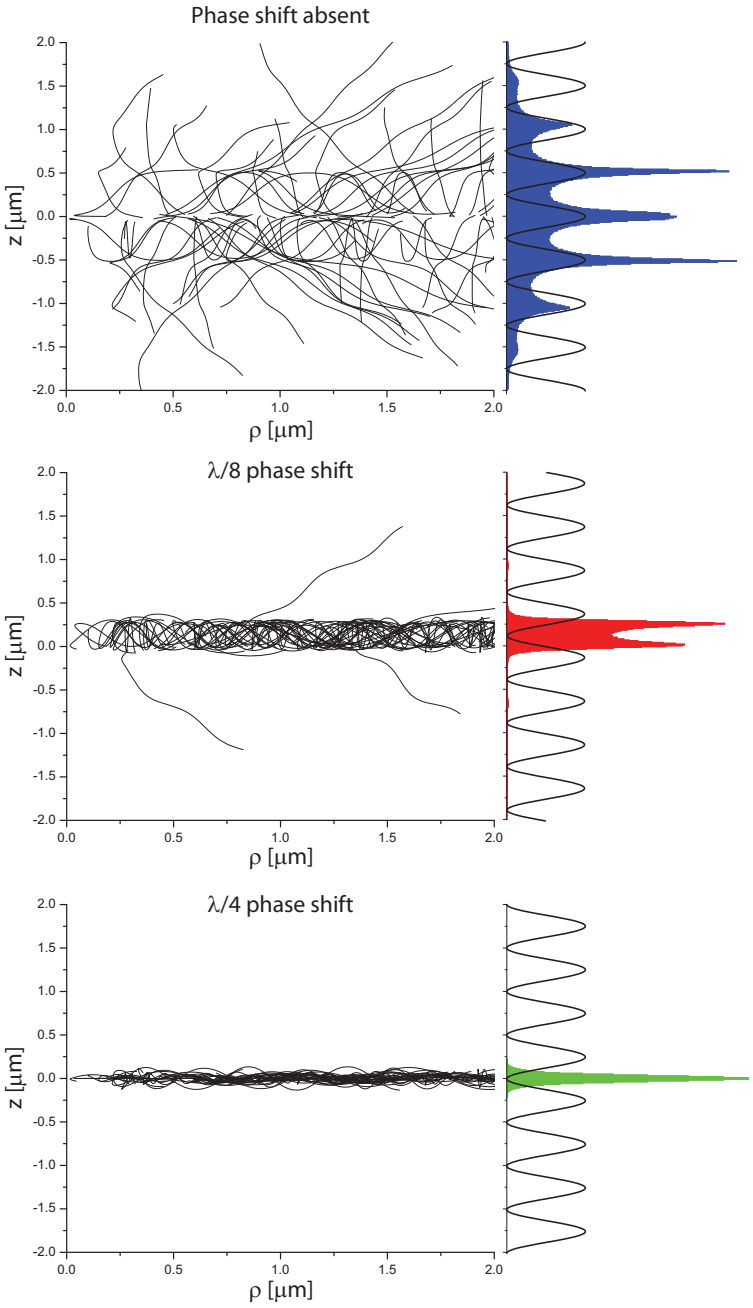

Figure 5.5: Rydberg atom trajectories for the indicated amounts of lattice shift after excitation. The right side of each graph contains a histogram of z-positions in the lattice. The sine waves overlaid on the right show the locations of the lattice maxima and minima relative to the trajectories and the histograms.

$$\sqrt{\frac{2P_1}{\pi w_1(z)}}e^{-\rho^2/w_1(z)^2}e^{ikz} + \sqrt{\frac{2P_2}{\pi w_2(z)}}e^{-\rho^2/w_2(z)^2}e^{-ikz} \quad . \tag{5.7}$$

Here, $w_1(z)$ and $w_2(z)$ are the different beam-waist functions of the beams, and

z is measured from the common focal spots. The wavefront curvature and the Guoy phase terms, as shown in Equation 6, were found to be insignificant in the parameter range of interest, and are left out in Equation 5.6 for simplicity.

The three-dimensional intensity profile of a standard optical lattice compared to a lattice where one beam is a factor of ten larger than the other is shown in Figure 5.6 panels (a) and (b). In panel (b), one can see that a transverse force is generated that will confine cold atoms near the lattice axis. I refer to this as a "bottle trap potential". The transverse potential height is about one quarter that of the longitudinal barrier.

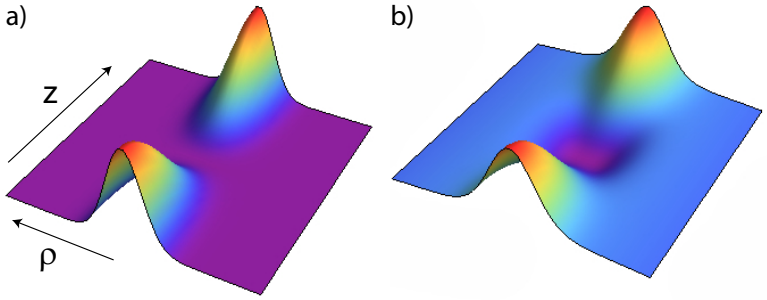

Figure 5.6: Three-dimensional intensity profiles for an optical lattice with equal beam sizes (a) and for two beams with a spot size ratio of ten to one (b).

Figure 5.7 shows two typical trajectories of atoms trapped in a potential resembling that of Figure 5.6b. In the simulation, I have combined the bottle trap potential with a $\lambda/4$ phase shift of the lattice applied immediately after excitation. The same beam intensities as in Figure 5.5 are used, however, one lattice beam has a FWHM of 1 μm while the other beam has a FWHM of 10 μm. Atoms are now confined longitudinally and transversely. The trajectories oscillate back and forth between near $\rho = 0$ and the outer edge of the trap potential near $\rho \approx 1$ μm. The apparent repulsion near $\rho = 0$ is a result of the centrifugal barrier, $L_Z^2/(2m\rho^2)$, which occurs in the three-dimensional calculation. (The calculation in Figure 5.1 was one-dimensional, hence there was no centrifugal term).

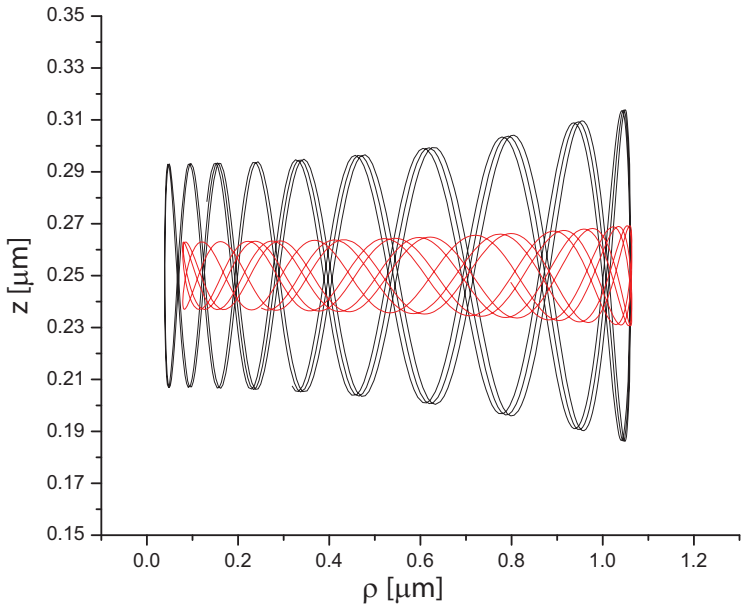

Figure 5.7: Two example trajectories of atoms in the potential shown in Figure 5.6b. Both atoms are three-dimensionally trapped, as a result of the attractive radial force that follows from the potential shown in Figure 6b. The inner turning point results from a centrifugal potential.

5.6 Conclusion

In this Chapter, I have analyzed microwave spectra and trajectories of Rydberg atoms in a ponderomotive optical lattice. These are important steps forward in tailoring the optical lattice as a trapping device. I have shown that microwave spectroscopy is an important tool in characterizing the lattice, and offered techniques for increasing the trapping efficiency. Trapping can be increased to very nearly 100% by implementing both the $\lambda/4$ phase shift and the bottle trap configuration. In the next chapter, I will consider new effects that are visible when the lattice depths are increased by a factor of 20-40. In this regime, one can describe the lattice in terms of effective electric and magnetic fields, and a direct comparison to the diamagnetic problem in classical mechanics works well to describe the system.

CHAPTER VI

Adiabatic Potentials for Rydberg Atoms in a Ponderomotive Optical Lattice

So far, the discussion in this thesis has been limited to non-degenerate (low angular momentum) states in optical lattices. Using $nS_{1/2}$ states, I have proven the existence of the ponderomotive optical lattice for Rydberg atoms, and characterized it using microwave spectroscopy as a sensitive probe. These experiments required a lattice depth of about 50 MHz for sufficient visibility of the theorized microwave shifts. This depth is much less than would be necessary to mix the nS states with other nearby Rydberg states. Some interesting effects occur, however, when the lattice potential becomes deep enough such that state-mixing does occur.

In this chapter, I show how the adiabatic potentials for degenerate states in a one-dimensional ponderomotive optical lattice can be calculated, and use effective electric and magnetic fields to obtain insight into the underlying physics. This work contrasts with previous calculations of ponderomotive optical lattice potentials, where electric and magnetic fields were used to deliberately remove the degeneracy of the Rydberg states in order to eliminate the mixing between different states [40]. Near the inflection points of the lattice potential and for sufficiently low principal quantum numbers ($n <\sim 35$ in the cases studied), the adiabatic level structure resembles that of the dc Stark effect, and an effective electric-field model can be used to model the

lattice-induced perturbation. Near the nodes and anti-nodes of the lattice field, the adiabatic level structure exhibits a combination of adjacent rotational and vibrational energy level sequences. Here, an analogy between the ponderomotive optical lattice and the diamagnetic problem works well to interpret the lattice-induced perturbation in terms of an effective magnetic field.

The adiabatic potentials for atoms in an optical lattice can be calculated semi-classically by treating the internal dynamics quantum mechanically along with a classical description of the center of mass motion. At each position in space, the atom-field interaction Hamiltonian is obtained and diagonalized, yielding position-dependent adiabatic energy eigenvalues. The adiabatic potential surfaces are generated by plotting the eigenvalues versus position. This method is discussed in detail in Section 6.2.

6.1 Adiabatic potentials of Rydberg atoms in a ponderomotive optical lattice

In the familiar case of ground-state atoms subjected to an optical lattice, adiabatic trapping potentials and wave-functions result from an atom-field interaction that typically couples a few low-lying atomic states. In most cases, the excited states are adiabatically eliminated, and spatially periodic light-shift potentials are obtained for the ground state levels [63]. Sometimes, state mixing due to lattice-induced Raman couplings between magnetic sub-levels of the ground state occurs.

As discussed in Chapter 4 and Appendix B.3, a different approach is usually taken for Rydberg states. While Rydberg levels are ground-state-like in that they have long lifetimes (typically $\sim 100\ \mu$s), lattice lasers applied to a Rydberg atom usually are not near-resonant with any optical transition, because transitions between Rydberg levels are in the GHz and THz frequency range. (I assume a generic case in which the

lattice laser does not significantly couple the Rydberg level of interest down to a low-lying atomic level.) Following methods used for ground-state atoms, one may obtain the light shifts and state mixing of Rydberg atoms in optical lattices by summing over the effects of virtual transitions to all available atomic states, as well as over all transitions through the continuum. A more practical method is based on the fact that the (optical) laser frequency is several orders of magnitude higher than the Kepler frequency of the Rydberg atom. Consequently, the effect of the laser field can be treated via a Born-Oppenheimer separation of variables, in which the dynamics at the optical frequency are accounted for by adding a Born-Oppenheimer potential to the equations that govern the dynamics in the slow degree(s) of freedom [40, 76]. The Born-Oppenheimer potential for the case of a (quasi-)free electron in a laser field is just the previously-discussed ponderomotive potential[4], or the time-averaged kinetic energy of the free electron in the oscillating electric field of the laser as described in Equation 4.5.

Besides the fact that the origin of the light shifts of ground-state and Rydberg atoms is fundamentally different, there are additional differences between these two cases. Since the size of Rydberg atoms is on the order of the lattice period, Rydberg atoms sample an entire region of the lattice at once (this is the origin of the state-dependent shifts discussed in Chapter 4), while ground-state atoms usually are considered as point-like particles in relation to the lattice period. The ratio between Rydberg-atom size and lattice period can be tuned over a wide range around unity via the principal and the magnetic quantum numbers. Further, the number of states being coupled by the lattice field is much larger for Rydberg atoms than it is for ground-state atoms. The adiabatic wave-functions of the Rydberg electron in pon-

[4]Full quantum-mechanical expressions for the ponderomotive potential and the free-electron state in a laser field are provided by [76] and references therein.

deromotive optical lattices typically are coherent superpositions of 10's to 100's of states. Also, these wave-functions vary as a function of the center of mass coordinate of the atom in the lattice. This is in contrast to the case of ground-state atoms in an optical lattice, in which the adiabatic wave-functions are spatially varying spin-states.

6.2 Calculation of adiabatic potentials

The adiabatic potential surfaces shown in this thesis are calculated by adiabatically eliminating the electron quiver motion from the center of mass motion of the atom via the Born-Oppenheimer approximation along the lines of reference [40]. The result of this elimination is that an optical standing wave of the type of Equation (4.2) adds a ponderomotive lattice potential

$$V_{\mathrm{P}} = \frac{1}{2} V_0 \left(1 + \cos\left(2k\left(z + z_0\right)\right)\right) \tag{6.1}$$

to the inner-atomic Coulomb potential. Here, $V_0 = \frac{e^2 E_0^2}{m_e \omega^2}$ with single-beam electric field E_0, z_0 is the atomic center of mass coordinate, and z is the relative (internal) coordinate of the Rydberg electron. The full atomic Hamiltonian, in atomic units, is then

$$H = \frac{p^2}{2} - \frac{1}{r} + V_c(r) + V_{\mathrm{P}}(z + z_0) + V_{LS} \tag{6.2}$$

where $V_c(r)$ is a short-range core potential accounted for by using the proper quantum defects of the atom and V_{LS} is the fine-structure. The variable z_0 is a classical parameter of the Hamiltonian (not an operator).

The following analysis is similar to the theoretical outline found in reference [41] with the fine-structure of the Rydberg atom now taken into account to include all possible state mixing. The lattice potential can be expanded in a Taylor series about

$z = 0$:

$$1 + \cos\left(2k\left(z + z_0\right)\right) = \sum_{p=0}^{\infty} K_p z^p \tag{6.3}$$

where the coefficients K_p are given by

$$K_p = \frac{(2k)^p}{p!} \begin{cases} (-1)^{p/2} \cos\left(2kz_0\right) + \delta_{p,0} & , \quad p \text{ even} \\ (-1)^{(p+1)/2} \sin\left(2kz_0\right) & , \quad p \text{ odd} \end{cases} \tag{6.4}$$

where $\delta_{p,0}$ is a Kronecker-delta.

In the bound energy range of the Rydberg atom, the Hamiltonian including fine structure can be represented in the basis $\{|n, l, j, m_j\rangle\}$ as

$$H_{n,l,j,m_j}^{n',l',j',m'_j} = E_{n,l,j}\delta_{n,n'}\delta_{l,l'}\delta_{j,j'}\delta_{m_j,m'_j} + \frac{1}{2}V_0\delta_{m_j,m'_j}\sum_{p=0}^{\infty}\Big\{K_p\ (r^p)_{n,l,j}^{n',l',j'} \times$$
$$\left[C^*_{l,j,m_j,\uparrow}C_{l',j',m_j,\uparrow}\left(\cos^p\theta\right)_{l,m_j-1/2}^{l',m_j-1/2} + C^*_{l,j,m_j,\downarrow}C_{l',j',m_j,\downarrow}\left(\cos^p\theta\right)_{l,m_j+1/2}^{l',m_j+1/2}\right]\Big\} \tag{6.5}$$

where the $E_{n,l,j}$ are the non-perturbed energy levels, and $(r^p)_{n,l,j}^{n',l',j'}$ and $(\cos^p\theta)_{l,m_j\pm1/2}^{l',m_j\pm1/2}$ are the radial and angular matrix elements induced by the optical lattice, respectively. The $C_{l,j,m_j,\uparrow}$ and $C_{l,j,m_j,\downarrow}$ denote Clebsch-Gordan coefficients for the electron spin in the angular state $|l, j, m_j\rangle$ pointing up or down, respectively. The radial matrix elements, $(r^p)_{n,l,j}^{n',l',j'}$, are calculated numerically using the quantum defects of the atom of interest. The quantization axis for the m_j-quantum number is along the laser beam direction for the ponderomotive optical lattice. Due to the resulting azimuthal symmetry, the magnetic quantum number m_j is conserved. The angular matrix elements can be written as

$$\begin{aligned} \left(\cos^p\theta\right)_{l,m}^{l',m} &= (-1)^m\, p! \sum_{\tilde{l}=p,p-2,\ldots,0} \left\{ \frac{\left(2\tilde{l}+1\right)\sqrt{(2l+1)\,(2l'+1)}}{2^{\left(p-\tilde{l}\right)/2}\left(\frac{p-\tilde{l}}{2}\right)!\left(p+\tilde{l}+1\right)!!} \times \right. \\ &\qquad \left. \begin{pmatrix} l' & \tilde{l} & l \\ 0 & 0 & 0 \end{pmatrix} \begin{pmatrix} l' & \tilde{l} & l \\ -m & 0 & m \end{pmatrix} \right\} \\ &= (-1)^m\, p!\, \Lambda(l, l', m, p) \quad , \end{aligned} \tag{6.6}$$

where $m = m_j \pm 1/2$. Using $\Lambda(l, l', m, p)$ as defined in Equation (6.6) and after some rearrangement, one finds

$$H^{n',l',j',m'_j}_{n,l,j,m_j} = E_{n,l,j}\delta_{n,n'}\delta_{l,l'}\delta_{j,j'}\delta_{m_j,m'_j} + \frac{1}{2}V_0\delta_{m_j,m'_j}\left(-1\right)^{m_j-1/2+\left(\tilde{l}_{\min}+\eta\right)/2} \times$$
$$\sum_{p=\tilde{l}_{\min},\tilde{l}_{\min+2},\cdots} \left\{\left(-1\right)^{\left(p-\tilde{l}_{\min}\right)/2}\left(2k\right)^p\left(r^p\right)^{n',l',j'}_{n,l,j}\left[\cos\left(2kz_0 - \frac{\eta\pi}{2}\right) + \delta_{p,0}\right] \times \right.$$
$$\left.\left[C^*_{l,j,m_j,\uparrow}C_{l',j',m_j,\uparrow}\Lambda(l,l',p,m_j-1/2) - C^*_{l,j,m_j,\downarrow}C_{l',j',m_j,\downarrow}\Lambda(l,l',p,m_j+1/2)\right]\right\} \tag{6.7}$$

Here, the value $\tilde{l}_{\min} = |l - l'|$ and $\eta = 0$ or 1 for even and odd $\tilde{l}_{\min}$, respectively. Once the Hamiltonian is obtained, the eigenvalues and adiabatic potentials are determined as described in the introduction.

6.3 Some illustrative adiabatic potentials

6.3.1 Overview

In accordance with the experiment presented in Chapter 4, in these calculations I have used the quantum defects of rubidium and a lattice laser wavelength of 1064 nm. Figure 6.1 shows the adiabatic potentials versus the center-of-mass atomic position, z_0, for the hydrogenic states of $n = 30$, m_j=2.5 with a lattice depth V_0 =2 GHz. Figures 6.2 and 6.3(a) show the corresponding potentials for $n = 45$ and $n = 65$. The value of m_j=2.5 is chosen for the simulation because it corresponds to the state that would be reached when exciting out of a $P_{3/2}$ state and using σ^+ optical pumping. The anti-nodes of the optical lattice occur at $0, \pm\lambda/2, \pm\lambda \ldots$ and the nodes at $\pm\lambda/4, \pm 3\lambda/4 \ldots$

Since in all cases studied in this thesis the lattice depth is much less than the Kepler frequency, lattice-induced state mixing only extends over states of similar effective quantum numbers. Hence, the lattice potential primarily mixes the levels

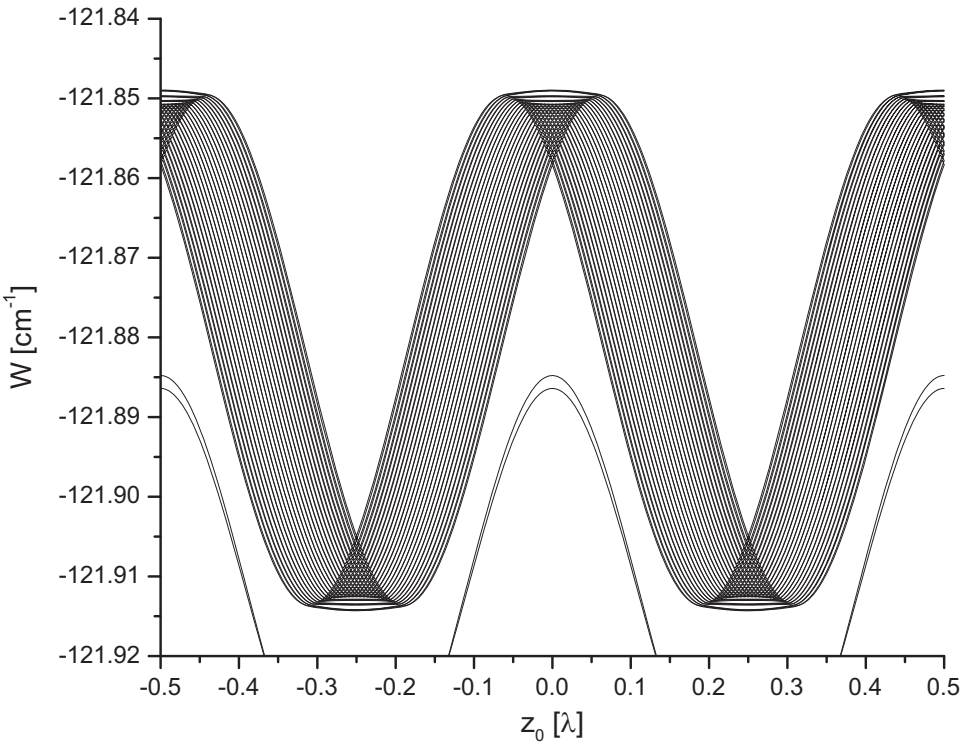

Figure 6.1: Adiabatic potentials in wavenumbers, W, for an optical lattice with V_0=2 GHz, $n = 30$ and $m_j = 2.5$. These potentials exhibit distinct regions of approximately linear and quadratic behavior, explained in the text.

with zero quantum defect (for rubidium these are all levels with angular momentum $l \geq 5$). With increasing ratio of lattice depth to the Kepler frequency, the G and F-levels may mix with the hydrogenic levels as well. For Rydberg states with principal quantum numbers $n \lesssim 35$, the adiabatic potentials exhibit a simple structure resembling a set of interlaced sine-like curves that are all quite similar to the underlying free-electron ponderomotive potential, Equation (6.1). This behavior can be readily explained as follows. Each of the adiabatic states that correspond to potentials shown in Figure 6.1 is a superposition of many Rydberg states. All components of the superposition states have sizes less than a lattice period and, hence, the sizes of the adiabatic state wave-functions are also less than a lattice period. As a consequence, all adiabatic states experience a shift that approximately equals the

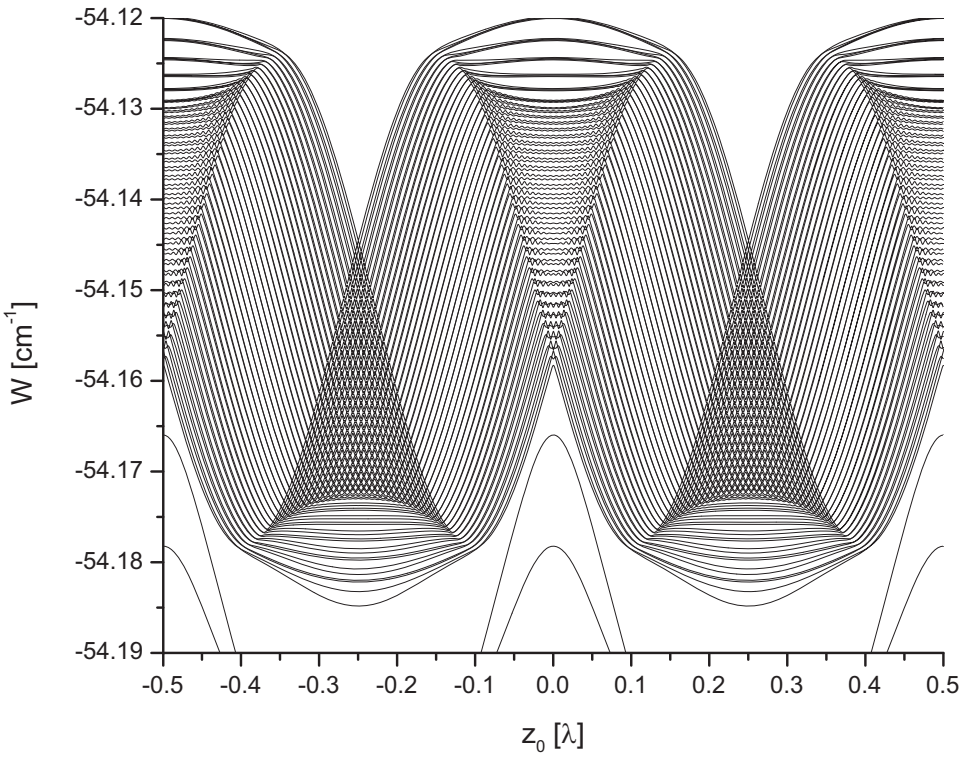

Figure 6.2: Adiabatic potentials for an optical lattice with V_0=2 GHz, $n = 45$ and $m_j = 2.5$. The linear region over which the lattice perturbation can be modeled as an effective electric field is much narrower than that for $n = 30$ (see figure 6.1).

free-electron ponderomotive potential evaluated at the center-of-mass location of the atom, which corresponds to setting $z = 0$ in Equation (6.1).

Considering the detailed behavior of the adiabatic potentials in Figure 6.1, one notes several qualitatively different regions. Between the nodes and anti-nodes, most adiabatic potentials are approximately straight, non-intersecting curves. In these regions, the lattice perturbation can be modeled via an effective electric field, as discussed in section 6.3.2 below. Near the nodes (anti-nodes) of V_{P}, I find regions of intersecting potentials and, below (above) in energy, regions of nearly flat, non-intersecting potential curves with non-uniform energy separations. In these regions, the lattice-induced perturbation is quadratic and can be modeled via an effective magnetic field, as discussed further in sections 6.3.3 and 6.3.4.

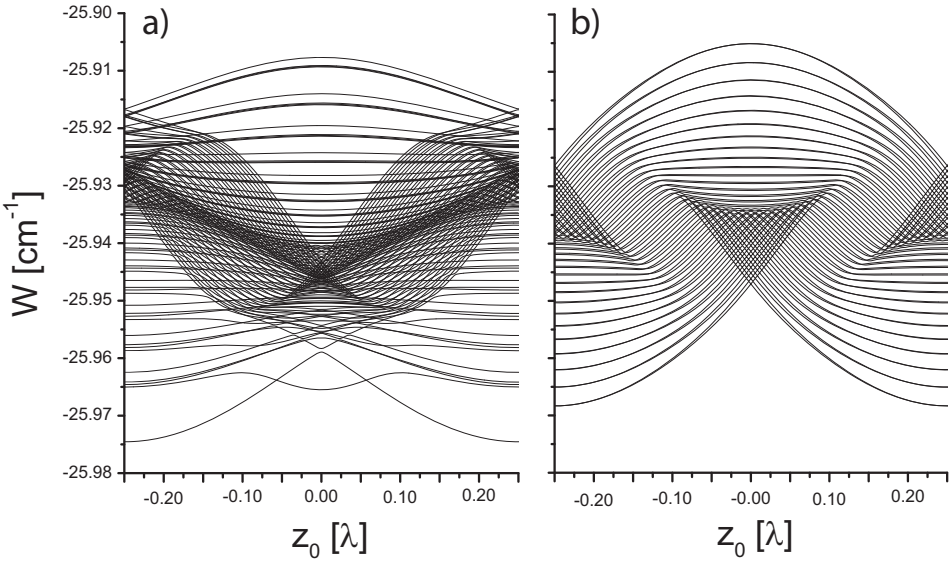

Figure 6.3: Adiabatic potentials for an optical lattice with V_0=2 GHz, $n = 65$ and $m_j = 2.5$ (panel (a)) and $m_j = 32.5$ (panel (b)). For $m_j = 2.5$, because of the extent of the Rydberg atom wave-function, there are no longer clear distinctions between different regions of the lattice, as the wave-function of the Rydberg atom averages over many parts of the potential. For $m_j = 32.5$, the number of states is reduced and the linear- and quadratic-like regions reemerge (see text).

With increasing principal quantum number, the atomic diameter (of order $2n^2$ to $4n^2$) approaches and eventually exceeds the lattice period, and the number of levels that substantially mix increases. As a result, as n increases the sets of adiabatic potentials appear more widely spread out (Figure 6.2), and eventually form convoluted patterns (Figure 6.3). This behavior reflects the fact that, once the wave-function of the atom extends over a significant part of the lattice period (532 nm), the effective electric and magnetic field models are no longer applicable.

I note that the sets of adiabatic potentials near the anti-nodes and the nodes ($z_0 = 0$ versus $z_0 = \pm\lambda/4$) are not exactly symmetric to each other under the transformation $z_0 \rightarrow z_0 \pm 0.25\lambda$ and $W \rightarrow -W + const.$ The asymmetry is most easily seen for higher n-values, such as in Figures 6.2 and 6.3(a). The deviation from perfect symmetry is due to the quantum defects, which lead to an asymmetric placement of several unperturbed low-angular-momentum levels (S, P, D, F and G)

about the hydrogenic manifolds.

In Figures 6.1 and 6.2, there are two adiabatic potentials that are slightly offset toward lower energy from the main manifold and that exhibit a fairly simple spatial dependence. These potentials correspond, respectively, to the 30G and 45G Rydberg states that have a quantum defect of 0.00405 [77]. In Figures 6.1 and 6.2, the adiabatic potentials for the G-levels are less complex than what is seen for the bulk of quantum-defect-free levels because the G-levels are sufficiently non-degenerate from the quantum-defect-free levels that minimal lattice-induced state-mixing occurs. In both figures, there are two adiabatic potentials for the G-state, because the m_j=2.5 manifold contains both $|n, l = 4, m_l = 2, m_s = 1/2\rangle$ and $|n, l = 4, m_l = 3, m_s = -1/2\rangle$ components, with n=30 and 45, respectively. As the fine structure coupling of the G-components is very small, they do not mix and exhibit slightly different lattice-induced shifts. Hence, the adiabatic potentials at the bottom of Figures 6.1 and 6.2 correspond to adiabatic electronic states that are approximately given by $|n, l = 4, m_l = 2\rangle$ and $|n, l = 4, m_l = 3\rangle$. In Figure 6.3, the lattice-induced coupling is strong enough that the G-levels are mixed into the manifold of quantum-defect-free levels.

Further qualitative changes are observed when varying m_j while keeping n fixed. In Figure 6.3, I compare the adiabatic potentials for $n = 65$ and $m_j = 2.5$ (panel (a)) and $m_j = 32.5$ (panel (b)). As m_j is increased, the quantum states generally become more pancake-like and extend over a smaller range of z. As a result, the larger the value of m_j, the higher the value of n up to which the ponderomotive lattice can be modeled using effective electric and magnetic fields. This is because the effective-fields model gradually loses validity as the extension of the quantum states in the z-direction approaches the lattice period. For instance, Figure 6.3(b) clearly breaks

up into a region resembling the Stark effect and a region resembling a diamagnetic spectrum, while Figure 6.3(a) is much more complex and no such analogy can be made. It is also noted that in the case of Figure 6.3(b) all states in the manifold are quantum-defect-free, and the adiabatic potentials exhibit perfect symmetry under the transformation $z_0 \rightarrow z_0 \pm 0.25\lambda$ and $W \rightarrow -W + const.$

6.3.2 Effective Electric Field

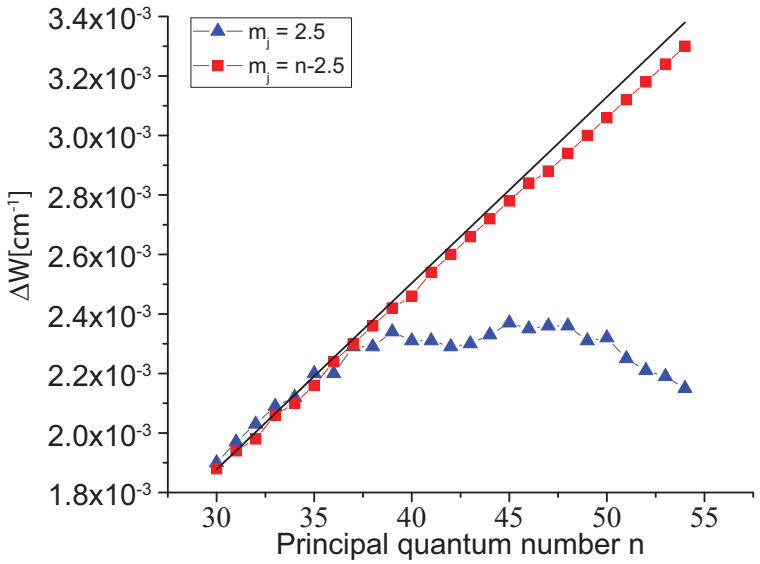

Figure 6.4: Splitting between adjacent adiabatic potential lines at the inflection point of the lattice for m_j=2.5 (a) and m_j=n-2.5 (b). The splitting values for $m_j = n - 2.5$ are multiplied by a factor of two (see text). The solid line shows the splitting predicted by the effective electric field model.

For atomic center-of-mass positions, z_0, near the inflection points of the ponderomotive potential, Equation (6.1), and for Rydberg-atom wave-functions with sufficiently small extension in the z-direction, the potential can be modeled using an effective electric field. The maximum gradient (and thus maximum force) occurs at the inflection points of Equation (6.1) and has a value of $V_0 k$, corresponding to an effective electric field of $F = V_0 k/e$. For a lattice depth of 2 GHz, the effective electric field at the inflection point is $F = 0.49$ V/cm. Using this value, the spacing between the adiabatic potential curves near the lattice inflection points can be pre-

dicted for all n via $\Delta W = 3nF$ (in atomic units). Figure 6.4 shows the predicted values of ΔW using this effective electric field model, along with the actual spacing between the adiabatic potential lines for a range of n and m_j=2.5 (blue triangles) and m_j=$n - 2.5$ (red squares). For m_j=2.5, the effective electric field model predicts ΔW well up until $n \approx 37$. For higher n, the values for ΔW become relatively constant, and then start to decrease around $n = 50$. This behavior is attributed to the fact that with increasing n the wave-functions of Rydberg atoms located at an inflection point increasingly extend into regions of decreasing potential gradient, *i.e.* smaller effective electric fields.

The n-value up to which the effective electric field model holds increases with m_j, because with increasing m_j the wave-functions become more and more concentrated in the plane transverse to the lattice quantization axis (the xy-plane). For the case $m_j = n-2.5$ shown in Figure 6.4, only a few near-circular Rydberg states are present in the calculation. Since these states mostly extend in the xy-plane, they do not average over the lattice potential as much as the lower-m_j states. The red squares in Figure 6.4 show that for $m_j = n-2.5$, the model of an effective electric field remains valid over a much larger n-range than for low m_j. As a minor aside, it is noted that for large m_j there is no fine structure coupling. As a result, the computation of adiabatic potentials for m_j yields two decoupled manifolds of states, namely one with $m_l = m_j - 1/2, m_s = 1/2$ and another with $m_l = m_j + 1/2, m_s = -1/2$. Looking at both manifolds combined in one plot, the adiabatic levels are interlaced in a way that the apparent level spacing equals $(3/2)nF$. In contrast, at low values of m_j, the adiabatic potentials are grouped in pairs of two with a pair-to-pair spacing of $3nF$ (see Figures 6.1 and 6.2 near $z_0 = \pm\lambda/8$). To compare the cases m_j=2.5 and $m_j = n-2.5$ in Figure 6.4, I multiply the spacing observed for the case $m_j = n-2.5$

by a factor of two.

The n-range over which the effective electric field model is applicable can be estimated for low angular momentum states (blue triangles in Figure 6.4) using the condition that the diameter of the atom must be less than half the lattice period, $4n^2 < \lambda/4$. This yields $n < 35$, which agrees well with what is seen in Figure 6.4. For near-circular states (red squares), I estimate, based on the scaling behavior of radial and angular wavefunctions, that the effective electric field model should be valid up to $n \sim 250$.

6.3.3 Effective magnetic field

Figure 6.6 shows a zoomed-in part of the spectra depicted in Figure 6.1 centered around the anti-node of the lattice at $z_0 = 0$. The highest energy levels resemble those that would be obtained for a rigid rotator (energy level spacings progressively increasing), while the bottom of the spectra looks more like the energy levels of a harmonic oscillator (fixed energy level spacings). This phenomenology is very similar to that found for Rydberg atoms in a magnetic field in the l-mixing regime, *i.e.* a regime in which the magnetic field is strong enough that the l-states of a given n-manifold become mixed. The term responsible for the l-mixing is the diamagnetic interaction: $\frac{1}{8}B^2r^2\sin^2\theta$ in atomic units. In the following, I show that there is indeed a close similarity between the diamagnetism of Rydberg atoms in the l-mixing regime and the adiabatic spectra observed near the maxima and minima of ponderomotive optical lattices.

To establish the relationship between the diamagnetic perturbation and the ponderomotive optical lattice, I consider the lattice-induced perturbation of the Rydberg electron potential for an atom with center-of-mass position located at a maximum

of the standing-wave light field ($z_0 = 0, \pm\lambda/2, \pm\lambda, ...$):

$$V = \frac{1}{2} V_0 \left(1 + \cos 2kz\right). \tag{6.8}$$

This potential can be approximated up to second order, yielding a harmonic approximation of the perturbation that is valid for Rydberg atoms with wave-functions much smaller than the lattice period:

$$\begin{aligned} V &\approx \frac{V_0}{2}\left[1 + 1 - \frac{1}{2}\left(2kz\right)^2\right] \\ &= V_0 - \frac{4\pi^2 V_0}{\lambda^2} z^2 \qquad (6.9) \\ &= V_0 - \frac{4\pi^2 V_0}{\lambda^2} r^2 \left(1 - \sin^2\theta\right) \\ &= \left[V_0 - \frac{4\pi^2 V_0}{\lambda^2} r^2\right] + \frac{4\pi^2 V_0}{\lambda^2} r^2 \sin^2\theta \qquad (6.10) \end{aligned}$$

This expression shares the $r^2 \sin^2\theta$-term with the diamagnetic perturbation, has an irrelevant constant, V_0, and includes a term $\propto -r^2$. The $r^2 \sin^2\theta$-term of the lattice-induced perturbation leads to the striking similarities between diamagnetic spectra and adiabatic energy levels of Rydberg atoms near the maxima of ponderomotive lattices. The term $\propto -r^2$ is only present in the ponderomotive-lattice case; it is, obviously, responsible for some quantitative differences observed between the diamagnetic case and the ponderomotive-lattice case. Comparing the respective pre-factors of the $r^2 \sin^2\theta$-term and using $V_0 = e^2 E_0^2/(m_e \omega^2)$, I find that the ponderomotive potential for a Rydberg atom situated at a lattice maximum corresponds to an effective magnetic field:

$$\begin{aligned} \frac{e^2 B^2}{8 m_e} &= \frac{4\pi^2 V_0}{\lambda^2} \\ B^2 &= \frac{8\pi E_0^2}{\omega^2 \lambda^2} \\ B &= \frac{\sqrt{2} E_0}{c}, \end{aligned} \tag{6.11}$$

where E_0 is the electric-field amplitude of a single laser beam forming the ponderomotive lattice[5]. Similarly, for Rydberg atoms located at the nodes ($z_0 = \pm\lambda/4\ldots$) the lattice-induced perturbation of the Rydberg electron potential is

$$V(z) \approx \frac{4\pi^2 V_0}{\lambda^2} z^2 \tag{6.12}$$

$$= \frac{4\pi^2 V_0}{\lambda^2} r^2 - \frac{4\pi^2 V_0}{\lambda^2} r^2 \sin^2\theta. \tag{6.13}$$

Aside from an additive constant V_0, this is the negative of Equation (6.10). This symmetry is the reason for the (approximate) symmetry of the adiabatic lattice potentials under the transformation $z_0 \to z_0 \pm 0.25\lambda$ and $W \to -W + const.$

The effect of the diamagnetic perturbation has been studied in great detail [78–81]. In these papers, it has been established and explained why the diamagnetic perturbation leads to adjacent rotor-like and vibrator-like energy level sequences; these are very similar to the level sequences seen at $z_0 = 0$ in Figure 6.6 and in several other figures in this chapter. The rotor-like and vibrator-like energy level sequences have a noteworthy explanation based on classical mechanics. Classically, in both the diamagnetic problem and in ponderomotive lattices (for atoms situated at $z_0 = 0$ and not too large in size), there exist two types of precession patterns of perturbed Kepler orbits [79]. In one type, the electron orbit remains mostly aligned with the magnetic-field axis or the lattice-beam direction with the semi-major axis precessing about that direction. This type of precession behavior corresponds to the vibrational states in the spectrum, found on the lower-energy side of the manifold. In the other type, the electron orbit remains mostly aligned in the plane transverse to the magnetic field (or the lattice-beam direction), and the semi-major axis periodically precesses through that plane. This type of precession behavior corresponds to the rotational

[5]The first term in this equation is just the diamagnetic term mentioned at the beginning of this section. For the purposes of illustrating how the effective magnetic field is related to the applied electric field, I have written the term in SI units

states in the spectrum, found on the high-energy side of the manifold.

The electronic wave-functions of Rydberg states at z_0=0 closely reflect the probability distributions that follow from the above described classical dynamics. In Figure 6.5, the squares of the magnitudes of the wave-functions for three different states are shown. To simplify the discussion, the wave-functions are calculated for an optical lattice without fine structure or quantum defects. In each case, the atom is located at position $z_0 = 0$. The wave-functions are cylindrically symmetric about the axis of the lattice. Panel (a) shows the fundamental vibrational state. This is the lowest-energy state, and its wave-function extends along the axis of the lattice. Panel (b) shows an intermediate state. Compared to the lowest-energy vibrational state, this intermediate state has some excitation transverse to the lattice, and it has a rather complex node-line structure. Panel (c) shows the highest energy state. This state extends entirely in the plane transverse to the lattice and thus is purely rotational. For reference, panel (d) shows the adiabatic potentials for all of the $n = 30$ states. The states corresponding to the wave-functions in panels (a), (b), and (c) are labeled.

I note that the wave-function squares of vibrational states located at $z_0 = 0$ have two symmetric lobes, one pointing along $+z$ and the other along $-z$. The wave-function amplitude of the state displayed in Figure 6.5(a) is symmetric under z-inversion. There exists another, practically degenerate vibrational state that is anti-symmetric under $z-$inversion and whose energy exceeds the energy of the symmetric state only by a minute amount. This behavior reflects the fact that the underlying classical system has two degenerate vibrational electron orbits, one extending along positive and the other along negative z. The analogous quantum system exhibits near-degenerate, symmetric and anti-symmetric wave-functions with lobes pointing

along the $+z$ and $-z$ directions. In fact, a close study of Figure 6.5(d) reveals that all vibrational states come in pairs of almost degenerate states; these pairs are near-identical states, one of which is symmetric and the other is anti-symmetric under z-inversion. An inspection of Figure 6.5(d) also shows that the near-degeneracy is lifted as soon as z_0 deviates from $z_0 = 0$ (i.e. away from the center of the graph). The rotational states do not exhibit this near-degeneracy.

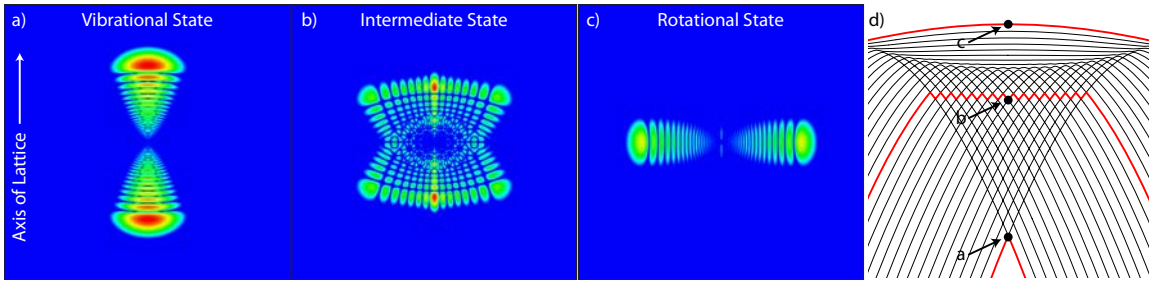

Figure 6.5: Wave-function amplitude squared for an $n = 30$ atom at $z_0 = 0$ for three different states, and the corresponding set of adiabatic potentials. Wave-functions and potentials are calculated without fine structure or quantum defects. (a) The lowest-energy adiabatic potential is a state that is purely vibrational and thus extends along the axis of the lattice. (b) The wave-functions for higher energies compared to that shown in (a) gain more excitation transverse to the axis of the lattice. (c) The highest-energy adiabatic potential corresponds to a state that is purely rotational, extending in the plane transverse to the lattice axis. (d) Adiabatic potentials near $z_0 = 0$. The black dots identify the energies and locations for which the wave-functions are calculated.

6.3.4 Parallel electric and magnetic fields

Finally, I consider the case of atoms located in the vicinity of $z_0 = 0$, at a distance less than about $\lambda/8$. As discussed in the previous chapter, the curvature of the ponderomotive potential generates a quantum behavior similar to that found in an equivalent magnetic field. In addition, in section 6.3.2 it has been established that a linear component of the ponderomotive potential can be modeled via an equivalent electric field. Hence, one may expect that for $z_0 \lesssim \lambda/8$ Rydberg atoms in ponderomotive lattices can be modeled using effective parallel electric and magnetic fields, with a fixed effective magnetic field $B = \frac{2\sqrt{2}E_0}{c}$ and an effective electric field

given by $F \approx -2V_0k^2z_0/e$. I thus expect a situation similar to that in reference [81], where helium Rydberg states in parallel electric and magnetic fields were studied. It has been pointed out in a number of studies that this type of system leads to three classes of states, referred to as I, II, and III [80, 82]. Classes I and II are vibrational states with a positive or negative electric dipole moment along the z-axis, respectively. States in class III are rotational states. The ratio of the electric and magnetic fields determines the classes of states that are available. In the present context, in the plots of adiabatic potentials of sufficiently small Rydberg states, the z_0-axis is analogous to an electric-field-scale, as the effective electric field $E \approx -2V_0k^2z_0/e$. Plotting the adiabatic potentials for $|z_0| \lesssim \lambda/8$, I indeed observe a striking similarity between the potential surfaces of Rydberg atoms in a ponderomotive lattice and the spectra of Rydberg atoms in parallel electric and magnetic fields. This is seen when comparing Figure 6.6 and corresponding figures in the above references, in particular the first figure in reference [81].

As can be seen in Figure 6.6, as the ratio of the effective electric and magnetic fields (linear to quadratic perturbations) increases, i.e. when moving from $z_0 = 0$ to $z_0 = \lambda/8$, all states turn into class I states. The situation is similar when moving from $z_0 = 0$ to $z_0 = -\lambda/8$, except that the effective electric field now points in the opposite direction, and all states turn into class II states.

A close look at the first figure in reference [81] and Figure 6.6 reveals several fine differences, including an upward curvature of the class III states and a lack of curvature in the class I/II states in reference [81]. These differences are attributed to the inhomogeneity of the effective electric field in the lattice and to the presence of the term $-\frac{1}{8}B^2r^2$ in the lattice-induced Hamiltonian. Nonetheless, in comparison with these differences, the overall similarity between the first figure in reference [81]

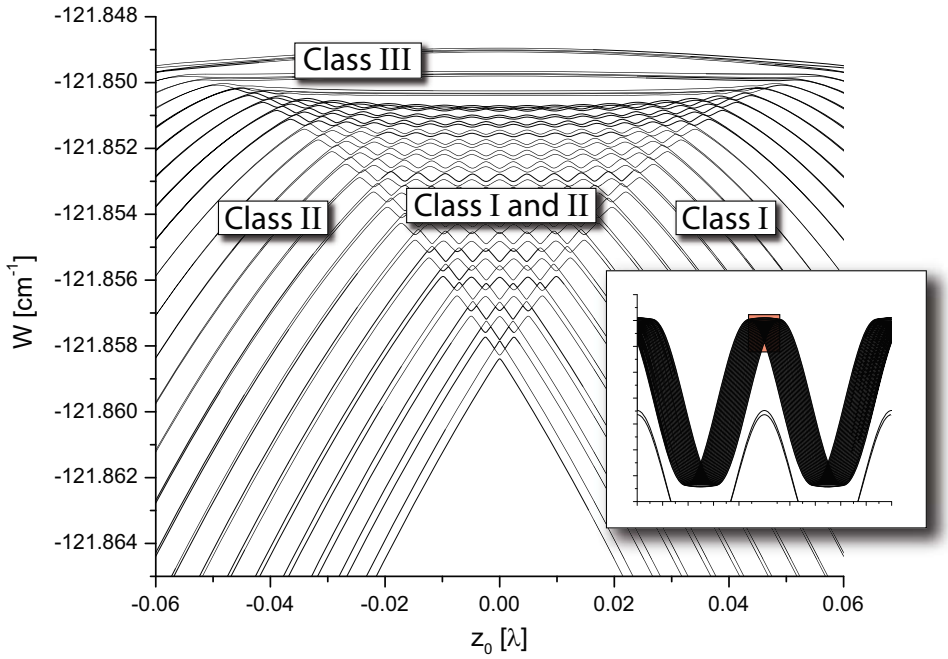

Figure 6.6: A closer look at the adiabatic potential for a $V_0 = 2$ GHz lattice with $n = 30$ and $m_j = 2.5$ reveals three classes of states. Class I consists of vibrational states with a positive dipole moment, class II consists of vibrational states with a negative dipole moment, and class III consists of rotational states.

and Figure 6.6 is compelling.

6.4 Conclusion and experimental possibilities

In the past three chapters, I have shown that the large size and high degree of degeneracy of Rydberg atoms leads to a number of interesting effects that govern their behavior in optical lattices. In this chapter, the adiabatic potential surfaces for Rydberg states in a ponderomotive optical lattice have been calculated. The structure of the potentials can be modeled via an effective electric field near the lattice inflection points and an effective magnetic field near the lattice nodes and anti-nodes. By restricting the available states to high m_j values, the n-range over which the models are applicable is increased due to a reduction of the extent of the Rydberg atom wave-function along the lattice laser beam direction. I have demonstrated how the perturbation at the anti-nodes of the lattice electric field resembles the

diamagnetic problem and gives rise to rotational and vibrational energy levels. I have shown the adiabatic wave-functions for some representative cases. The adiabatic potentials in this chapter could be measured spectroscopically in a ponderomotive optical lattice that is sufficiently deep, such that the individual potentials can be resolved. With the current experimental setup, trap depths of up to $\sim$ 50 MHz are possible, which is not enough to measure the effects described in this chapter. However, the future implementation of an in-vacuum concentric cavity within the CryoMOT experiment will drastically improve the depth of the lattice and would be an important step forward in visualizing the adiabatic potentials of the degenerate Rydberg atom states within a ponderomotive optical lattice.

CHAPTER VII

Future Directions

In the following, I discuss a few options for future endeavors in both the Blockade Experiment and the CryoMOT. These are just a few of the many projects we have discussed over the past five years but never had time to investigate.

7.1 Dual excitation in the Blockade Experiment

In the rotary echo experiment described in Chapter 3, the excitation region is approximately 1200 μm^3. For the case of strongest interactions at $n = 43$, this allowed for about three excitations ("bubbles"). If the excitation region were reduced in size such that only one excitation was allowed, while all others were blockaded, new effects would be visible. For example, I was not able to reach the regime of a perfectly blockaded system as theoretically studied in Ref. [37] with the current excitation scheme. Having a single excitation volume would also enable new studies of excitation statistics [31] and double resonance spectroscopy [30] without the decohering effects of multiple interacting excitations.

A natural extension of reducing the excitation region size is creating two separate excitation regions that can be individually addressed. A number of research groups have moved toward this type of dual excitation [24, 53]. This can be accomplished either by creating two excitation beams interacting with a single trap of atoms or by

creating two spatially separated traps.

For future experiments in the Blockade Experiment, I have constructed an excitation setup that generates two lower transition (780 nm) excitation beams using a birefringent calcite crystal. Beam displacers are formed from a plane parallel plate cut such that the optic axis is angled with respect to the front surface. Light with a polarization perpendicular to the optic axis will travel straight through the crystal without refraction, while light with a polarization parallel to the optic axis will travel at an angle through the crystal. At the exit of the crystal, the two beams will be parallel yet displaced from each other. The amount of displacement is determined by the length of the crystal and the angle of the optic axis with respect to the surface normal. As a side note, sometimes yttrium orthovanadate (YVO_4) is used instead of calcite in beam displacers. YVO_4 has better mechanical and optical properties, better temperature stability, a higher optical damage threshold, and a higher index of refraction (crystal size can be smaller for the same beam displacement). However, the transmission through YVO_4 is lower for most visible wavelengths and the crystal itself can be more expensive.

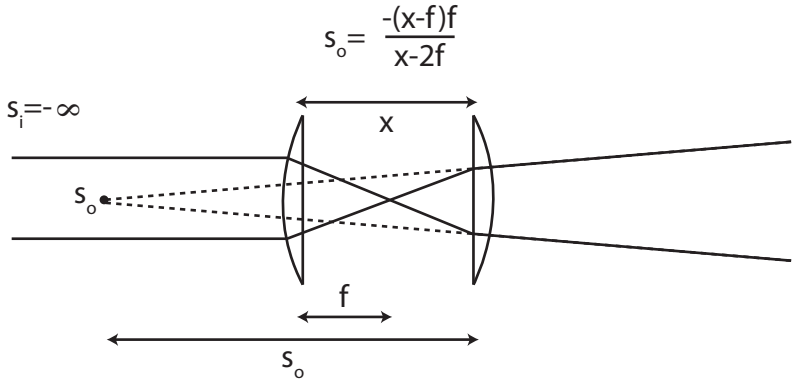

Figure 7.1: Initial telescope used to create a slightly divergent beam.

Here I outline the optical setup needed for two excitation spots with adjustable

separation. The complete setup involves two telescopes with the birefringent crystal situated between them. A final lens focuses the two spots into the vacuum chamber and onto the excitation region. In order to create two spatially separated focal spots in the excitation region, the beam entering the birefringent crystal must be slightly divergent. Otherwise, the final lens before the chamber will simply focus the two separated beams onto the same spot. Figure 7.1 shows the first telescope in the dual excitation setup. The lenses have the same focal length, f, and are separated by slightly more than $2f$. This telescope creates a virtual image behind the lens system located at $s_0 = \frac{-(x-f)f}{x-2f}$ where x is the distance between the two lenses.

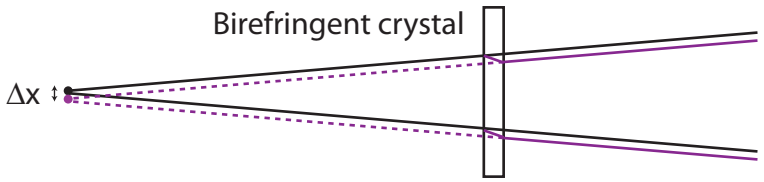

Figure 7.2: Birefringent calcite crystal used to separate the incident beam into two polarization components.

The effect of the birefringent crystal on a divergent beam is shown in Figure 7.2. Upon entering the crystal, the beam must be polarized such that the polarization components parallel and perpendicular to the optic axis of the crystal are evenly divided. In this case, half of the beam power is transmitted straight through the crystal while the other half is refracted at an angle defined by the angle of the optic axis. Tracing the beams backwards shows that the effect of the crystal is to create two beams with a spatially separated virtual focus of Δx. This separation is determined by the crystal properties (index of refraction, length, etc.) and is fixed. Usual beam separations are in the range 0.1-10 mm.

The last telescope serves to recollimate the two beams. Figure 7.3 shows how this is done. I have assumed here that the focal lengths of the two telescope lenses are the

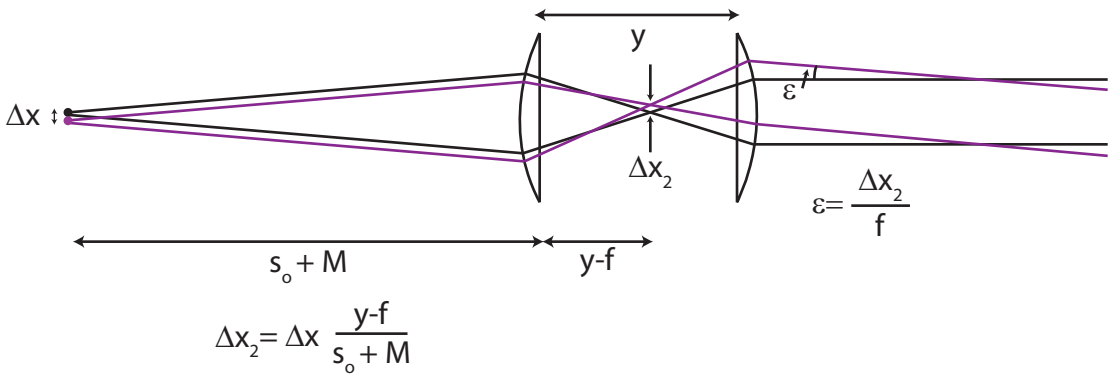

Figure 7.3: Recollimation of two spatially separated beams.

same and are equal to the focal lengths of the other telescope lenses, but this need not be the case. The two virtual beam sources are a distance $s_0 + M$ from the first lens where M takes into account the mounting distance of the birefringent crystal. The two beams will focus between the lenses with a separation of $\Delta x_2 = \Delta x \frac{y-f}{s_0+M}$. Here, y is the distance between the lenses and is slightly greater than $2f$, such that the exiting beams are collimated. The two collimated beams then travel with an angular separation of $\varepsilon = \Delta x_2 / f$.

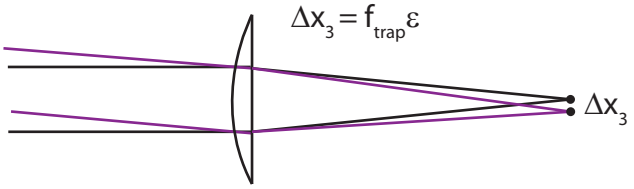

Figure 7.4: Focus of the two beams into the vacuum chamber.

The last part of the dual beam setup is shown in Figure 7.4. The last lens serves to focus the two beams into the vacuum chamber. The beam separation at the excitation region is $\Delta x_3 = f_{\text{trap}} \times \varepsilon$.

The complete optical setup is shown in Figure 7.5. The final focused beam separation can be adjusted by changing the distances x and y as shown in Figures 7.1 and 7.3. Using a CCD camera placed at the focus of the optical system, I measured

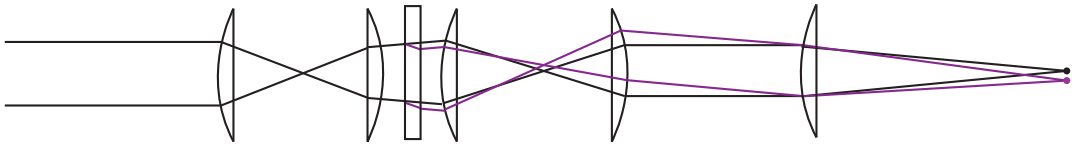

Figure 7.5: Complete optical setup for dual excitation beams.

a final beam separation of 17 μm for $f = 5$ cm and Δx=200 μm. By changing the distance between the first pair of lenses, this value can be adjusted from zero up to about 100 μm before the beam divergence becomes unmanageable. Figure 7.6 shows the intensity profile of the two beams overlayed with an approximate profile of the dipole trap. Ideally, the two beam widths would be slightly smaller to ensure only one excitation is allowed per beam. The best way to accomplish this would be to move the last lens of the optical system inside the chamber and closer to the excitation region.

The implementation of the setup described in this section would allow a number of new investigations into Rydberg atom interactions. For one, the rotary echo experiment described in Chapter 3 should exhibit much higher echo visibilities of one can reach the strongly blockaded regime where only one Rydberg excitation is allowed per excitation beam. To achieve this for $n = 43$, the widths of the 780 nm beams would have to be reduced to about 5 μm. By changing the polarization of the light entering the birefringent crystal, it would be easy to switch between a single excitation region and two nearby regions. Ref. [37] suggests that this would reduce the echo visibility due to interactions between pseudoparticles, whereas in Chapter 3 I have provided an alternate explanation that suggests the visibility would not be affected. Additionally, the double-resonance spectroscopy experiment I performed with Aaron Reinhard in the Raithel lab (Ref. [30]) could yield much clearer results

with a single excitation region, and would allow one to study how the Rydberg excitation ladder energy structure changes with distance between Rydberg atoms.

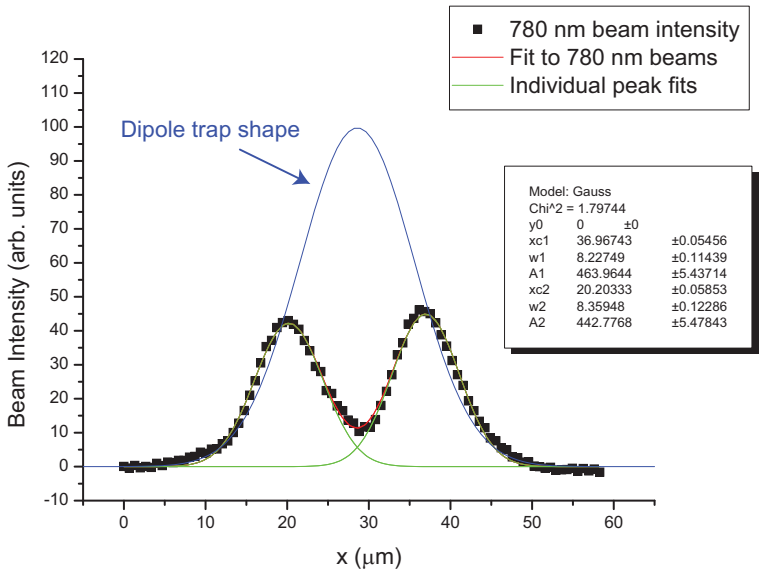

Figure 7.6: Intensity profile of two spatially separate excitation beams overlayed with a dipole trap profile. Fit parameters represent a fit to each individual peak.

7.2 Raman optical lattice in the CryoMOT experiment

There a number of applications that can be pursued with the optical lattice setup described in Chapter 4. Here I calculate the relevant parameters important in creating a Raman optical lattice, which is a slight modification of the current apparatus. This would be an excellent way to increase population transfer into the Rydberg state over the traditional excitation method. Injecting atoms into the lattice in this manner would be applicable in quantum information processing schemes where it is important to fill lattice sites as evenly as possible. In this case, as opposed to applying 1064 nm radiation, one of the excitation beams is used to form the lattice instead.

A classical Raman transition refers to a Λ-system where there are two long-lived

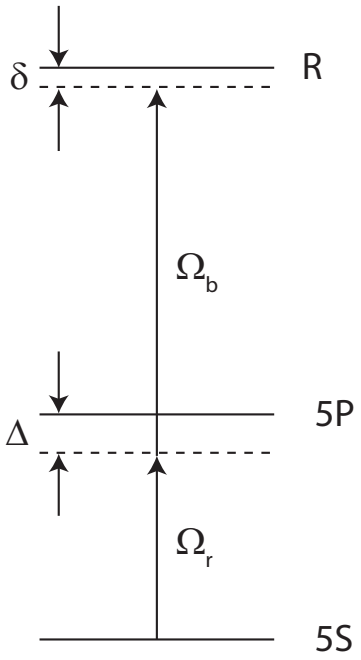

Figure 7.7: Excitation scheme for Raman optical lattice.

ground states and one excited state. Population is coherently transferred between the ground states via an excited state that is detuned from resonance. In this case, the two long-lived states are the ground 5S state and the Rydberg state. This is loosely termed a Raman transition because the Rydberg state has a very long lifetime ($\sim$100 μs) compared the to the lifetime of the 5P state (27 ns).

The two-photon Rabi frequency for the transition from the 5S state to the Rydberg state is given by,

$$\Omega_{\mathrm{RAM}} = \frac{\Omega_R \Omega_B}{2\Delta} \tag{7.1}$$

For an intermediate detuning of $\Delta = 1$ GHz and Rabi frequencies of $2\pi \times 50$ MHz on both transitions, this leads to a two-photon Rabi frequency of $2\pi \times 1.25$ MHz.

To create an optical lattice, one of the excitation beams is a standing wave such that the Rabi frequency is modulated in space. The depth of the lattice is given by,

$$V = \frac{\Omega_{\mathrm{RAM}}^2}{2\delta} \tag{7.2}$$

For a Rydberg state detuning of $\delta = 2\pi \times 5$ MHz, the trap depth is $2\pi \times 156$ kHz. The corresponding temperature is $T = h\nu/k_b = 7.5\mu K$, which points out the fact that cooling below the Doppler limit of 140 μK would be necessary to keep the atoms confined. The trap potential takes the form $V \sim V_0 \cos 2kz \sim V_0 \left(1 - \frac{4k^2z^2}{2}\right)$ where the bottom of the lattice has been approximated as a harmonic potential. The force constant, F, is then $F = V_0\,(4k^2)$. The oscillation frequency in such a harmonic potential is given by, $\Omega = \sqrt{\frac{F}{m}} = 2\pi \times 3.5\mu$s.

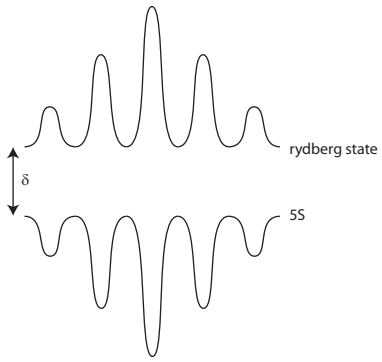

Figure 7.8: Dressed state picture for Raman optical lattice.

The lattice energy levels in the dressed state picture are shown in Figure 7.8. The nodes of the lattice are the points where the blue Rabi frequency is zero, and the antinodes are the points where the Rabi frequency is maximized. When the blue Rabi frequency is zero, the lower and upper states are pure 5S and Rydberg, respectively. When the Rabi frequency is at its maximum, the states are coherently mixed as,

$$\psi_+ = \frac{1}{\sqrt{2}}\left(|5S\rangle + e^{i\phi}|R\rangle\right) \tag{7.3}$$

$$\psi_- = \frac{1}{\sqrt{2}}\left(|5S\rangle - e^{i\phi}|R\rangle\right) \tag{7.4}$$

The atoms will be in the 5S ground state when the lattice is off. The quantum adiabatic theorem states that a system remains in its instantaneous eigenstate a long

as a given perturbation acts slowly enough (is adiabatic) and there is a gap between its eigenvalue and the rest of the spectrum. Therefore, a slow turn on of the optical lattice will cause the atoms to settle on the lower adiabatic potential. Slow in this case means slow compared to the relevant Rabi frequencies and detunings. This means that the turn on time must be at least 1 μs, however, there are some upper limits to the speed at which the lattice can be turned on.

The scattering rate out of the 5P state limits the coherence time of the lattice. This rate is given by,

$$\tau_{\text{scatter}} = \frac{\Gamma}{2}\frac{\Omega_r^2}{4\Delta^2} \tag{7.5}$$

where Γ is the linewidth of the transition, and $\frac{\Omega_b^2}{4\Delta}$ is the light-shifted energy of the 5P state. For a linewidth of $2\pi \times 6$ MHz, the scattering rate is one photon every 85 μs. The lifetime also limits the coherence time of the lattice. Typical lifetimes for Rydberg S states around $n = 50$ are 100 μs.

With the current experimental apparatus in the CryoMOT, there would be minimal modifications necessary needed to create a Raman optical lattice. Additionally, adiabatic transfer into the current 1064 nm lattice could also be achieved by sweeping and electric field across the resonance. The microwave spectroscopy technique used in Chapters 4 and 5 would provide a method of determining the transfer efficiency into the lattice as well as the trapping lifetime.

7.3 Goodbye and good luck

In this thesis, I have examined interactions between cold Rydberg atoms, primarily within the context of quantum information. The DiVincenzo requirements for quantum computing as first listed in Chapter 1 are scalability, qubit initialization, gates faster than the decoherence time of the system, the ability to read out a result

at the end of the gate, and a universal gate set. Here, I have addressed the first four of these requirements. In Chapter 3, I described a unique method for determining coherence in Rydberg atom excitation with the use of a rotary echo technique. This method is ideal for larger ensembles of atoms where the more traditional method of measuring Rabi oscillations is not possible. This rotary echo technique can be used to test the effect of many sample parameters on coherence time, including atom-atom interaction strength, atom density, and atom temperature. The technique is an excellent method for determining the maximum gate time that can be used in order to maintain the required gate fidelity. The experiment described in Chapter 3 was the first to measure rotary echo signals in an atom sample with a temperature as high as 1 mK. I also provided a new interpretation of how the coherence time of the system depends the interaction strength between Rydberg atoms.

In Chapters 4, 5, and 6, I discussed a method to build and uses for a ponderomotive optical lattice for Rydberg atoms. This was the first demonstration of the existence of a ponderomotive optical lattice for Rydberg atoms. Trapping Rydberg atoms in optical lattices has applications in a wealth of research fields, including high precision spectroscopy, dipole-forbidden transitions, purely quantum mechanical effects, as well as quantum information. When Rydberg atoms are trapped in a lattice structure, they exhibit long storage times, reduced collision rates, and minimal trap-induced shifts. This is ideal for scaling up quantum computation registers to include multiple qubits. It also allows for qubit initialization and readout, since lattice sites can be individually addressed with tightly focused laser beams.

In Chapter 7, I have discussed a few possible future endeavors for the Blockade Experiment and the CryoMOT, yet there seems to be such a number of ideas floating around at the moment that I have barely grazed the surface. I wish the future

students who take on these projects the best of luck, and hope that they have as much fun as I did, but with fewer floods and electrocutions. One last piece of advice, if someone asks you a question about your project and you don't know the answer, say this:

> "At this stage there is essentially the question of an influence on the very conditions which define the possible types of predictions regarding the future behavior of the system." *Niels Bohr*

APPENDICES

APPENDIX A

Atomic Units

Atomic units are one of the most useful simplifications made in atomic physics. Here I will give a brief summary.

In atomic units, the rest mass of the electron (m_e), the electron charge (e), Planck's constant (reduced) ($\hbar$), and the Coulomb force constant ($1/4\pi\epsilon_0$) are all set to one. You will have to multiply by the SI value of these constants to convert a number given to you in atomic units into SI units. For example, if you have a mass $m = 100$ a.u., this is equal to $100 \times 9.109 \times 10^{-31}$ kg. The values for the fundamental atomic units are shown Table A.1.

Symbol	SI value
m_e	$9.10938215(45)\times10^{-31}$ kg
e	$1.602176487(40)\times10^{-19}$ C
$\hbar$	$1.054571628(53)\times10^{-34}$ J·s
$1/4\pi\epsilon_0$	$8.9875517873681\times10^{9}$ kg·m^3·s^{-2}·C^{-2}

Table A.1: Fundamental atomic units.

Perhaps the best way to remember what constants you need to multiply is to memorize the units of each of values shown in Table A.1. Additionally, there are many derived units that are combinations of the values given in Table A.1 and a few other fundamental constants such as the Bohr radius and the Hartree. The must useful conversions for understanding the topics in this thesis are given in Table A.2.

Name and Symbol	Fundamental constants	SI value
Length (Bohr radius, a_0)	$4\pi\epsilon_0\hbar^2/\left(m_e e^2\right)$	$5.2917720859(36) \times 10^{-10}$ m
Energy (Hartree, E_h)	$m_e e^4/\left(4\pi\epsilon_0\hbar\right)^2$	$4.35974394(22)\times10^{-18}$ J
Electric field	$E_h/\left(ea_0\right)$	$5.14220632(13)\times10^{11}$ V·m^{-1}

Table A.2: Derived atomic units.

To illustrate the use of these units, I provide a couple of different examples below.

A.1 Interaction Energy $\mathrm{V_{int}}$

The dipole-dipole interaction energy is written as $\mathrm{V_{int}}$=n^{*4}/R^3 in this thesis. See that this is written in units of inverse length cubed. To convert this value into Joules, multiply by the Bohr radius cubed and then the Hartree, which is equivalent to multiplying by $e^2a_0^2/4\pi\epsilon_0$. Explicitly, for a Rubidium Rydberg state,

$$\mathrm{V_{int}} = \mathrm{n^{*4}/R^3} \rightarrow \frac{\mathrm{n^{*4}}}{\mathrm{R^3}} \times \frac{\mathrm{e^2 a_0^2}}{4\pi\epsilon_0} \tag{A.1}$$

For the state $50\mathrm{D}_{5/2}$ at a separation of 1 μm,

$$\mathrm{V_{int}} = \frac{0.36\sqrt{2}\left(50-1.34\right)^4}{\left(10^{-6}\mathrm{m}\right)^3} \times \frac{\left(1.6\times10^{-19}\ \mathrm{C}\right)^2\left(0.529\times10^{-10}\ \mathrm{m}\right)^2}{4\pi\left(8.85\times10^{-12}\ \mathrm{kg^{-1}\cdot m^{-3}\cdot s^{-2}\cdot C^2}\right)} \tag{A.2}$$

$$= 1.84\times10^{-24}\ \mathrm{J} \tag{A.3}$$

$$= 2.77\ \mathrm{GHz} \tag{A.4}$$

where in the last step I divided by h to convert to GHz, which is often a more useful representation than Joules. The $0.36\sqrt{2}$ factor is particular to this case. The exact factor may be different for other Rydberg states. The angular momentum D states couples symmetrically to two states: a P and an F state, resulting in the $\sqrt{2}$ factor. The 0.36 is a result of the wavefunction overlap of the states.

A.2 Ionization electric field

The electric field at which a Rydberg state ionizes is typically $E = \frac{1}{16n^{*4}}$. To convert this into SI units, simply multiply by the derived electric field unit shown in Table A.2. For $50D_{5/2}$,

$$E = \frac{1}{16\left(50 - 1.34\right)^4} \times 5.14 \times 10^{11} \text{ V/m} \tag{A.5}$$

$$= 57.3 \text{ V/cm}. \tag{A.6}$$

APPENDIX B

Scalar, Tensor, and Dynamic Polarizabilities of Atoms

The polarizability of an atomic state describes how the atom responds to an electric field. Scalar and tensor polarizabilities arise from static electric fields, while the dynamic polarizability is the result of an oscillating electric field and is frequency dependent.

B.1 Scalar and Tensor Polarizabilities

The polarizability of an atom represents the amount of charge separation that occurs when the atom is placed in an external field. The polarizability is related to the external electric field $\mathbf{E}$ via

$$\mathbf{p} = \alpha \cdot \mathbf{E}. \tag{B.1}$$

Consider the energy of an induced dipole in an electric field. Inducing a dipole moment will affect the energy of the atom and will therefore determine how the atom acts in the external field. We can relate the change in the energy of the atom to the polarizability by looking at the amount of work done on the atom by the external field. The work done on the induced dipole in changing the electric field from $\mathbf{E}$ to $\mathbf{E} + d\mathbf{E}$ is

$$dW = -\mathbf{p} \cdot d\mathbf{E} = -\mathbf{E} \cdot \alpha \cdot d\mathbf{E}. \tag{B.2}$$

We can integrate this equation to find the total work is simply

$$W = -\frac{1}{2}\mathbf{E} \cdot \alpha \cdot \mathbf{E}. \tag{B.3}$$

An interesting fact is that the polarizability of all atoms in their ground state is positive for static fields, which means that the energy of a ground state atom is always lowered by the presence of the external field. This is simply an illustration of the fact that while in the ground state, the atom can only couple to higher-lying states.

If the polarizability is isotropic, then equation B.3 reduces to $W = -\frac{1}{2}\alpha E^2$ where the polarizability α can now be represented by a single number since it is a scalar. This is just the familiar Stark shift of an electron placed in an external field. However, the polarizability is only isotropic for an atom that has zero total angular momentum ($J = 0$). If $J \neq 0$, then the induced dipole moment will depend on the spin polarization of the atoms and will be anisotropic. In this case, the polarization is still proportional to the external field, but the direction of the induced dipole moment may not be the same as the direction of the applied field. In this case we need a polarizability tensor, to describe the dipole moment induced in the atom.

The Hamiltonian describing the effect of an electric field $\mathbf{E}$ on an atom is given by [83]

$$H = -\left(\alpha_0 + \alpha_2 \frac{3J_z^2 - \mathbf{J}^2}{J\left(2J-1\right)}\right)\frac{E^2}{2} \tag{B.4}$$

where $\mathbf{J}$ is the angular momentum of the electron and the quantization axis z is parallel to the direction of the electric field. The second term is the tensor polarizability and only exists for $J \neq 0$, as described above. The terms α_0 and α_2 are the

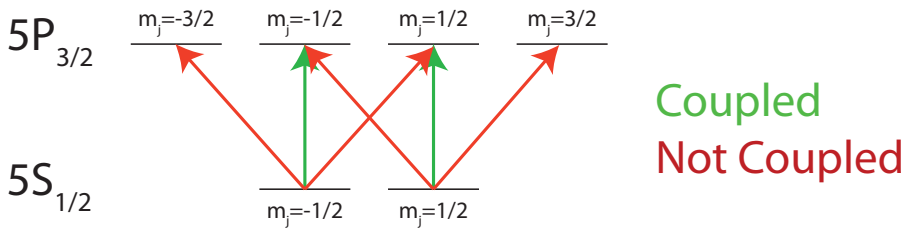

Figure B.1: Coupling between the $5S_{1/2}$ state and the $5P_{3/2}$ state due to a static electric field.

scalar and tensor polarizabilities respectively, and are defined by

$$\alpha_0 = \frac{r_0}{4\pi^2} \sum_{J'} \lambda_{JJ'}^2 f_{JJ'} \tag{B.5}$$

$$\alpha_2 = \frac{r_0}{8\pi^2} \frac{1}{(2J+3)(J+1)} \sum_{J'} \lambda_{JJ'}^2 f_{JJ'} \left[8J(J+1) - 3X(X+1)\right] \tag{B.6}$$

where $X = J'(J'+1) - 2 - J(J+1)$, r_0 is the classical electron radius, $\lambda_{JJ'}$ is the wavelength for a transition between states J and J' and $f_{JJ'}$ is the transition oscillator strength [84].

As an example, a $P_{3/2}$ state has $J = 3/2$, $\mathbf{J}^2 = 3/2\,[3/2+1] = 15/4$, and $J_z = 3/2$ or $1/2$. The tensor part of the Hamiltonian is then $H_{\text{tens}} = \alpha_2 \frac{E^2}{2}$ for $J_z = 1/2$ and $H_{\text{tens}} = -\alpha_2 \frac{E^2}{2}$ for $J_z = 3/2$. Because the scalar and tensor polarizabilities are a result of a linear field, the couplings between different states that contribute to the sum in equation B.4 are limited. For example, the $5S_{1/2}$ state does not couple to the $5P_{3/2,|m_j|=3/2}$ state, as shown in Figure B.1. The shift of this state is thus entirely due to higher lying states with angular momentum $J > 1/2$.

B.2 Dynamic Polarizability

The dynamic polarizability is the result of an atom being placed in an oscillating electric field (like an electro-magnetic wave). This construction is parallel to the AC stark shift or light shift of atomic energy levels. There are three main differences between the static polarizability and the dynamic polarizability: the tensor polariz-

ability can contain an antisymmetric part, the atom can absorb and emit photons from the field so the polarizability tensor consists of both a dispersive part and an absorptive part, and the polarizability depends on the frequency of the light inducing the dipole moment [85]. It is the dynamic polarizabilities of the different levels of Rb that allow the formation of the optical dipole traps and optical lattices described in this thesis.

B.3 Dynamic Polarizabilities: On Resonant Dipole Trap Spectra

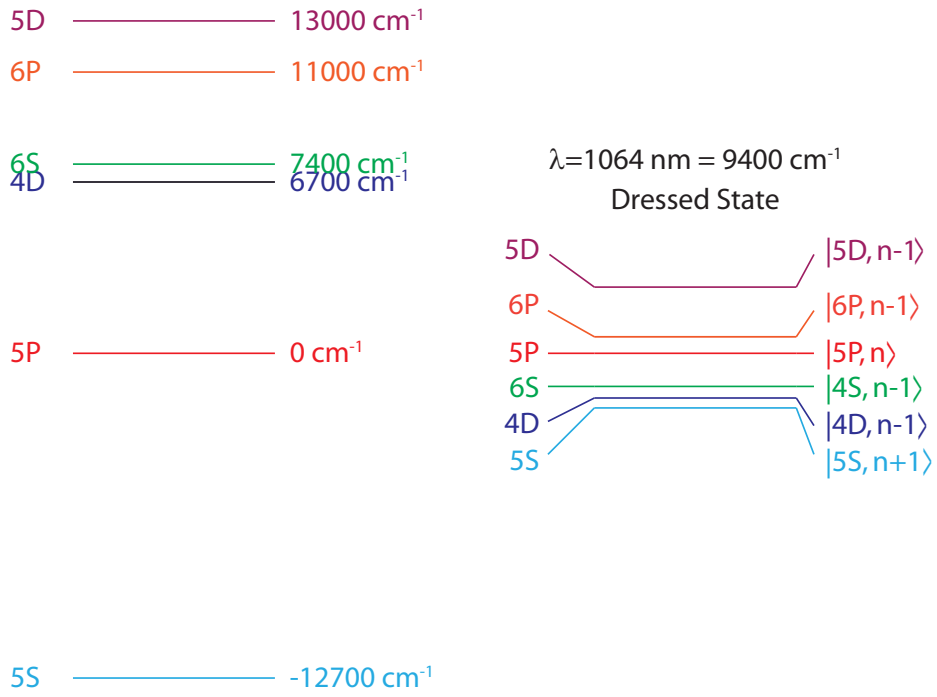

Figure B.2: Energy levels near the 5S-5P transition in Rubidium (left). Dressed state energy levels with a 1064 nm field (right).

Here I provide a qualitative discussion of the effect of the dipole trap light on the 5S and 5P atomic states in Rubidium. This is an alternative view to that discussed in Section 2.3. Though off-resonant, the 1064 nm laser light initiates couplings between the various states of our atoms via a dynamic polarizability as discussed above. These couplings will generate light shifts of the energy levels and create a potential well

into which atoms are attracted. To determine the exact light shifts of the 5S and 5P levels of Rubidium in a 1064 nm field, the sum of the couplings to all other states must be calculated. It is easiest to consider the situation in the dressed state picture. The relevant unperturbed energy levels are shown on the left in Figure B.2. On the right are the energy levels in the dressed state basis where one photon has been added or subtracted from the field. Here, 5P is taken as the reference, zero-energy point. Energies are written in wavenumbers (cm^{-1}). The photon from the field is 1064 nm or 9400 cm^{-1}.

The 5S state couples strongly only to the 5P state. The next dipole coupled state is the 6P state which lies more than two photons away (11000 cm^{-1}+12700 cm^{-1}=23700 cm^{-1}). Consider the Hamiltonian of the interaction between the 5S and 5P states:

$$H = \begin{pmatrix} E & \chi \\ \chi & 0 \end{pmatrix}$$

where the energy of the 5P state is the reference energy 0, and the energy of the 5S state is E. The coupling between the state is denoted as χ. The eigenvalues of the system are,

$$\lambda_+ = \frac{-\chi^2}{E} \tag{B.7}$$

$$\lambda_- = E + \frac{\chi^2}{E} \tag{B.8}$$

where λ_+ and λ_- are the perturbed energy levels of the 5P and 5S states, respectively. Since the energy value E is negative in this case (see Fig. B.2), the 5P state shifts up in energy due to the interaction with 5S, and the 5S state shifts down in energy due to the interaction with 5P. The shifts are equal in magnitude.

The light shift for 5S is equal to $\frac{1}{2}\alpha_{5\mathrm{S}}E^2$ where $\alpha_{5\mathrm{S}}$ is the dynamic polarizability of the 5S state. In the classical electron oscillator model, the polarizability is calculated

via

$$\alpha = -\frac{e^2}{m\omega^2}\frac{1}{\omega^2 - \omega_0^2} \tag{B.9}$$

where ω is equal to $2\pi c/1064$ nm and ω_0 is an atomic resonance. Using only the strong resonance from 5S to 5P at 780 nm to calculate α, we find a value of $\alpha_{5S} = 1.573 \times 10^{-7} \frac{\text{cm}^2}{\text{V}^2}$MHz. Since there are no other strong couplings for the 5S state, calculating just the shift from the 5P state provides an estimation accurate to within about 10 percent. A more accurate determination is provided in Ref [86] and is equal to $1.776 \times 10^{-7} \frac{\text{cm}^2}{\text{V}^2}$MHz.

It is more difficult to find an estimate of the 5P dynamic polarizability, and, to my knowledge, has not been experimentally measured to date. From Figure B.2, it is clear that there are a number of resonances that contribute to the light shift (6S and 4D will push the state upwards in energy while 5D will depress the energy). We can find an estimation of the dynamic polarizability of 5P by looking at spectra of Rydberg atom excitation in an optical lattice. Note that in contrast to the spectra shown in Chapter 4, for these cases the trap is excited with the lower transition 780 nm laser approximately on resonance with atoms that are located at the bottom of the dipole trap. This is opposed to the 1.2 GHz detuning used for the experiments in Chapter 4.

Spectra of the dipole trap excited on resonance show three distinct features. In figure B.3, the peak on the far left corresponds to atoms not in the trap, being off-resonantly excited by the 5S-5P light, combined with a 480 nm photon at the right frequency. The peak in the middle corresponds to atoms at the bottom of the trap, being resonantly excited by 5S-5P light combined with a 480 nm photon. Lastly, the peak on the far right corresponds to atoms not in the trap, being resonantly excited by primary MOT light and a 480 nm photon. The primary MOT light is 5 MHz red

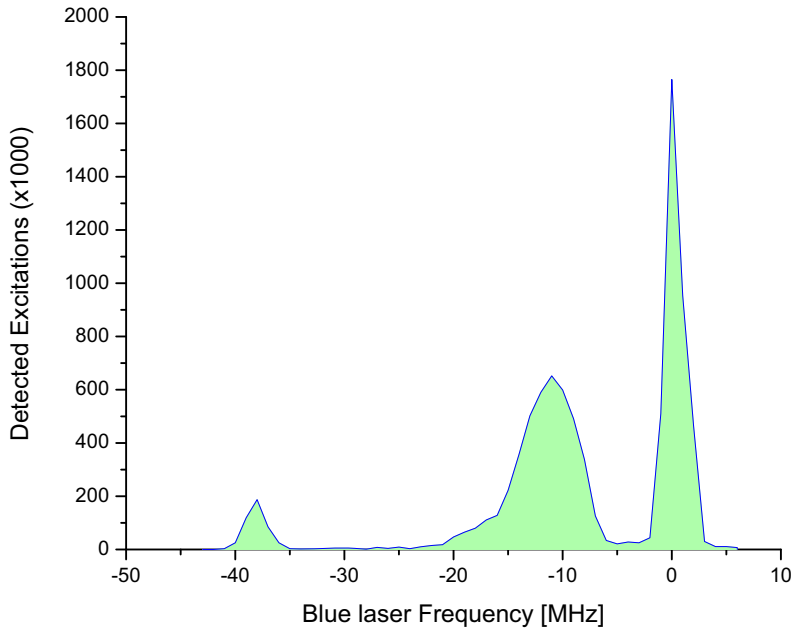

Figure B.3: Excitations as a function of blue laser frequency. The lower transition light is approximately on resonance with atoms at the bottom of the dipole trap.

detuned of the 5S-5P transition resonance, so this peak is slightly shifted to the right in the spectra, since a higher energy blue photon is required for excitation. As a side note, the primary MOT light leaks into the secondary MOT chamber through the pyramidal MOT (see Section 2.5). It is usually not desirable that this light would overlap with the excitation region, but in this case serves as a convenient frequency marker that does not depend on the intensity of the dipole trap light or the frequency of the 5S-5P excitation laser light. By measuring the distance between this peak and the peak on the far left, the detuning of the 5S-5P laser can be easily measured.

Figure B.4 shows how the three peaks in Figure B.3 are excited. As the red frequency is scanned (arrows (2) and (3)) in Figure B.4) the peaks will shift. There is a narrow frequency region where atoms in the dipole trap will be resonantly excited. At all other frequencies, both atoms in the trap and atoms outside of the trap are

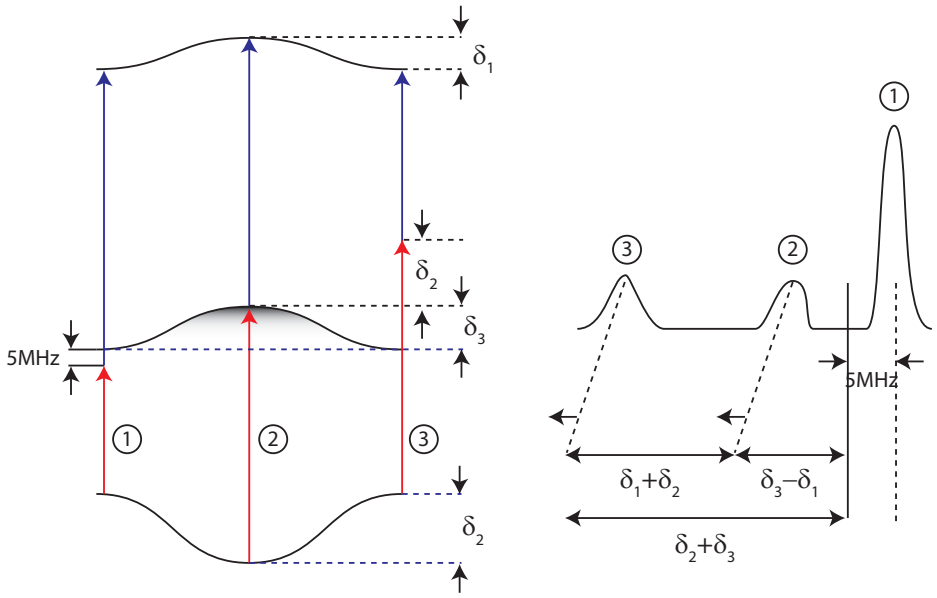

Figure B.4: Origin of the three different peaks in the dipole trap spectra.

excited off-resonantly.

Figure B.5 shows many different spectra for different 5S-5P laser frequencies. As previously mentioned, the detuning of this laser from the MOT transition can be determined by measuring the distance between the far left and right peaks in the spectra. The peak corresponding to the dipole trap does not appear until a detuning of about 30 MHz has been reached. The maximum height of the peak occurs at a detuning of 36 MHz. The relative shift of atoms inside and outside of the trap appears approximately linear. This is expected if atoms are being excited off resonantly, and most atoms in the dipole trap are at the very bottom of the trap. This is confirmed from off-resonant dipole trap spectra as shown in Figure B.6, where the intermediate 5S to 5P transition is detuned by 1.2 GHz. From this spectrum, most atoms are located at a depth of about 25 MHz. By examining Figures B.4 and B.5, and by using the dynamic polarizabilities of the 5S and Rydberg state ($1.776 \times 10^{-7} \frac{\text{cm}^2}{\text{V}^2}$MHz and $-1.354 \times 10^{-7} \frac{\text{cm}^2}{\text{V}^2}$MHz, respectively), we can determine the values of δ_1, δ_2, and δ_3 from Figure B.4. This allows us to estimate the 5P polarizability to be

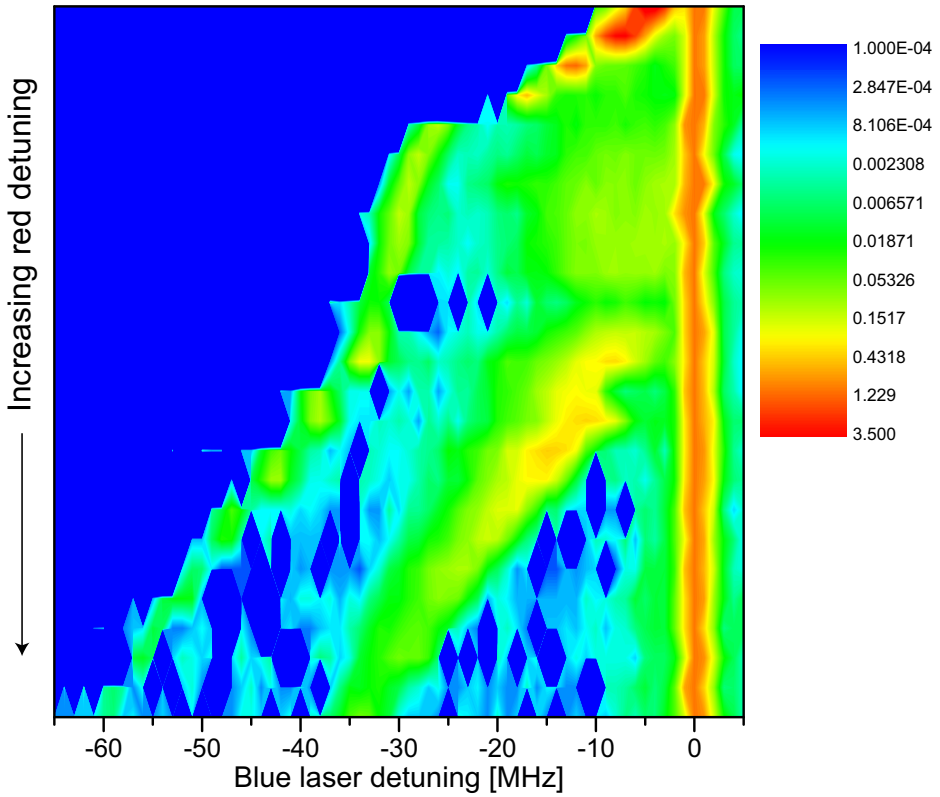

Figure B.5: Dipole trap spectra as the 5S-5P laser is scanned in frequency.

$\sim -1.9 \times 10^{-7} \frac{\mathrm{cm}^2}{\mathrm{V}^2}$MHz. This value is consistent with the discussion above.

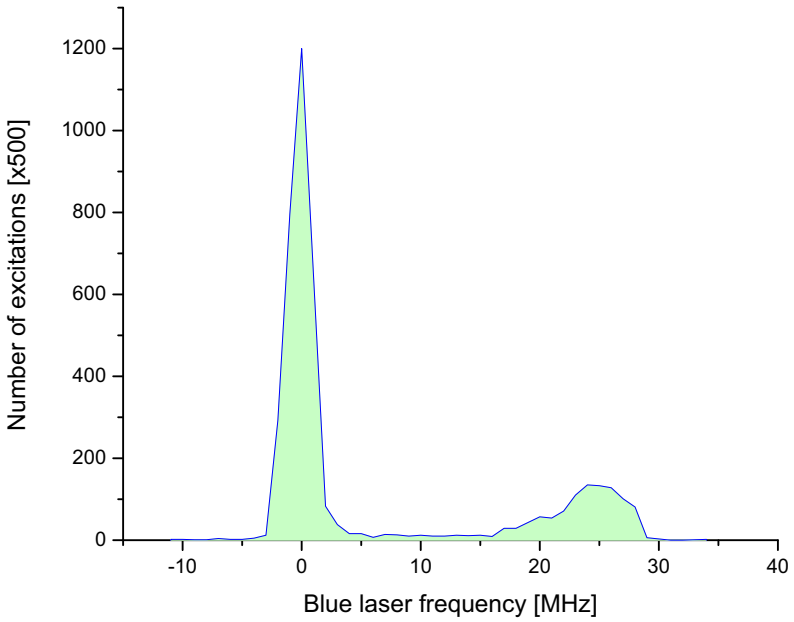

Figure B.6: Spectrum of atoms in and out of the dipole trap with a 1 GHz detuning on the intermediate transition.

APPENDIX C

Phase Matching in a Frequency-Doubled Laser

In order for the non-linear crystals inside of frequency doubled lasers to be effective at producing doubled light, the wavevectors of the two colors (960 nm and 480 nm in the case of this thesis) much match. This is known as phase matching. In general, the difference between the wavevectors is not zero because the index of refraction of a material depends on the frequency of the pump field. Ensuring Δk is zero is the same as matching the indices of refraction, since:

$$\Delta k = k^{(2\omega)} - 2k^{(\omega)} = \frac{2\omega}{c}(n^{2\omega} - n^{\omega}) \tag{C.1}$$

If one does not phase match, the second-harmonic wave generated at some plane z_1 having propagated to some other plane z_2, is not in phase with the second-harmonic wave generated at z_2, and there is interference. Two adjacent peaks of this interference pattern are separated by the "coherence length" $\frac{2\pi}{\Delta k}$, which gives the maximum crystal length that is useful in producing the second-harmonic power.

One way to phase match is to use waves of different types (extraordinary and ordinary) as the ω and 2ω beams. The index of refraction for the ordinary beam is the same no matter what angle it has with respect to the axis of the crystal, but the index for the extraordinary beam can be adjusted. The index is given by

$$\frac{1}{n_e^2(\theta)} = \frac{\cos^2\theta}{n_o^2} + \frac{\sin^2\theta}{n_e^2} \tag{C.2}$$

If θ is chosen correctly, the two indices can be matched, as shown in Figure C.1.

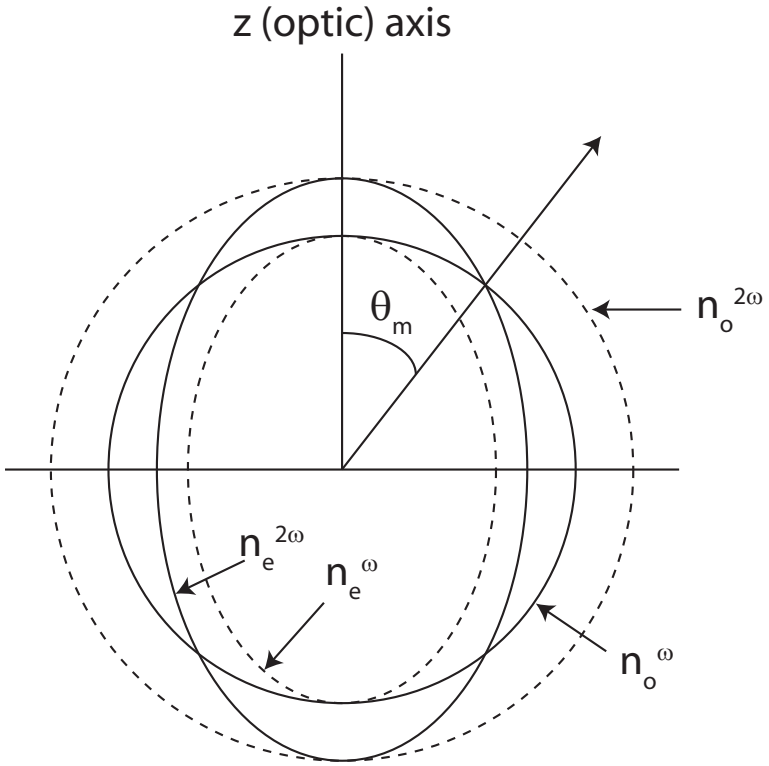

Figure C.1: Normal (index) surfaces for the ordinary and extraordinary rays in a negative ($n_e < n_0$) uniaxial crystal.

In this case, θ_m is given by

$$\frac{\cos^2\theta_m}{(n_o^{2\omega})^2} + \frac{\sin^2\theta_m}{(n_e^{\omega})^2} = \frac{1}{(n_o^{\omega})^2} \tag{C.3}$$

Solving for θ_m gives

$$\sin^2\theta_m = \frac{(n_o^{\omega})^{-2} - (n_o^{2\omega})^{-2}}{(n_e^{2\omega})^{-2} - (n_o^{\omega})^{-2}} \tag{C.4}$$

This method of phase matching is known as critical phase matching because a small change in the angle θ_m can change the phase matching by a large amount. Non-critical phase matching, or ninety-degree phase matching, is sometimes a better method. In this case, $\theta_m = 90\,^\circ$. It is seen from Figure C.1 that this is the flattest part of the ellipse for $n_e^{2\omega}$, and so a small change in angle does not change the phase matching condition very much. If this technique is used, the value of $n_e^{2\omega}$ must be

adjusted by changing the temperature of the crystal. In this way, Poynting vector walk-off is avoided, and the crystal angle does not have to be adjusted to phase match, which could cause the cavity to lose mode matching.

APPENDIX D

Calculating the Fourier transform limit of an optical pulse

When applying an excitation pulse (optical, microwave, etc) to a system, it is useful to calculate the Fourier transform limit of the pulse that you apply in order to get an estimate of the frequency bandwidth of your excitation. It is a reasonable assumption that the full width of the Fourier transform of an excitation pulse is the inverse of the temporal pulse width (i.e. $1/T$), however, this is only true for a Gaussian shaped pulse. If instead one has a square pulse, which is often a closer approximation for moderate pulse lengths, our Fourier transform is instead a sinc function and the full width is less clear. This example shows how to deal with such a case.

If one has a system where there are two coupled levels with amplitudes c_0 and c_1, detuning Δ, and coupling χ, the Hamiltonian in the rotating wave approximation (dressed state picture) is given by

$$H = \hbar \begin{pmatrix} 0 & \chi \\ \chi & \Delta \end{pmatrix} \tag{D.1}$$

and the Schrödinger equation yields

$$i\hbar \begin{pmatrix} \dot{c}_0 \\ \dot{c}_1 \end{pmatrix} = \hbar \begin{pmatrix} 0 & \chi \\ \chi & \Delta \end{pmatrix} \begin{pmatrix} c_0 \\ c_1 \end{pmatrix}. \tag{D.2}$$

In the limit of low saturation, set $c_0 = 1$ to find that

$$\dot{c}_1 + i\Delta c_1 = -i\chi. \tag{D.3}$$

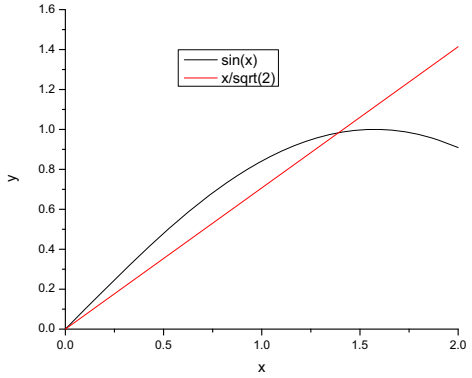

Figure D.1: Plot of $y = \sin x$ and $y = x/\sqrt{(2)}$.

The solution of such a differential equation has a homogeneous part and an inhomogeneous part. The homogeneous part has the solution $c_1 = ce^{i\omega t}$. Plugging this into Equation D.3 results in $i\omega ce^{i\omega t} + i\Delta ce^{i\omega t} = 0$. This shows that $\Delta = \omega$ and our final homogeneous solution is $c_1 = ce^{i\Delta t}$.

The inhomogeneous part is found by setting $\dot{c}_1 = 0$. In this case, $c_1 = -\chi/\Delta$.

Adding the two parts, our complete solution is $c_1(t) = ce^{i\Delta t} - \chi/\Delta$.

If $c_1(0) = 0$, then the constant c is equal to χ/Δ and the solution becomes

$$c_1(t) = \frac{\chi}{\Delta}\left(1 - e^{-i\Delta t}\right). \tag{D.4}$$

The population of the excited state c_1 is

$$c_1 c_1^* = \left(\frac{\chi}{\Delta}\right)^2 (2 - 2\cos\Delta T). \tag{D.5}$$

A quick check at this point to see if the calculation is correct can be performed by setting $\Delta = 0$. This gives $c_1 c_1^* = \chi^2 T^2$ which is what one would expect for zero detuning. The half-width can be found by setting

$$\frac{c_1 c_1^*}{\chi^2 T^2} = \frac{2}{\Delta^2 T^2}(1 - \cos\Delta T) = \frac{1}{2}. \tag{D.6}$$

Using the identity $(1 - \cos(2u))/2 = \sin^2 u$, Equation D.6 results in the transcendental equation

$$\sin x = x/\sqrt{2} \tag{D.7}$$

where $x = \Delta T/2$. This can be solved using any numerical method of preference. Figure D.1 shows a graph of the two intersecting curves. The graph shows that $x = 1.39$ or $\Delta = 2.78/T$. This is the half-width at half maximum. The full width in frequency units is then

$$\Delta = \frac{2 \times 2.78}{2\pi T} = \frac{0.88}{T}. \tag{D.8}$$

For example, if the pulse length is 7 μs (as in the microwave pulse used in Chapter 4), then $\Delta = 126$ kHz.

BIBLIOGRAPHY

BIBLIOGRAPHY

[1] D. Jaksch, J. I. Cirac, P. Zoller, S. L. Rolston, R. Côté, and M. D. Lukin. Fast quantum gates for neutral atoms. *Phys. Rev. Lett.*, 85:2208–2211, 2000.

[2] M. D. Lukin, M. Fleischhauer, R. Cote, L. M. Duan, D. Jaksch, J. I. Cirac, and P. Zoller. Dipole blockade and quantum information processing in mesoscopic atomic ensembles. *Phys. Rev. Lett.*, 87:037901, 2001.

[3] Vera Bendkowsky, Bjrn Butscher, Johannes Nipper, James P. Shaffer, Robert Lw, and Tilman Pfau. Observation of ultralong-range rydberg molecules. *Nature*, 458:1005–1008, 2009.

[4] C. Vadla, V. Horvatic, and K. Niemax. Line-broadening studies of excited diatomic homoatomic and heteroatomic rydberg molecules formed by potassium, rubidium, and cesium atoms. *Phys. Rev. A*, 80:052506, 2009.

[5] I. Lesanovsky, M. Mller, and P. Zoller. Trap-assisted creation of giant molecules and rydberg-mediated coherent charge transfer in a penning trap. *Phys. Rev. A*, 79:010701(R), 2009.

[6] H. H. Fielding. Rydberg wavepackets in molecules: From observation to control. *Annu. Rev. Phys. Chem.*, 56:91–117, 2005.

[7] Wenhui Li, Michael W. Noel, Michael P. Robinson, Paul J. Tanner, and Thomas F. Gallagher. Evolution dynamics of a dense frozen rydberg gas to plasma. *Phys. Rev. A*, 70:042713, 2004.

[8] T. C. Killian, S. Kulin, S. D. Bergeson, L. A. Orozco, C. Orzel, and S. L. Rolston. Creation of an ultracold neutral plasma. *Phys. Rev. Lett.*, 83:4776–4779, 1999.

[9] S. Kulin, T. C. Killian, S. D. Bergeson, and S. L. Rolston. Plasma oscillations and expansion of an ultracold neutral plasma. *Phys. Rev. Lett.*, 85:318–321, 2000.

[10] T. C. Killian, M. J. Lim, S. Kulin, R. Dumke, S. D. Bergeson, and S. L. Rolston. Formation of rydberg atoms in an expanding ultracold neutral plasma. *Phys. Rev. Lett.*, 86:3759–3762, 2001.

[11] F. Robicheaux. Proposal for making a beam of antihydrogen by two charge exchange events. *J. Phys. B: At. Mol. Opt. Phys.*, 43:015202, 2010.

[12] A. Reinhard, T. Cubel Liebisch, K. C. Younge, P. R. Berman, and G. Raithel. Rydberg-rydberg collisions: Resonant enhancement of state mixing and penning ionization. *Phys. Rev. Lett.*, 100:123007, 2008.

[13] K. C. Younge, A. Reinhard, T. Pohl, P. R. Berman, and G. Raithel. Mesoscopic rydberg ensembles: Beyond the pairwise-interaction approximation. *Phys. Rev. A*, 79:043420, 2009.

[14] K. C. Younge and G. Raithel. Rotary echo tests of coherence in rydberg-atom excitation. *New J. Phys.*, 11:043006, 2009.

[15] I. Mourachko, Wenhui Li, and T. F. Gallagher. Controlled many-body interactions in a frozen rydberg gas. *Phys. Rev. A*, 70:031401(R), 2004.

[16] Thomas F. Gallagher. *Rydberg Atoms*. Cambridge University Press, 1994.

[17] Michael A. Nielsen and Isaac L. Chuang. *Quantum Computation and Quantum Information*. Press Syndicate of the University of Cambridge, 2000.

[18] Julian Brown. *Minds, Machines, and the Multiverse: The Quest for the Quantum Computer*. Simon and Schuster, 2000.

[19] J. I. Cirac and P. Zoller. Quantum computations with cold trapped ions. *Phys. Rev. Lett.*, 74: 4091, 1995.

[20] I. H. Deutsch, G. K. Brennen, and P. S. Jessen. Quantum computing with neutral atoms in an optical lattice. *Fortschritte der Physik*, 48:925–943, 2000.

[21] Xiaoqin Li, Duncan Steel, Daniel Gammon, and Lu J. Sham. Semiconductor quantum dots. *Optics and Photonics News*, 15:38–43, 2004.

[22] T. Pellizzari, S.A. Gardiner, J.I. Cirac, and P. Zoller. Decoherence, continuous observation, and quantum computing: A cavity qed model. *Phys. Rev. Lett.*, 75:3788–3791, 1995.

[23] R. Laflamme, D.G. Cory, C. Negrevergne, and L.Viola. Nmr quantum information processing and entanglement. *Quantum Information and Computation*, 2:166–176, 2002.

[24] A. Gaetan, Y. Miroshnychenko, T. Wilk, A. Chotia, M. Viteau, D. Comparat, P. Pillet, A. Browaeys, and P. Grangier. Observation of collective excitation of two individual atoms in the rydberg blockade regime. *Nature Physics*, 5:115–118, 2009.

[25] T. Wilk, A. Gaetan, C. Evellin, J. Wolters, Y. Miroshnychenko, P. Grangier, and A. Browaeys. Entanglement of two individual neutral atoms using rydberg blockade. *Phys. Rev. Lett.*, 104: 010502, 2010.

[26] L. Isenhower, E. Urban, X. L. Zhang, A. T. Gill, T. Henage, T. A. Johnson, T. G. Walker, and M. Saffman. Demonstration of a neutral atom controlled-not quantum gate. *Phys. Rev. Lett.*, 104:010503, 2010.

[27] A. Reinhard, T. Cubel Liebisch, B. Knuffman, and G. Raithel. Level shifts of rubidium rydberg states due to binary interactions. *Phys. Rev. A*, 75:032712, 2007.

[28] Thibault Vogt, Matthieu Viteau, Amodsen Chotia, Jianming Zhao, Daniel Comparat, and Pierre Pillet. Electric-field induced dipole blockade with rydberg atoms. *Phys. Rev. Lett.*, 99: 073002, 2007.

[29] Thibault Vogt, Matthieu Viteau, Jianming Zhao, Amodsen Chotia, Daniel Comparat, and Pierre Pillet. Dipole blockade at forster resonances in high resolution laser excitation of rydberg states of cesium atoms. *Phys. Rev. Lett*, 97:083003, 2006.

[30] A. Reinhard, K. C. Younge, T. Cubel Liebisch, B. Knuffman, P. R. Berman, and G. Raithel. Double-resonance spectroscopy of interacting rydberg-atom systems. *Phys. Rev. Lett*, 100: 233201, 2008.

[31] A. Reinhard, K. C. Younge, and G. Raithel. Effect of forster resonances on the excitation statistics of many-body rydberg systems. *Phys. Rev. A*, 78:060702(R), 2008.

[32] Harold J. Metcalf and Peter van der Straten. *Laser Cooling and Trapping*. Springer-Verlag, 1999.

[33] P. Lett, R. Watts, C. Westbrook, W. Phillips, P. Gould, and H. Metcalf. Observation of atoms laser cooled below the doppler limit. *Phys. Rev. Lett.*, 61:169, 1988.

[34] M. Kasevich and S. Chu. Laser cooling below a photon recoil with three-level atoms. *Phys. Rev. Lett.*, 69:1741–1744, 1992.

[35] A. Aspect, E. Arimondo, R. Kaiser, N. Vansteenkiste, and C. Cohen-Tannoudji. Laser cooling below the one-photon recoil energy by velocity-selective coherent population trapping. *Phys. Rev. Lett.*, 61:826–829, 1988.

[36] Naoto Masuhara, John M. Doyle, Jon C. Sandberg, Daniel Kleppner, Thomas J. Greytak, Harald F. Hess, and Greg P. Kochanski. Evaporative cooling of spin-polarized atomic hydrogen. *Phys. Rev. Lett.*, 61:935–938, 1988.

[37] J. V. Hernandez and F. Robicheaux. Simulations using echo sequences to observe coherence in a cold rydberg gas. *J. Phys. B: At. Mol. Opt. Phys*, 41:195301, 2008.

[38] T. A. Johnson, E. Urban, T. Henage, L. Isenhower, D. D. Yavuz, T. G. Walker, and M. Saffman. Rabi oscillations between ground and rydberg states with dipole-dipole atomic interactions. *Phys. Rev. Lett.*, 100:113003, 2008.

[39] Ulrich Raitzsch, Vera Bendkowsky, Rolf Heidemann, Bjrn Butscher, Robert Lw, and Tilman Pfau. Echo experiments in a strongly interacting rydberg gas. *Phys. Rev. Lett.*, 100:013002, 2008.

[40] S. K. Dutta, J. R. Guest, D. Feldbaum, A. Walz-Flannigan, and G. Raithel. Ponderomotive optical lattice for rydberg atoms. *Phys. Rev. Lett.*, 85:5551–5554, 2000.

[41] B. Knuffman and G. Raithel. Multipole transitions of rydberg atoms in modulated ponderomotive potentials. *Phys. Rev. A*, 75:053401, 2007.

[42] M. H. Anderson, J. R. Ensher, M. R. Matthews, C. E Wieman, and E. A. Cornell. Observation of bose-einstein condensation in a dilute atomic vapor below 200 nanokelvin. *Science*, 269:198, 1995.

[43] C. Monroe, D. M. Meedkhof, B. E. King, W. M. Itano, and D. J. Wineland. Demonstartion of a fundamental quantum logic gate. *Phys. Rev. Lett.*, 75:4714, 1995.

[44] Z. T. Lu, K. L. Corwin, M. J. Renn, M. H. Anderson, E. A. Cornell, and C. E. Wieman. Low-velocity intense source of atoms from a magneto-optical trap. *Phys. Rev. Lett.*, 77:3331–3334, 1996.

[45] D. Tong, S. M. Farooqi, J. Stanojevic, S. Krishnan, Y. P. Zhang, R. Ct, E. E. Eyler, and P. L. Gould. Local blockade of rydberg excitation in an ultracold gas. *Phys. Rev. Lett.*, 93:063001, 2004.

[46] Amnon Yariv and Pochi Yeh. *Optical Waves in Crystals: Propagation and Control of Laser Radiation*. John Wiley and Sons, Inc., 2003.

[47] E. Hansis, T. Cubel, J.-H. Choi, J. R. Guest, and G. Raithel. Simple pressure-tuned fabryperot interferometer. *Review of Scientific Instruments*, 76:033105, 2005.

[48] Erik D. Black. An introduction to pounddreverhall laser frequency stabilization. *Am. J. Phys.*, 69:79–87, 2001.

[49] J.J. Arlt, O. Marago, S. Webster, S. Hopkins, and C.J. Foot. A pyramidal magneto-optical trap as a source of slow atoms. *Optics Communications*, 157:303–309, 1998.

[50] R. C*hatrmotacuterme*. From classical mobility to hopping conductivity: Charge hopping in an ultracold gas. *PRL*, 85:5316, 2000.

[51] Marcel Mudrich, Nassim Zahzam, Thibault Vogt, Daniel Comparat, and Pierre Pillet. Back and forth transfer and coherent coupling in a cold rydberg dipole gas. *Phys. Rev. Lett.*, 95: 233002, 2005.

[52] T. Cubel, B. K. Teo, V. S. Malinovsky, J. R. Guest, A. Reinhard, B. Knuffman, P. R. Berman, and G. Raithel. Coherent population transfer of ground-state atoms into rydberg states. *Phys. Rev. A*, 72:023405, 2005.

[53] C. S. E. van Ditzhuijzen, A. F. Koenderink, J. V. Hernndez, F. Robicheaux, L. D. Noordam, and H. B. van Linden van den Heuvell. Spatially resolved observation of dipole-dipole interaction between rydberg atoms. *Phys. Rev. Lett.*, 100:243201, 2008.

[54] Rolf Heidemann, Ulrich Raitzsch, Vera Bendkowsky, Bjrn Butscher, Robert Low, Luis Santos, and Tilman Pfau. Evidence for coherent collective rydberg excitation in the strong blockade regime. *Phys. Rev. Lett.*, 99:163601, 2007.

[55] J. V. Hernndez and F. Robicheaux. Simulation of a strong van der waals blockade in a dense ultracold gas. *J. Phys. B: At. Mol. Opt. Phys.*, 41:045301, 2008.

[56] M. Reetz-Lamour, T. Amthor, J. Deiglmayr, and M. Weidemuller. Rabi oscillations and excitation trapping in the coherent excitation of a mesoscopic frozen rydberg gas. *Phys. Rev. Lett.*, 100:253001, 2008.

[57] E. L. Hahn. Spin echoes. *Phys. Rev.*, 80:580, 1950.

[58] I. Solomon. Rotary spin echoes. *Phys. Rev. L*, 2:301, 1959.

[59] F. Robicheaux. Ionization due to the interaction between two rydberg atoms. *J. Phys. B: At. Mol. Opt. Phys.*, 38:S333–S342, 2005.

[60] Norman F. Ramsey. A molecular beam resonance method with separated oscillating fields. *Phys. Rev.*, 78:695–699, 1950.

[61] F. Robicheaux and J. V. Hernndez. Many-body wave function in a dipole blockade configuration. *Phys. Rev. A*, 72:063403, 2005.

[62] Thad G Walker and Mark Saffman. Zeros of rydbergrydberg forster interactions. *J. Phys. B: At. Mol. Opt. Phys.*, 38:S309, 2005.

[63] P. S. Jessen and I. H. Deutsch. Optical lattices. *Adv. At. Mol. Opt. Phys.*, 37:95–136, 1996.

[64] U. Schneider, L. Hackerm"uller, S. Will, Th. Best, I. Bloch, T. A. Costi, R. W. Helmes, D. Rasch, and A. Rosch. Metallic and insulating phases of repulsively interacting fermions in a 3d optical lattice. *Science*, 322:1520–1525, 2008.

[65] C. M. Chandrashekar and Raymond Laflamme. Quantum phase transition using quantum walks in an optical lattice. *Phys. Rev. A*, 78:022314, 2008.

[66] Andrew J. Ferris, Murray K. Olsen, and Matthew J. Davis. Atomic entanglement generation and detection via degenerate four-wave mixing of a bose-einstein condensate in an optical lattice. *Phys. Rev. A*, 79:043634, 2009.

[67] J.-H. Choi, J. R. Guest, A. P. Povilus, E. Hansis, and G. Raithel. Magnetic trapping of long-lived cold rydberg atoms. *Phys. Rev. Lett.*, 95:243001, 2005.

[68] P. H. Bucksbaum, D. W. Schumacher, and M. Bashkansky. High-intensity kapitza-dirac effect. *Phys. Rev. Lett.*, 61:1182, 1988.

[69] D. Normand, L.-A. Lompr*acuterme*, A. L'Huillier, J. Morellec, M. Ferray, J. Lavancier, G. Mainfray, and C. Manus. Ac stark shifts induced by a yag lser in the np and nf rydberg series in xenon. *J. Opt. Soc. Am. B*, 6:1513, 1989.

[70] T. R. OBrian, J.-B. Kim, G. Lan, T. J. McIlrath, and T. B. Lucatorto. Verification of the ponderomotive approximation for the ac stark shift in xe rydberg levels. *Phys. Rev. A*, 49: R649, 1994.

[71] Marcus P. Hertlein, Philip H. Bucksbaum, and H. G. Mullerz. Evidence for resonant effects in high-order ati spectra. *J. Phys. B: At. Mol. Opt. Phys.*, 30:L197–L205, 1997.

[72] G. G. Paulus, F. Grasbon, H. Walther, R. Kopold, and W. Becker. Channel-closing-induced resonances in the above-threshold ionization plateau. *Phys. Rev. A*, 64:021401, 2001.

[73] Dieter Meschede and Arno Raschenbeutel. Manipulating single atoms. *Adv. At. Mol. Phys.*, 53:76–102, 2006.

[74] K. C. Younge, B. Knuffman, S. E. Anderson, and G. Raithel. State-dependent energy shifts of rydberg atoms in a ponderomotive optical lattice. *Phys. Rev. Lett.*, 104:173001, 2010.

[75] K. C. Younge, S. E. Anderson, and G. Raithel. Adiabatic potentials for rydberg atoms in a ponderomotive optical lattice. *New. J. Phys.*, 12:023031, 2010.

[76] Harald Siegfried Friedrich. *Theoretical Atomic Physics*. Springer, 2004.

[77] K. Afrousheh, P. Bohlouli-Zanjani, J. D. Carter, A. Mugford, and J. D. D. Martin. Resonant electric dipole-dipole interactions between cold rydberg atoms in a magnetic field. *Phys. Rev. A*, 73:063403, 2006.

[78] Myron L. Zimmerman, Jarbas C. Castro, and Daniel Kleppner. Diamagnetic structure of na rydberg states. *Phys. Rev. Lett.*, 40:10831086, 1978.

[79] J. C. Gay and D. Delande. The hydrogen atom in a magnetic field. symmetries in the low field diamagnetic limit. *Comments At. Mol. Phys*, 13:275, 1983.

[80] P. Cacciani, E. Luc-Koenig, J. Pinard, C. Thomas, and S. Liberman. Experimental studies of a diamagnetic multiplet in odd rydberg states of lithium. *Phys. Rev. Lett.*, 56:1124–1127, 1986.

[81] T. van der Veldt, W. Vassen, and W. Hogervorst. Helium rydberg states in parallel electric and magnetic fields. *J. Phys. B: At. Mol. Opt. Phys.*, 26:1945–1955, 1993.

[82] P. Cacciani, S. Liberman, E. Luc-Koenig, J. Pinard, and C. Thomas. Rydberg atoms in parallel magnetic and electric fields. *J. Phys. B: At. Mol. Opt. Phys.*, 21:3473–3498, 1988.

[83] Abbas Khadjavi and Allen Lurio. Stark effect in the excited states of rb, cs, cd, and hg. *Phys. Rev.*, 167:128–135, 1968.

[84] W. A. Van Wijngaarden. Scalar and tensor polarizabilities of low lying s, p, d, f, and g states in rubidium. *J. Quant. Spectrosc. Radiat. Transfer*, 2:275–279, 1997.

[85] Keith D. Bonin and Vitaly V. Kresin. *Electric-dipole polarizabilities of atoms, molecules, and clusters*. World Scientific Publishing Company, 1997.

[86] M. Marinescu, H. R. Sadeghpour, and A. Dalgarno. Dynamic dipole polarizabilities of rubidium. *Phys. Rev. A*, 49:5103–5104, 1994.